CARBONYLATION OF CYCLOHEXENE WITH CARBON DIOXIDE (CO_2) USING TRANSITION METALS AS HETEROGENEOUS AND HOMOGENEOUS CATALYSTS

A thesis submitted in fulfilment of the requirements for the degree of Master of Science in chemistry at the

Department of Chemistry

Rhodes University

Makhanda 6140

South Africa

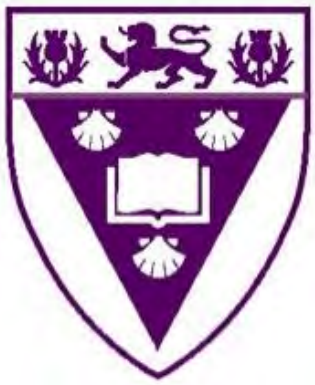

By

Bafokeng Thabelo Sekaleli

December 2023

Supervised by

Professor Rui Krause, Doctor Vincent Smith and Doctor Theodor Geswindt

Acknowledgements

First and foremost, I would like to thank the high-power for granting me courage, diligence and most importantly the resilience which helped me throughout my whole academic journey.

Many thanks to my supervisors Professor Rui Krause, Doctors Vincent Smith and Theodor Geswindt who gave me a great opportunity to further my studies. Thank you for your guidance that helped me grow and develop my skills in research. Most importantly, thank you for the moola! Lastly, to my distant supervisor Doctor Samuel Jali, thank you for your advice and guidance.

Thank you to Rhodes University and Doctor Vincent Smith for the financial support through the Sandisa Imbewu Fund.

A big thank you to the Chemistry department, the support staff and all my research teammates (Lab F22 & F2). I am filled with so much gratitude for the support and advice that I have received from Professor Rosa Klein, Mrs Benita Tarr and Mrs Bukiwe Magopeni, thank you!

I would like to thank; Professor Roderick Walker for training on and using his DSC, Professor Tebello Nyokong for training on and using her solid-state UV-Vis spectrophotometer, the Electron Microscope Unit and Mr Marvin Randall for training on and using TEM and EDX analysis.

Most importantly a huge thank you to my beloved friends and colleagues, Lebo Ramohapi, Nthabeleng Molupe, Ntseka Masoabi, Tsebang Matlapeng, Mofeli Leoma, Yamkela Siko, Urbain Ndagano, Justin Safari, Sodeeq Aderotimi, Thierry Lwanzo, Yolande Openda, Andile Zitha, Alain Bapolisi, Baa Ebenezer, Preven Chetty, William Maletje, Reuben Thufhulufhelwi, Tsotelo Mapetla, Bokang Mosiuoa and Liteboho Pii.

Above all; my family! My mother Mrs ‘Mabafokeng Sekaleli, my sister Lineo Sekaleli, my grandmother Mrs ‘Manthakoana Moleko, my aunts Ms Sebolelo Moleko, Ms Mookho Moleko, Mrs Mpasi Mokoka and the rest of the family. Thank you a million times for your utmost support and prayers, this wouldn’t have been possible without you. *Kea leboha Bafokeng!*

Abstract

From a green chemistry perspective, carbon dioxide (CO_2) emerges as an appealing C1 synthon, given its abundance in the atmosphere and cost-effectiveness. Many essential chemicals for daily life are derived from fossilized carbon sources like coal, petroleum, and natural gas. However, the by-product of these processes, CO_2, poses environmental risks when excessively emitted as a greenhouse gas. Achieving a balance between carbon emissions and removal is crucial to address environmental concerns surrounding CO_2.

Utilizing CO_2 as a C1 source in organic synthesis holds promise for mitigating this balance in the long term. Combining CO_2 with other underutilized fine chemicals, such as alkanes, alkenes, and alkynes, to produce more valuable platform chemicals presents an economically viable strategy due to carbon dioxide's abundance, low cost, and recyclability. Despite its simplicity, CO_2's high thermodynamic stability and low kinetic reactivity, owing to its highly oxidized state, pose challenges to its use as a feedstock.

Overcoming these hurdles requires catalysts to enhance CO_2 reactivity. Our work focuses on developing and employing catalytic systems capable of activating CO_2 as a C1 synthon in reactions with cyclohexene and a reducing agent to yield carboxylic acids or esters. In one approach, we have developed heterogeneous catalyst systems comprising transition metals (Au, Fe, Ni, Ru) supported on metal oxide (TiO_2). Characterization techniques such as TEM, EDX, UV-Vis, BET, and XRD were used to study the properties of these materials. The catalysts were evaluated in a reaction involving cyclohexene, CO_2, and H_2O.

In another approach, we explored the use of cyclo-tris(tetracarbonylruthenium) [$Ru_3(CO)_{12}$] as a homogeneous catalyst in a reaction involving cyclohexene, methanol, and CO_2 in the presence of an ionic liquid, 1-Butyl-3-methylimidazolium chloride ($[BMIM]^+Cl^-$). ^1H NMR and ATR-FT-IR were utilized to characterize $[BMIM]^+Cl^-$. The reaction product was characterised utilizing GC-MS.

Upon seeing that $Ru_3(CO)_{12}$ changes color from orange to black when exposed to heat, an investigation was undertaken on the kind of transformations that the catalyst undergoes. This investigation was carried out with the hopes of finding the structures that could be resulting from $Ru_3(CO)_{12}$ during the reaction and their significance to it. The orange and black Ru complexes were characterized utilizing DSC, TGA, ATR-FT-IR and PXRD.

Table of Contents

1. INTRODUCTION

1.1 Carbon Dioxide – a Brief Overview

Carbon dioxide (CO_2) is a naturally occurring, colourless and odourless atmospheric gas, ranking fourth in abundance in the atmosphere. CO_2 is generated through respiration, during which organisms metabolize food for energy. This serves as a substrate for photosynthesis, where plants and select microbes convert it and water into organic compounds in the presence of sunlight, releasing oxygen in the process.[1,2] The primary ecological importance of CO_2 lies in its ability to regulate the Earth's temperature.

As a greenhouse gas, CO_2 allows short-wavelength solar radiation to penetrate the Earth's atmosphere and captures the long-wavelength radiation reflected from the Earth's surface. The captured energy is subsequently re-emitted towards the Earth, creating a warming effect.[3] In the absence of this mechanism, Earth's average temperature would be an inhospitable -19℃, instead of the current average of 14℃. [3 4]

Natural sources of atmospheric CO_2 include biomass decomposition, biological respiration, volcanic emissions, and wildfires.[1,2] However, anthropogenic activities, primarily through the combustion of fossil fuels and deforestation, have significantly augmented atmospheric CO_2 concentrations. Since the advent of industrialization, atmospheric CO_2 levels have surged from 280 ppm to approximately 400 ppm, contributing to a temperature increase from 0.4℃ in 1850 to 0.7℃ in 2019. [4 5] According to the Intergovernmental Panel on Climate Change (IPCC), the majority of recent global warming could be attributed to human-derived activities.[6]

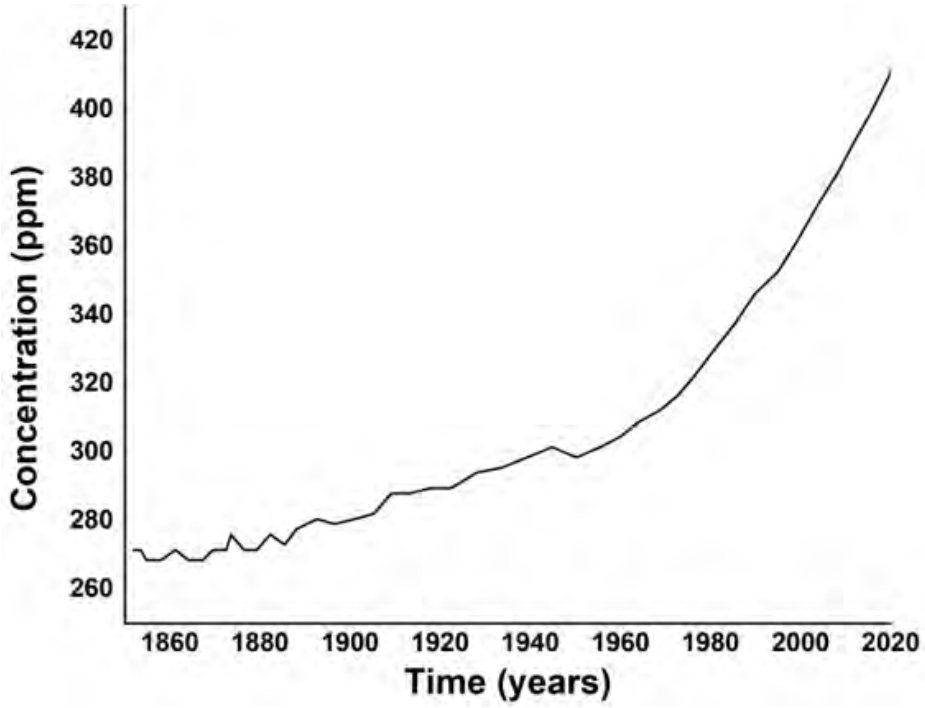

Figure 1.1 *Global average long-term atmospheric concentration of CO_2 in ppm from 1146 to 2018 measured from EPICA Dome C & NOAA* [6]

Additionally, elevated CO_2 levels contribute to ocean acidification[7]; which is a consequence of silicates and carbonate rock weathering by acid rain (upon interaction of CO_2 with rainwater). The resultant alkaline ions change the ocean's CO_2 absorption capacity, further acidifying marine environments.[4] Furthermore, CO_2-induced climate change leads to physical, health, and ecological challenges which intensified by anomalous weather occurrences. These disruptions can impair agricultural output, further impacting socio-economic stability.[6]

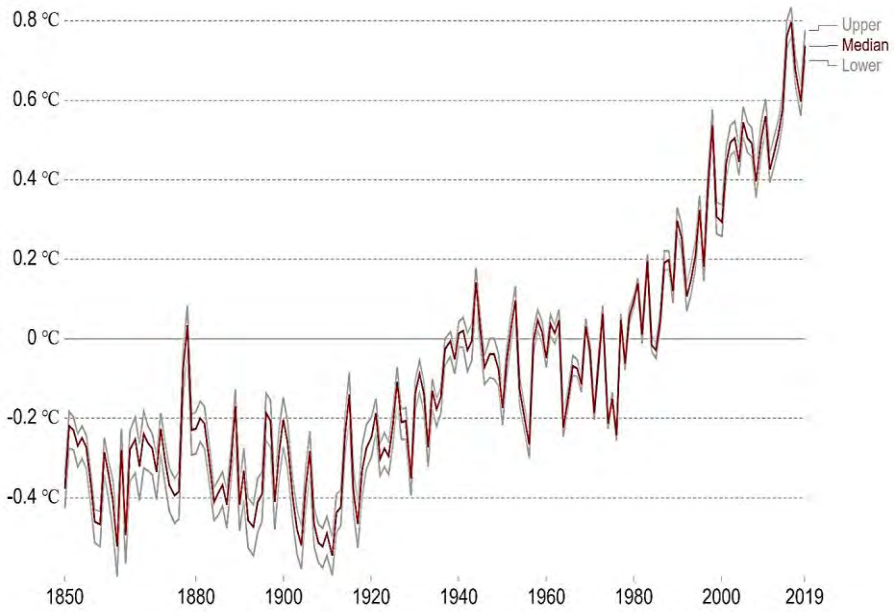

***Figure 1.2**. Global average land-sea temperature anomaly relative to the 1961-1990 average temperature sourced from Met Office Hadley Centre*[6]

While CO_2, regarded as an industrial by-product, can be repurposed as a feedstock in chemical sectors and academic endeavours[8] [9] [10], this research is driven by the prospect of employing CO_2 as a C1 reagent, in conjunction with olefins, for the production of high-value chemicals. However, it's essential to recognize that solely using CO_2 in synthesis doesn't mitigate its atmospheric abundance.[11]

1.2 Uses of CO_2 as a C1 feedstock

Due to its abundance, low cost and recyclability[9] [12] CO_2 is highly desirable in the chemical synthesis of various commodities – with the annual global consumption roughly being 110 *M*t. The primary industrial consumer of CO_2 is in the production of urea which is used for the manufacturing of nitrogenous fertilizers.[13] [14] Traditionally, CO_2 is used in the production of carboxylic acids, carbonates, esters, *etc*. **(Scheme 1.1)**; however, a comprehensive literature survey reveals relatively few reports on the use of CO_2 as a C1 synthon in combination with olefins during the production of carboxylic acids and esters.

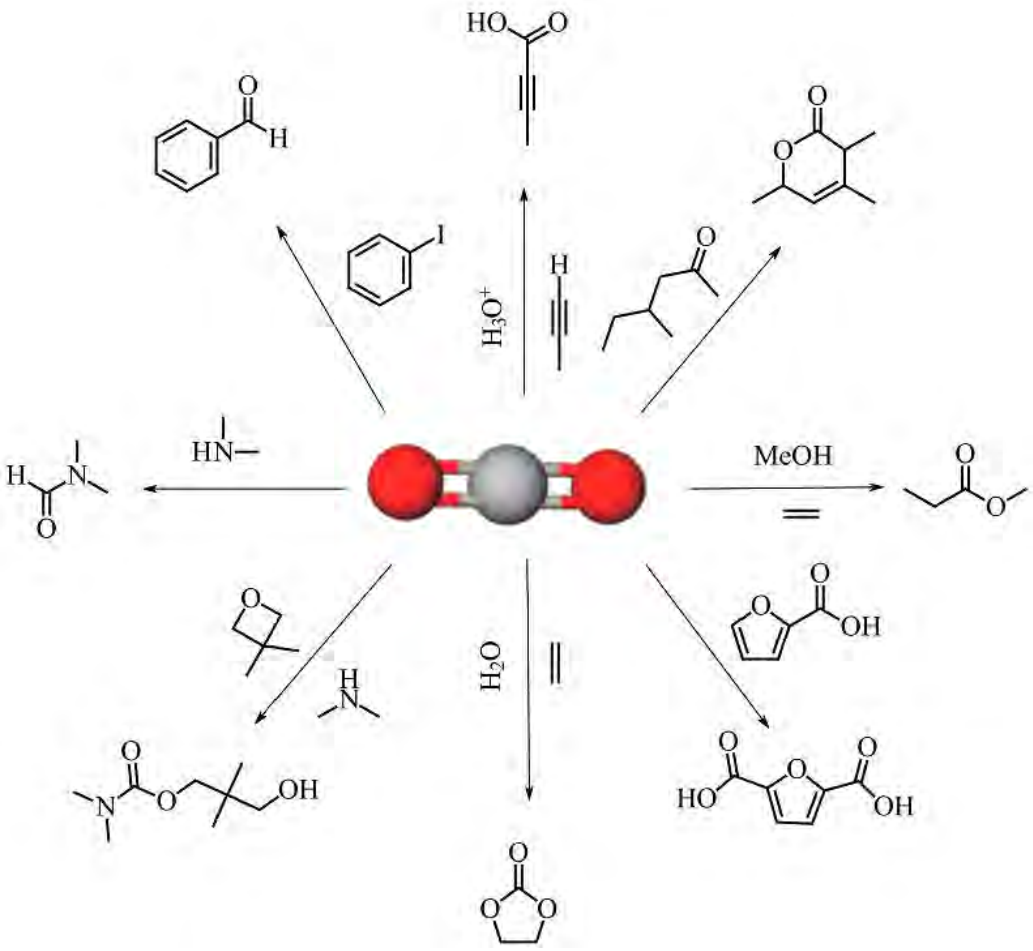

Scheme 1.1 *A summary of different reactions that involve the use of CO_2 as a C1 synthon with a variety of starting materials in organic synthesis*

(*i*) For production of carboxylic acids

Carboxylic acids (R-COOH) are a group of compounds with good chemical and physical properties resulting from their hydroxyl (-OH) and carbonyl (-C=O) function in their molecular structure. These properties present a great opportunity for their application in chemical synthesis for making a range of products useful in areas such as medicine, pharmaceuticals, polymer sciences and many more.[15 16] These class of compounds are usually produced through the oxidation of aldehydes, primary alcohols, oxidative cleavage of olefins, dehydrogenation of alcohols etc.[16 17] Though these conventional approaches efficiently produce carboxylic acids, using CO_2 as a simplest alternative C_1 feedstock to nucleophiles such as olefins to obtain carboxylic acids is an interesting and important approach because CO_2 is abundant and relatively cheap. In addition, the olefins are produced in large amounts in petrochemical industry through cracking process and as side products in pyrolysis of plastic.[18 19]

This method of producing carboxylic acids can happen in two ways. Firstly, through carboxylation whereby the CO_2 molecule is fully incorporated into the olefin without being reduced.[20] [21] The production of propionic acid via carboxylation of ethene with CO_2 **(Scheme 1.2)** is amongst the earliest reactions of this kind which was influenced by the discovery of the reaction of metal complexes with CO_2 and olefins through their insertion into the metal-carbon bond of a Ni complex, bis(cyclooctadiene)nickel(0), in the presence of 1,8-diazabicyclo[5.4.0]undec-7-ene (DBU) resulting in a metalalactone which upon hydrolysis gives off the corresponding acid.[20] [22]

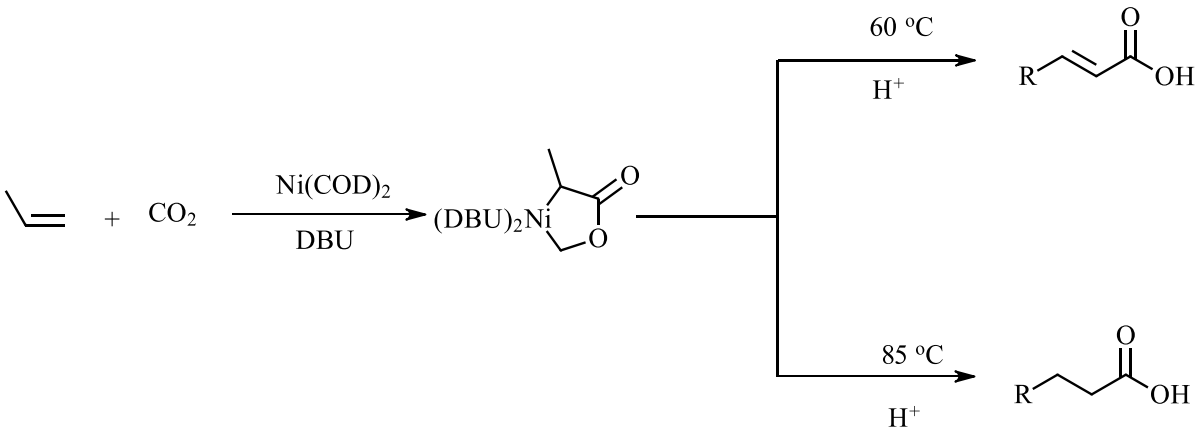

Scheme 1.2 *Production of propionic acid using propene and CO_2 facilitated by bis(cyclooctadiene)nickel(0) and 1,8-diazabicyclo[5.4.0]undec-7-ene at 85 °C under acidic conditions*

Furthermore, literature has also reported the carboxylation of alkenes with CO_2 via C-H bond activation.[23] In this approach α,β-unsaturated carboxylic acids are synthesized from α-arylalkenes and CO_2 in a reaction facilitated by a Lewis acid and a base as a catalyst. For this reaction, 2,6-cardisubstituted pyridine and diethylaluminium chloride ($EtAlCl_2$) were used as base and Lewis acid respectively in the presence of CO_2 and an olefin **(Scheme 1. 3)**.[23]

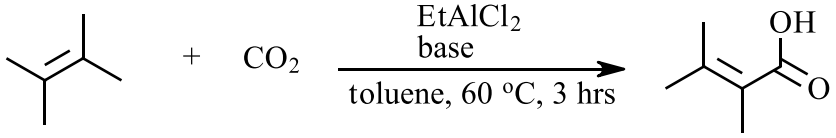

Scheme 1. 3 *Synthesis of α,β-unsaturated carboxylic acids from 2,3-dimethylbut-2-ene and CO_2 in the presence of diethylaluminium chloride as a catalyst, 2,6-cardisubstituted pyridine as a base and toluene as a solvent at 60 °C for 3 hours*

The second route reported for production of carboxylic acids is via carbonylation in which the CO_2 is in-situ reduced to a more reactive CO which subsequently reacts with the olefin. An example of this reaction is that between but-2-ene, hydrogen, and CO_2 **(Scheme 1.4)** catalyzed by di-μ-chloro-tetracarbonyldirhodium(I) , as a reverse water-gas shift reaction through the

reduction of CO_2 by hydrogen, in the presence of triphenyl phosphine (PPh_3), methyl iodide (CH_3I) as a promoter and p-Toluenesulfonic acid (p-TsOH.H_2O) as an acid additive.

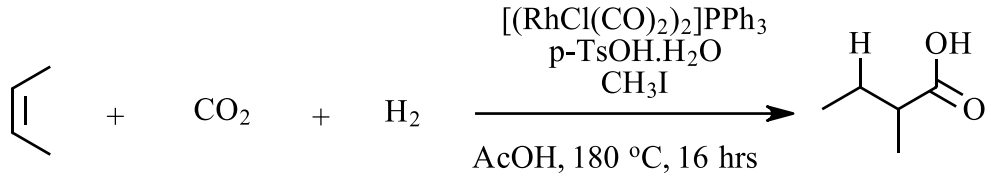

Scheme 1.4 *Carbonylation of but-2-ene with CO_2 in the presence of hydrogen as a, di-μ-chloro-tetracarbonyldirhodium(I), p-Toluenesulfonic acid, methyl iodide and acetic acid at 180 ^{O}C for 16 hours*

(*ii*) For production of esters

Generally, esters are derivatives of carboxylic acids obtained through a reaction between an acid and alcohol.[23] To access more esters through this well-established multi-step processes requires the use of corrosive acids and besides that, high quantity of undesired by-products are generated in the process.[25] Therefore the use of CO_2 and olefins to access esters is a more desirable alternative as it is a greener and economical approach. A few novel methodologies for the synthesis of esters via the incorporation of CO_2 into olefins have been developed. Amongst these is the synthesis of *α,β*-unsaturated ester **(Scheme 1.5)** facilitated by a transition metal complex. A Pd or Ni complex is used in this reaction to react with CO_2 and ethene to form a nickelalactone, followed by methylation of the metallacycle with CH_3I producing methyl acrylate.[20]

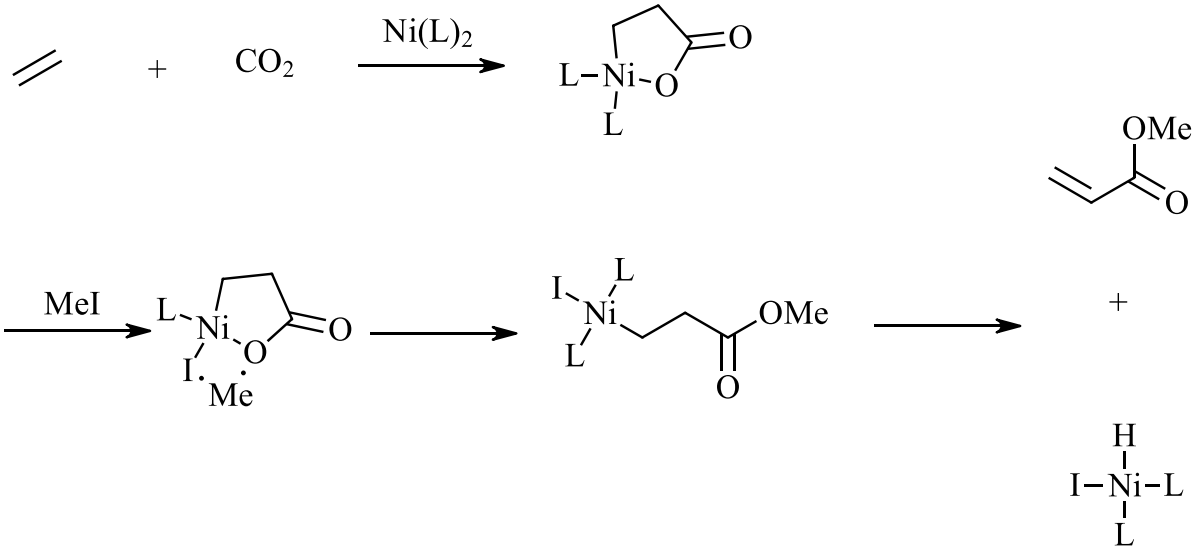

Scheme 1.5 *A general synthesis route of making esters from an olefin and CO_2 in the presence of a $Ni(L)_2$ complex leading to a formation of a nickelalactone which through methylation with methyl iodide gives of a methyl acrylate.*

Recently, literature has reported the synthesis of esters through the alkoxycarbonylation of olefins with CO_2. [25,26] This approach **(Scheme 1.6)** involves the use of cyclo-tris(tetracarbonylruthenium)(3 Ru—Ru), $Ru_3(CO)_{12}$, as a catalyst, an ionic liquid, 1-butyl-3-methylimidazolium chloride ([BMIM]Cl) as a CO_2 absorbent and an additive that suppresses hydrogenation of the olefin, methanol as a reducing agent to facilitate an in-situ reduction of CO_2 to CO which in turn reacts with the olefin and the alcohol to form an ester.[25 26]

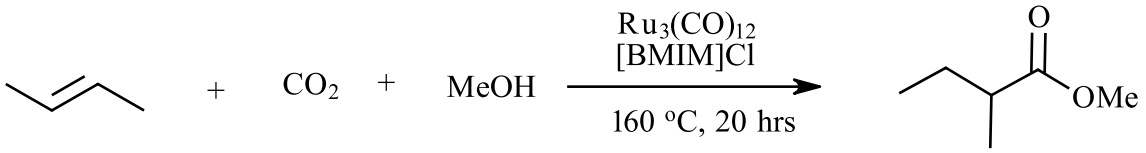

Scheme 1.6 *Alkoxycarbonylation of but-2-ene with CO_2 and methanol in the presence of cyclo-tris(tetracarbonylruthenium)(3 Ru—Ru) as a possible catalyst, 1-butyl-3-methylimidazolium chloride as an additive at 160 ^{O}C for 20 hours*[25 26]

Although the utilization of CO_2 for chemical synthesis presents an attractive prospect, a significant challenge arises due to the thermodynamic stability of this highly oxidized molecule, making it difficult to react with other molecules.[11 27] These characteristics of CO_2 can be understood through its chemical properties.

1.3 Chemical properties of CO_2

Carbon dioxide is a linear molecule in its ground state, with 16 valence electrons and belongs to the D ∞ h symmetry group. The CO_2 molecule is nonpolar with two polar carbon – oxygen (C=O) bonds, with an extremely high dissociation energy of about 750 $kJmol^{-1}$, that are of equal bond lengths with two orthogonal π-orbitals.[28 29] The highest occupied molecular orbitals (HOMO) of the two oxygen atoms make them weak Lewis bases and therefore are nucleophilic centers. On the other hand, the lowest unoccupied molecular orbitals (LUMO) of the carbon atom give it a Lewis acid character and are electrophilic centres.[11 28 30]

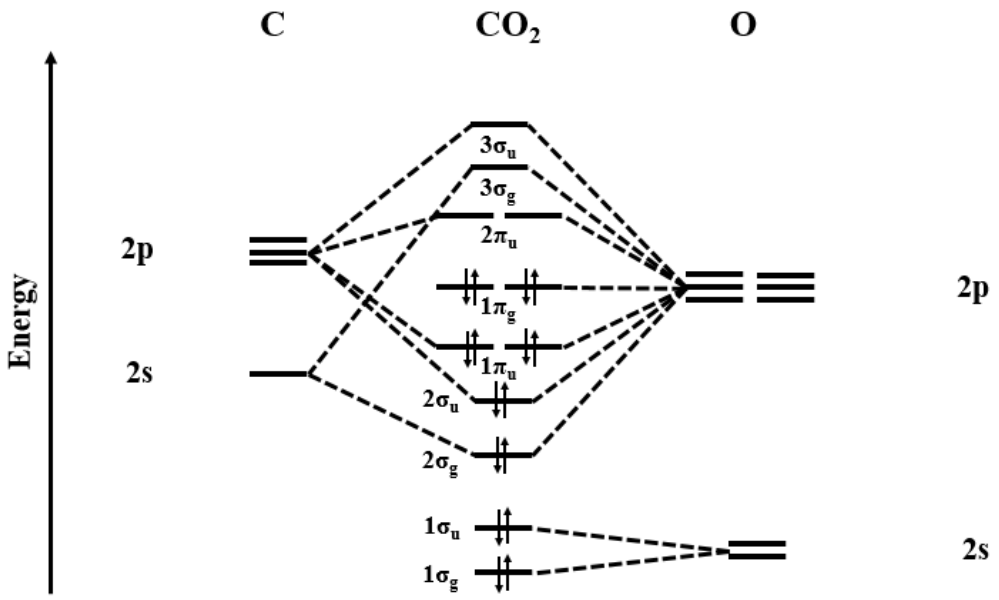

Figure 1.3 *Molecular orbital diagram of CO_2 showing the electron distribution within the different energy levels of the molecules to highlight it's reactivity*[31]

The molecule of CO_2 is in its highly oxidated state therefore has a high thermodynamic stability and a low kinetic reactivity.[32] [33] [34] The high stability and low reactivity of CO_2 can be understood from its molecular orbitals. The orbitals of significant importance in the reactivity of CO_2 are the 2s and 2p orbitals of the carbon and oxygen atoms, the 1s orbitals on the other hand don't play a role in reactivity and therefore stay unchanged.[31] [35]

The 2s orbitals of the two oxygens are too low in energy and therefore do not interact with any of the carbon orbitals. Interaction between 2s and $2p_x$ orbitals of carbon with $2p_x$ orbital of oxygen give rise to $2\sigma_u$, $2\sigma_g$ bonding molecular orbitals and $3\sigma_g$ anti-bonding molecular orbital while the interaction between $2p_y$ and $2p_z$ orbitals give rise to three doubly degenerate molecular orbitals which are $1\pi_u$ bonding orbital, $1\pi_g$ non-bonding orbital and $2\pi_u$ anti-bonding orbital. The 16 valence electrons are distributed among four σ-orbitals and two doubly degenerate π-orbitals.[35] The $1\pi_g$ non-bonding orbital localized at the oxygen atoms and $2\pi_u$ anti-bonding orbital localized at the carbon atom have the highest significance in reactivity as HOMO and LUMO respectively. As a result, the carbon dioxide molecule can be regarded as amphoteric due to the Lewis basic character of the oxygen atoms and the Lewis acid character of the carbon atom.[31]

Indicated in the molecular orbital structure of CO_2 above, it is expected to be energetically favorable for the reactivity of CO_2 to happen through the $2\pi_u$ anti-bonding orbital because of two reasons; firstly, the doubly degenerate $2\pi_u$ is empty therefore making it prone to lateral

distortion which destroys the degeneracy resulting in two orbitals, $2b_1$ and $6a_1$ while $1\pi_g$ non-bonding orbital stays intact because it has a maximum pairing of electrons.[35]

The resulting $2b_1$ orbital after distortion has a similar energy as before distortion while $6a_1$ orbital after distortion has its energy lowered significantly to almost the same energy as $1\pi_g$ non-bonding orbital making it energetically easier for electrons to occupy it in a reaction. Secondly, the electrons of the doubly degenerate $1\pi_g$ non-bonding orbital localized towards the highly electronegative oxygen are very low in energy making it energetically costly for them to take part in a reaction.[35] Therefore, CO_2 is an electron acceptor with its reactivity regulated by the electrophilic characteristics of the carbon atoms.[31]

Regardless of this reactivity of CO_2, the energy requirement for nucleophilic attack is still high therefore highly energetic nucleophilic molecules have been used in the past to form new C-C and C-H bonds. Examples of such nucleophiles are aziridines, epoxides, organometallic and Grignard reagents. The issue with using this chemicals is that they are toxic, their production is expensive and energy intensive therefore efficient and benign transformations under mild conditions need to be established.[11] This can be achieved by the application of transition metal catalysis to activate the CO_2 through its coordination with the metal center.

1.4 Interaction of CO_2 with transition metals

The first step in activating CO_2 for further reactions is by coordinating it to a transition metal centre. This coordination leads to changes in electronic structure and molecular geometry, thereby enhancing its reactivity.[36] Transition metals can activate CO_2 through interaction with their surfaces *via* the carbon or oxygen centres, either singly or in combination, at single or multiple coordination sites.[35] Due to the amphoteric nature of the CO_2 molecule, it can interact with metal centers by either accepting electrons through its carbon atom or by donating electrons from its oxygen atoms to the metal center. This depends on the oxidation states of the metal centers; for nucleophilic low oxidation state metal centers, the interaction will happen through the carbon atom. While on the other hand the electrophilic high oxidation state metal centers will interact with the oxygen centers.

This interaction can occur through different modes of coordination as illustrated in **Figure 1.4**. In mode **I** (η^1c) there is an electron transfer from the d_z^2 orbital of the transition metal to the $2\pi_u$ anti-bonding orbital of the carbon atom. Mode **II** (η^1o) shows an end-on coordination between one oxygen atom (through its lone pair of electrons) and an electron deficient metal centre with CO_2 molecule retaining its linear structure. In mode **III** (η^2o,o), there is an

interaction between the two oxygen atoms of CO_2 and one electron deficient metal center forming a metal-carboxylate system. Mode **IV** (η^2c,o), illustrates a σ-bond between the π-orbital of one of the oxygen atoms and an empty d_z^2 metal orbital, together with π-back bonding from the d_{xy} metal orbital to the $2\pi_u$ anti-bonding orbital of the carbon atom.[28]

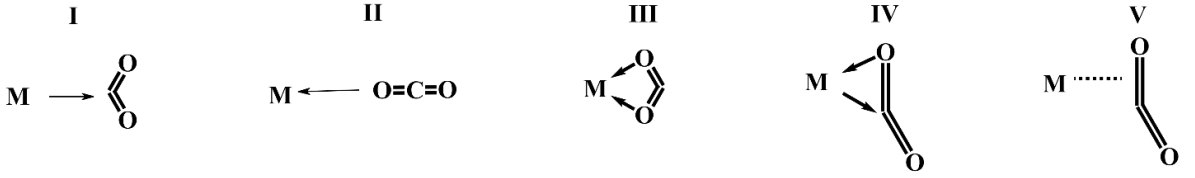

Figure 1.4 *Coordination mode of CO_2 with transition metals, I) electron transfer from electron rich metal to carbon atom, II) interaction of lone pair on oxygen with metal center, III) electron transfer from two oxygen atoms to an electron deficient metal centre, IV) this mode is a combination of I, II and III. V) side-on-bonding π-complex*[11]

Common coordination such as (η^2c,o) and (η^1c) have been extensively reported in literature. Though both of these are common but (η^2c,o) is the most popular because direct carbon metal interaction in (η^1c) is not energetically favorable due to the repulsive interaction between the metal and carbon center. Therefore, activation through interaction of metal with one oxygen and a carbon atom in (η^2c,o) is expected to be energetically favorable.

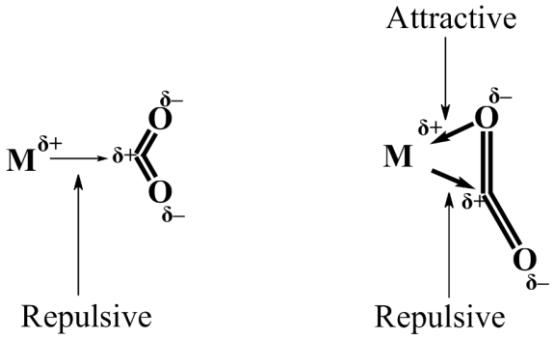

Figure 1.5. *Illustration of the different electrostatic interactions that can occur between the CO_2 and a metal centre*[35]

In the (η^2c,o) coordination mode, the C=O bonds are inequivalently elongated and the molecule also loses its linearity to become a bent molecule with O-C-O bond angles between 130˚ and 136˚ depending on the complex. Some of these complexes reported in literature are; $(PCy_3)_2Ni(CO_2)$, $Nb(\eta\text{-}C_5H_4Me)_2(CH_2SiMe_3)(\eta^2\text{-}CO_2)$, $Pd(PMePh_2)_2(CO_2)$, $Mo(CO_2)_2(PMe_3)_4$ etc.[37] [38] [39] Similarly, in the (η^1c) mode, the C=O bond lengths are asymmetrically elongated and the linearity changes leaving the molecule with a bent geometry with a O-C-O angle of 126˚. This coordination type can be found in complexes such as $Rh(diars)_2Cl(CO_2)$, $Ir(CO_2)(Cl)(dmpe)_2$, $(PMe_3)_4Fe(CO_2)$.[40]

As for the (η^1o) end on coordination mode, the only complex that has been isolated so far is the Uranium complex, (^{Ad}ArO)$_3$tacnU(η^1-OCO) in which the linearity of the CO_2 molecule is slightly changed to 178˚ O-C-O bond. Generally, interactions of a metal center with oxygen atoms in (η^1o) and (η^2o,o) with reference to the molecular orbital projections, are highly unfavorable due to the low energy of the oxygen electrons in the HOMO.[35] Nonetheless, interaction between a metal center and an oxygen atom can be highly favored if there is an oxygen defect, a vacancy, in the lattice of the reducible transition metal oxide surface. The role of the oxygen atom in the CO_2 molecule would be to replenish the surface oxygen of the reducible metal oxide, when it adsorbs on the surface, thus reducing the CO_2 molecule to CO.[41]

Coordinated CO_2 can further react due to changes in geometry and properties, which increase its reactivity. It can react in three different ways; firstly through its reaction with electrophiles, secondly through reaction with nucleophiles and lastly via oxygen transfer and C=O bond cleavage producing a more reactive CO that can further react with something else.[40]

1.5 Aims and objectives of study

Based on the background information on CO_2, a partial aim of this study was geared toward the use of CO_2 as a C_1 synthon to a cyclohexene (considered a less-valuable feedstock) for synthesizing platform chemicals applicable in various chemical processes. To achieve this, the study pursued the following objectives:

a. The incorporation of the CO_2 molecule into the cyclohexene double bond in the presence of a source of hydrogen with the expectation of obtaining the corresponding carboxylic acid through heterogeneous catalysis and an ester through homogeneous catalysis.

b. The utilization of homo- and heterogeneous transition metal-based catalysts to enhance the reactivity of CO_2.

2. HETEROGENOUS CATALYSIS

2.1. Introduction

At the heart of industrial activity lies mainly heterogeneous catalysis which contributes about 90 % to all chemical processes in petrochemical, pharmaceutical, food and other chemical industries.[42] This catalytic process utilizes a chemical substance in a separate phase from the reactants, enhancing the reaction rate without being consumed in the process.[43] The basic principle here is that the reactant materials are adsorbed over the surface of the heterogeneous catalyst - the reaction site - concentrating their molecules there thus increasing their chances of reacting with each other.[44]

Figure 2.1. *Illustration of how adsorption of molecules happens on a catalyst surface, using hydrogen and ethene as an example*

The most important feature of the heterogeneous catalyst is the active sites found on the surface of the catalyst. Usually, these exposed surface sites have an anisotropic character due to the difference in atomic structure, to minimize the total surface energy. The different active sites are presented in **(Figure 2.2)** and are classified into corners, steps, terraces, edges, kinks and vacancies. These differences result in different chemisorption properties, selectivity and catalytic activity.[42 44] For example, in the hydrogenation of aldehydes over a Ru/C catalyst to produce α,β-unsaturated alcohols, competition between C=C and C=O bond hydrogenation occurs. C=O bond hydrogenation is highly favoured on planes, whereas C=C bond hydrogenation is favoured on edges.[44]

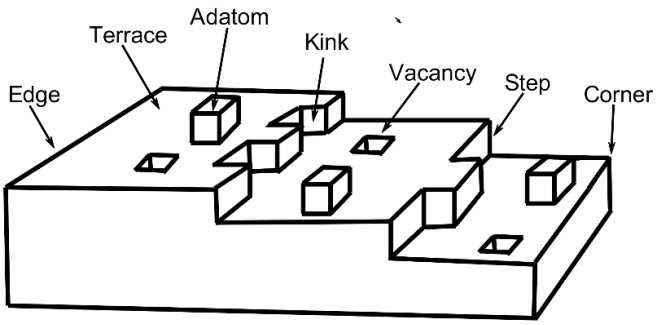

Figure 2.2. *Surface structure of a heterogeneous catalyst showing the different types of the possible adsorption sites that can facilitate the catalytic reaction*[45]

Heterogeneous catalysis involves several steps:[46]

- Reactant diffusion through the catalyst boundary
- Reactant diffusion through the catalyst pores
- Reactant adsorption on active sites
- Reaction of adsorbed substrates
- Desorption of products
- Product diffusion through the catalyst pores
- Product diffusion through the catalyst boundary

Heterogeneous catalysts are generally classified into bulk metal, metal oxides and supported metals, each serving specific purposes based on their desired function and the pre-existing knowledge of their chemistry and the chemical properties of the reactants.[47] In other words, a thorough understanding of the target reaction and the chemical properties of the reactants and catalyst is essential for selecting the appropriate catalyst.[48] In the context of this research, a catalytic system consisting of transition metals supported on a metal oxide was selected. Titanium dioxide (TiO_2) was used as a catalytic support, onto which gold, nickel, iron and ruthenium was doped.

2.2. Justification of catalyst choice

The choice of catalyst and support was motivated by literature reporting CO_2 reforming of methane (CH_4) on a transition metal (platinum) supported on a reducible oxide, ZrO_2.[41] Studies indicate that CO_2 reforming of CH_4 on Pt/ZrO_2 occurs via two mechanisms. The first path involves methane decomposition on Pt generating oxygen vacancies on the surface of the support. Subsequently, the carbon interacts with oxygen from the catalytic support to form carbon monoxide. [41]

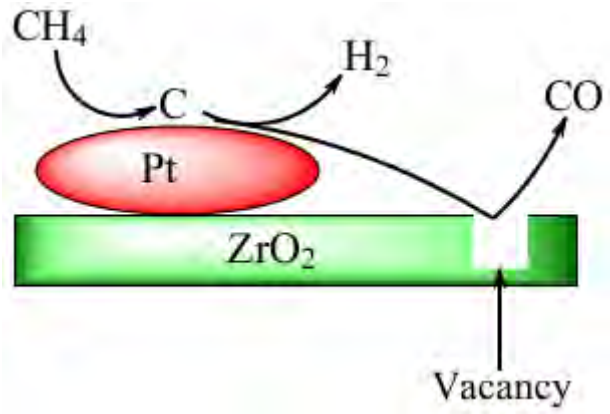

Figure 2.3. *Methane decomposition on a Pt particle subsequently generating an oxygen vacancy on the reducible metal oxide support*

The second path involves CO_2 adsorption and dissociation at the metal–support interface. Adsorption occurs at the oxygen vacancy that formed in the first path, followed by dissociation into CO and O which in turn replenishes the lost oxygen from the support for a continuous mechanism.[41 49]

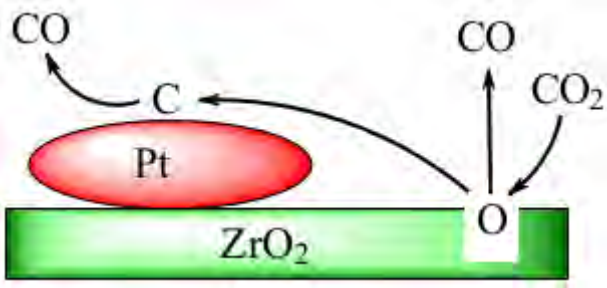

Figure 2.4. *Adsorption of the CO_2 molecule via the oxygen atom onto the oxygen vacancy that was formerly formed on the previous step*

The concept underlying our research was for the reactants to adsorb onto the bifunctional catalyst, as outlined below.

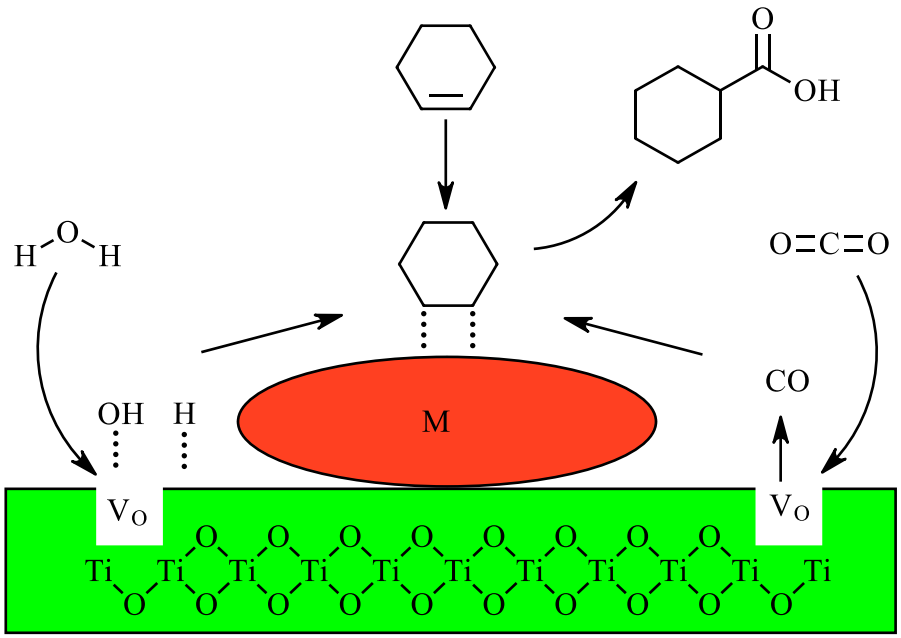

Figure 2.5. *Illustration of the possible interactions of the reactants with the catalyst system. The water molecule through the oxygen atom interacts with the oxygen vacancy (V_O) splitting into hydroxy radicals and hydrogen, CO_2 gets reduced to CO over the oxygen vacancy (V_O), cyclohexene adsorbs onto the supported transition metal*

Adsorption of the alkene takes place over the supported transition metal. This occurs through either π-complexing or di-σ-adsorption forming π-complexed double bonds, π-complexed π-allyl species, mono-σ-bonded alkanes and/or di-σ-bonded alkanes. The alkene adsorbs on the surface of the transition metal atoms with its π bond parallel to the plane of the surface atoms. This happens through associative adsorption whereby the π bond raptures and two σ bonds are formed between the two carbons which formerly had the π bond and the two surface transition metal atoms. This happens as opposed to dissociative adsorption whereby C-H bond is broken forming two σ bonds between the previously joined atoms and the surface of the metal.[47]

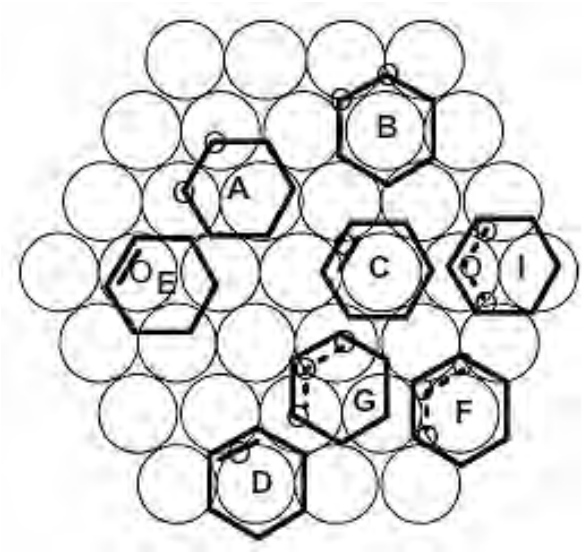

Figure 2.6. *Different possible modes, A-G, of interaction of cyclohexene with the metal surface and the species that form as a result* [47]

The adsorption sites represented by circles forming a hexagonal shape in **(Figure 2.6)** show a transition metal surface as face centred cubic (fcc) (111) where adsorption of alkenes, cyclohexene used as an example, takes place. More than one atom or group of atoms are involved in the catalysis. A and B shows possible locations of di-σ-adsorption forming 1,2-di-σ-$C_{1,2}$-cyclohexane. C, D and E shows possible locations of π-complexing forming π-$C_{1\text{-}2}$-cyclohexene. F, G, and I show possible locations of π-$C_{1\text{-}3}$-cyclohexene π allyl moiety. The mono-σ-C_n-cyclohexane species are indicated with one tiny circle at the carbon adsorbed on to the surface site. (The subscript letter n and numbers indicate the number of the carbon, e.g., carbon 1, carbon 2, etc., attached to the metal surface).[47]

i. Adsorption on the support

Reducible metal oxides such as TiO_2 have oxygen vacancies on their surfaces. These defects interact with the oxygen in the oxygen containing molecules resulting to their dissociation. The CO_2 is expected to adsorb on the oxygen vacancies which in turn dissociates into carbon monoxide, CO, and oxygen, O. The formed oxygen will then replenish the lost oxygen on the oxygen vacancy thus re-oxidising the TiO_2 in a similar way as in CO_2 reforming of methane, CH_4, on a transition metal, Pt, supported over a reducible oxide, ZrO_2.[41]

The adsorption of water takes place over the nanoparticles of the reducible metal oxide support (TiO_2). This can take place on the surface of the metal oxide[50] and at the oxygen vacancy (V_o)

formed as a result of a loss of an oxygen atom from the network on the crystal surface.[51] [52] On the surface of the reducible metal oxide, water can adsorb by dissociation or can adsorb molecularly at different facets and coverages depending on what adsorption is energetically favored.[50]

In reducible oxides dissociative adsorption of water on the oxide surface depends mostly on the position of the surface oxygen p orbital (O *2p* level). If the surface O *2p* level is located inside the band gap high above the valence band maximum, then these oxides will split water efficiently. During this adsorption, the O *2p* level experiences a downshift towards the valence band which results in a significant energy gain, enough to overcome the dissociation energy barriers on the surface, that facilitates water splitting.[50]

The scenario is different for TiO_2 since it has its O *2p* level buried within the valence band, therefore there is a slight downward shift of the O *2p* level, so the energy gain is very small to facilitate water splitting, therefore water adsorbs as a molecule on the surface of TiO_2. The intermolecular interactions between the adsorbed water molecules on the TiO_2 surface, hydrogen – hydrogen (H – H) repulsive forces and hydrogen – oxygen (H – O) attractive forces, induce large energy gain. This energy gain is significant to overcome the dissociation energy barriers on the metal oxide surface which in turn help water splitting into hydroxyl groups.

A hydroxyl group forms by the (-OH) group attaching to the titanium (Ti) site from dissociated water. The other hydroxyl group forms when the hydrogen from dissociated water attaches to the oxygen on the metal oxide surface, creating terminal and bridging hydroxyls[50], which is followed by the hydrolysis of Ti–O lattice bond.[53] [54]

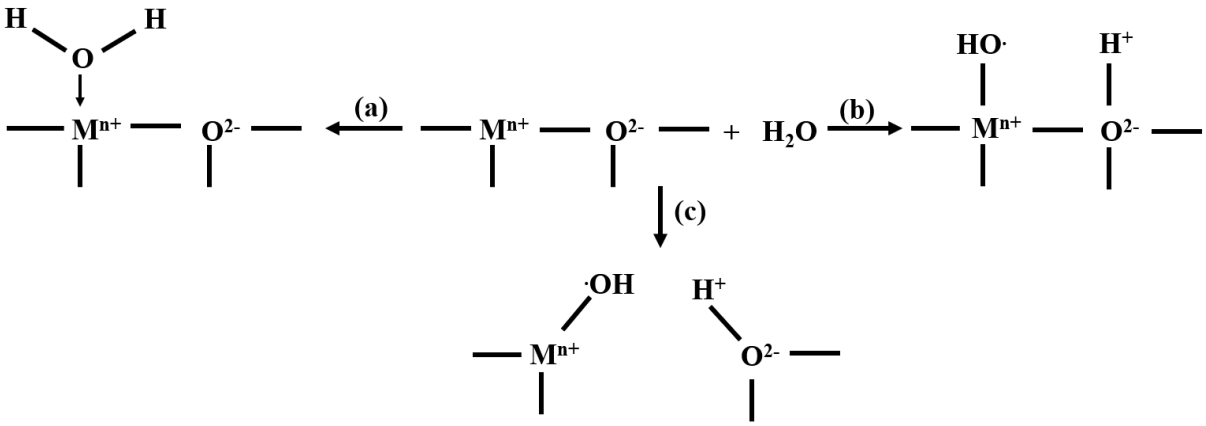

Figure 2.7. *Illustration of how water interacts with metal oxide surface (a) adsorption of water on metal site (b) dissociation of water molecule (c) hydrolysis of metal – oxygen bond*[53]

Water can also adsorb on defects, such as oxygen vacancies (V_O), on TiO_2. These electropositive centres, formed due to the loss of an oxygen atom on the metal oxide surface, interact with other oxygen containing species through the oxygen atom and thus causing a splitting of the water molecules.[51 53 55] As the water dissociates across the oxygen vacancy it forms bridging and terminal hydroxyls.[55 56] The (-OH) groups from water heals the vacancies through the oxygen atom, occupying the voids left behind by the oxygen atom that was removed when the oxygen vacancy was formed, therefore restoring the natural coordination of the Ti and O atom in the crystal lattice of the metal oxide surface.[53 56 57]

Figure 2.8. *Interaction of water with oxygen vacancies on the surface of reducible metal oxides (a) hydroxyl formed as water dissociates over oxygen vacancies (b) types of hydroxyls formed, I is a terminal hydroxyl, II is a bridging hydroxyl with hydrogen coordinated to two metal atoms, III is a bridging hydroxyl coordinated to three metal*[53 57]

Though adsorption, can take place at the coordinated surface Ti sites but the presence of oxygen vacancies on the surface of TiO_2 results in a competition for dissociation sites between water dissociating at the surface Ti sites and water dissociating at the oxygen vacancies. Nonetheless, the dissociation mechanism of water at the oxygen vacancies is more energetically favourable than dissociation at the surface Ti sites.[56]

All these adsorption modes of the reactants over the catalyst occurs *in-situ* as the reaction is taking place in the reaction vessel. **Figure 2.5** illustrates the postulated modes of adsorption of reactants and the desorption of the product.

2.3. Preparation of heterogeneous catalyst

Reactions occur on the surface of heterogeneous catalysts as reactants concentrate over the catalytic surface, thus accelerating the reaction.[47] It is important to have the supported metal highly dispersed over the metal oxide support to maximize active sites for the reaction.[58] The catalytic supports not only serve as a means of high dispersion of active phase but may also

participate in the catalytic activity, making the system a bifunctional catalyst; which was the aim of the catalytic system reported here.

During the preparation of a supported catalyst, a precursor solution with a desired amount of an active component is deposited on to the metal oxide support to achieve its optimal dispersion of active sites. Typically, for precious metals such as Au and Ru, low metal mass loading of 0.1 – 1% per mass of support is used to minimize the costs. On the other hand, for relatively cheap base metals such as Fe and Ni higher metal mass loading of 10 – 40% per mass of support is used to increase the space-time yield of the reactor.[59]

Preferably, precursor solutions are prepared using nitrate and carbonate salts where possible because they decompose easily during the catalyst's calcination step, thus avoiding potential catalyst poisoning.[60 61] Wet impregnation was used as opposed to dry impregnation because in wet impregnation migration of the precursor through the pores of the support happen through diffusion driven by concentration gradient therefore there is no pressure build up within the pores, caused by air bubbles, which will consequently lead to the collapse of pore structure of the support, leading to a decrease in the surface area for dispersion of active sites.[60 61]

On the other hand, in dry impregnation, migration of the precursor through the pores happens through capillary suction which traps and compresses the air bubbles within the pores and the resulting pressure build up collapses the pore structure of the support.[61] Precursor solutions are made using preferably nitrate and carbonate salts where possible because they decompose easily on the calcination step of the catalyst therefore are not capable of poisoning the catalyst.[60 62]Chloride and sulphide salts are avoided if possible because chloride and sulphide ions can act as poisons in some reactions.[60]

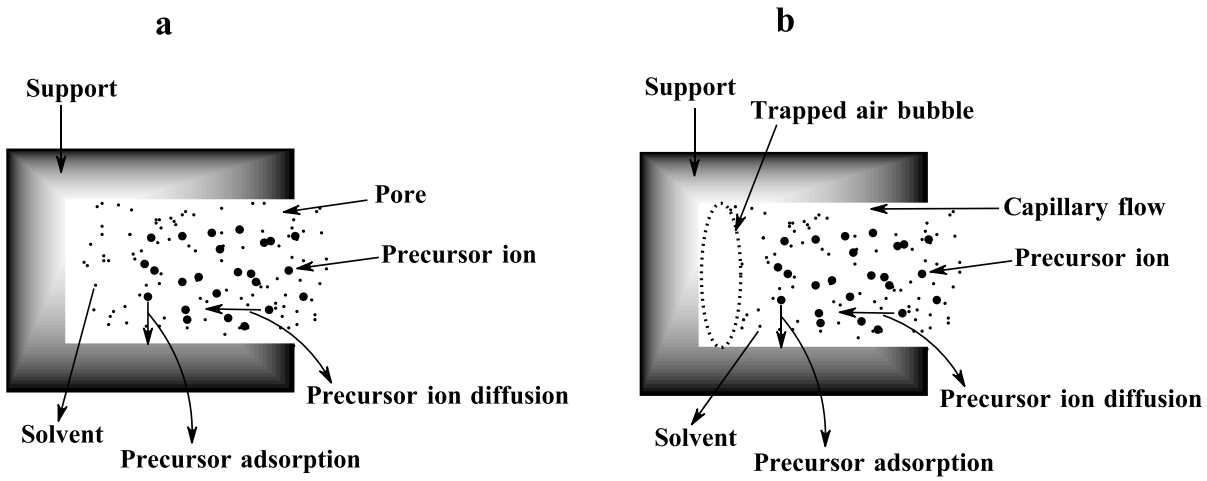

Figure 2.9. *Illustration of processes that happen during wet impregnation (a) and dry impregnation (b)*[60]

The next step involves a drying process to evaporate the solvent from the mixture to obtain the catalyst.[63] During the drying process, several critical aspects occur, including heat transfer from the surroundings to the wet support and mass transfer as vapour into the surroundings.[64] In this process there is a convective flow of solvent towards the external surface of support, diffusion of metal ions and adsorption of metal on to the support – thus affecting the distribution of the metal onto the support.[63 65]

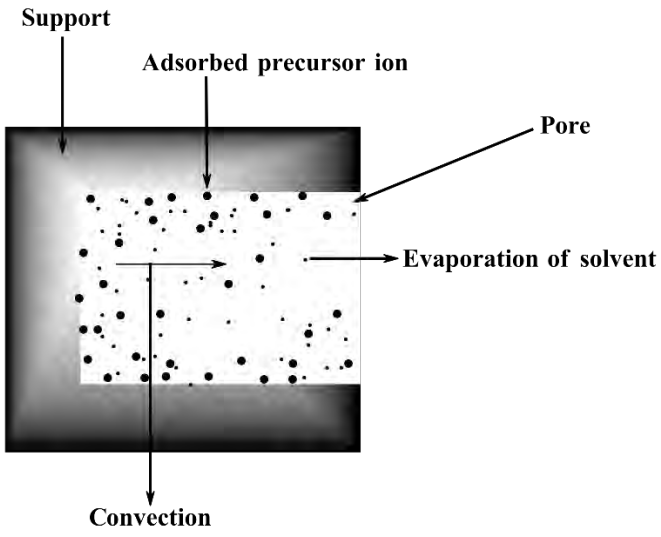

Figure 2.10. *Illustration of processes that happen during the drying process of the catalyst* [60]

The nitrate salts of Fe and Ni have low melting points (47.2 ℃ and 56.7 ℃ for Fe and Ni salts, respectively) and hence they are in a molten state during drying which also affects the distribution of the metal ions on the support.[59] Thus, the desired drying temperature should be above the melting point of these salts to afford uniform distribution, but also low enough to avoid non-uniform distribution on the support surface. In contrast, the chloride salts have high

melting points (254 ℃ and 500 ℃ for Ru and Au respectively) implying that drying temperature is below their melting points to avoid non-uniform distribution of the metals resulting from rapid flow of the solvents.

After the drying step, the catalysts are calcined at 600 ℃ to decompose the ligands coordinated to the metal salt as well as removing any solvent trapped within the support structure. Additionally, it ensures that the catalyst and support retains its structural integrity during the reaction.[60 66] Calcination is usually performed under flowing air or oxygen to burn any organic materials present.[60]

Finally, the catalysts were characterized to confirm the addition of metals onto the support and to probe their structural features. This was achieved using techniques such as:

- Powder X-ray diffractometry to study catalyst structure and chemical phases
- Brunauer–Emmett–Teller (BET) to calculate the surface area of the catalysts
- Transmission electron microscopy (TEM) to investigate morphological features
- Energy-dispersive X-ray spectroscopy (EDX) for elemental analysis of the catalyst and to confirm metal deposition onto the support
- Solid-state ultraviolet-visible spectrophotometry (UV-VIS) which will indicate absorbance changes that take place upon addition of the precursor ions.

2.4. Objectives

The main product that was targeted in this chapter is cyclohexanoic acid with the following objectives:

i. Preparation and characterization of different heterogeneous catalysts that are Au, Ru, Ni and Fe based supported over TiO_2.

ii. To use the prepared catalysts to facilitate the reaction between CO_2, H_2O and cyclohexene to produce cyclohexanoic acid

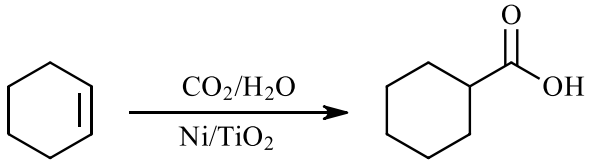

Scheme 2.1. *Illustration of the reaction that is expected to take place between equimolar amounts of cyclohexene (40 mmol), water (40 mmol) and 11 atm of CO_2 in the presence of Au/Fe/Ni/Ru supported on TiO_2*

3. HOMOGENEOUS CATALYSIS

3.1. Introduction

Industrially, only ~15% of all catalytic processes employ homogenous catalysts. This is mainly because most catalytic processes that produce the base chemicals, which serve as feed stocks for production of platform chemicals and other fine chemicals, require harsh conditions. As a result of the low thermal stability of homogenous catalysts, they are not applicable to these processes, and this is their main disadvantage in addition to the challenge of recovering them from the reaction media.

For example, the main source of chemicals, crude oil, requires high temperatures (>650 ℃) for it to be processed catalytically to produce other platform chemicals while the upper temperature limit of homogenous catalysts is only about 250 ℃. Herein, the objective is to produce an ester, which can be used as a substrate for production of other higher value-added chemicals, under mild conditions with the aid of a homogeneous catalyst.

In homogenous catalysis, the catalyst and reactant molecules are dispersed in the same phase (more often a liquid phase) in a reaction vessel for the duration of the reaction. At the molecular level, the catalyst may be present in different intermediate forms during the catalytic cycle. Homogenous catalysis involves the use of different types of catalysts, transition metal complexes, Bronsted and Lewis acid and base catalysts, organic catalysts and biological catalysts.[67] [68] For the purpose of this research, we will only focus on homogenous catalysts driven by transition metal complexes.

These type of catalysts are made up of a metal center surrounded by organic and/or inorganic ligands which are coordinated to the metal.[69] Each catalytically active entity acts as a single active catalytic site.[68] The catalytic activity depends on both the metal and the surrounding ligands, but generally the properties of the catalysts can be enhanced by modifying the ligand environment to tailor the catalyst for a specific selectivity and reaction rate,[67] therefore the ligand choice is important when developing an appropriate catalytic metal complex.[70]

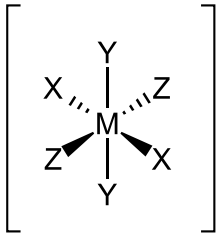

Figure 3.1. *Basic structure of an octahedral transition metal complex as an example*

For the metal to facilitate the reaction between the reactants, a vacant site in the metal centre is required to coordinate a molecule, initiating catalytic activity. The strength of substrate coordination determines the rate of the catalytic process; stronger coordination leading to a reduced rate of catalysis, and *vice versa*. Catalytic activation of substrates by these complexes typically occurs at the metal centre through different elemental steps, including:

i. Oxidative addition - happens when a molecule, AB, adds on to the complex through the breaking of a bond of that molecule into A and B then two new bonds metal-A and metal-B are formed between the metal and the molecule.

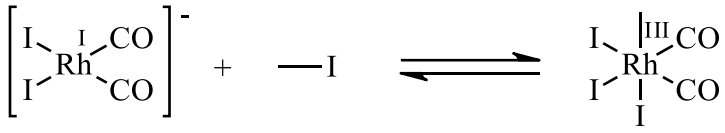

Scheme 3.1 *An example of oxidative addition process involving the incorporation of MeI onto* $[Rh(CO)_2I_2]^-$ *complex*

ii. Coordination – this is when a molecule, AB, interacts with the complex without the molecule losing its integrity remaining as AB with the alteration of the electron distribution within the molecule.

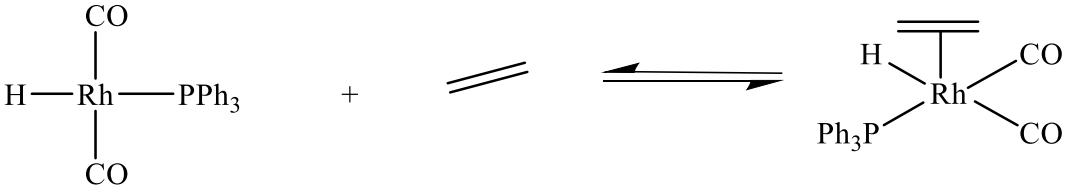

Scheme 3. 2. *Illustration of ethylene activation through coordination on to* $RhH(CO)_2PPh_3$ *metal complex*

iii. Migratory insertion - this is the reaction between the coordinated substrates within the complex. This happens through a vacation of the coordination site.

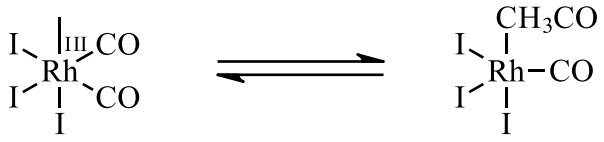

Scheme 3. 3. *An example of a reaction of methyl and Carbon monoxide within a complex via an insertion reaction following the oxidative addition of MeI on $[Rh(CO)_2I_2]^-$ complex.*

iv. Reductive elimination – this is the last step of the catalytic cycle. It is the opposite of the oxidative addition and an important step for the regeneration of the catalyst.

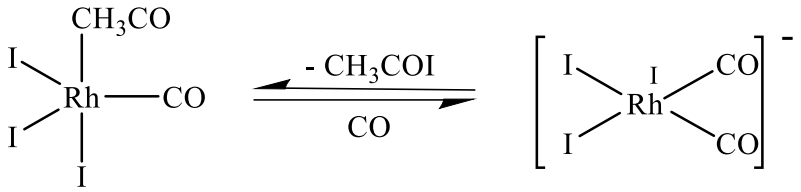

Scheme 3. 4. *Removal of CH_3COI from the complex via reductive elimination to regenerate the $[Rh(CO)_2I_2]^-$ complex.*

These steps in a catalytic cycle involve the conversion of a precursor complex into its active form, typically through ligand dissociation or interaction with a co-catalyst or promoter. Alternatively, the cycle involves the activation of reactant X by the catalyst and the subsequent activation of reactant Y by the product formed from the activation of reactant X. Lastly, the cycle involves an intramolecular reaction within the complex, leading to a product through reductive elimination, and eventually regenerating the catalyst.

Transition metals such as iron, cobalt, ruthenium, rhodium, iridium, platinum, and palladium have been widely employed to develop complexes for various catalytic reactions. The reactions that these metals have been used to catalyse include hydrogenation, hydroformylation, isomerization, polymerization, oligomerization, metathesis and carbonylation of olefins.[71] **Table 3. 1** summarizes the types of reactions and the corresponding metal complexes commonly used in catalytic reactions involving olefins.

Table 3. 1. *Summary of reactions from literature involving olefins and metal complexes generally used to catalyse them*

Reaction	Typical catalyst
Hydrogenation	$RhCl(PPh_3)_3$, $RuCl_2(PPh_3)_3$, $Co(CN)_5^{3-}$
Hydroformylation	$CoH(CO)_4$, $RhH(CO)_3$
Isomerization	$RhH(CO)(PPh_3)_3$, $CoH(CO)_4$, $Fe_3(CO)_{12}$
Polymerization	RhCl catalysts
Metathesis	Grubbs catalysts
Carbonylation	Co, Fe, Ru, Rh, Ni based carbonyl complexes

Though literature has reported several reactions based on catalytic transformation of olefins using different transition metals, this work will focus on the carbonylation reaction of olefins with CO_2 driven by $Ru_3(CO)_{12}$ as a transition metal-based catalyst.

3.2. Carbonylation of olefins with CO_2 catalyzed by $Ru_3(CO)_{12}$

A significant advancement in transition metal catalysis was the discovery of converting olefins to aldehydes using a cobalt catalyst in the presence of hydrogen and carbon monoxide. Subsequently, it was discovered that group 8 metal carbonyls can catalyse carbonylation reactions involving olefins and alkynes. The resulting product is a carboxylic acid or an ester when water or an alcohol was used, respectively, instead of hydrogen. Nickel was identified as the preferred metal for higher yields with alkynes; while cobalt, rhodium, iron, ruthenium, or palladium were found to be effective catalysts for carbonylation with alkenes. All of the above-mentioned reactions are carried out using carbon monoxide as a carbonyl source. This breakthrough paved the way for exploring various methods of achieving carbonylation reactions of olefins using alternative CO sources. These sources include formaldehyde, formic acid, formates and CO_2,[72] which is the surrogate in this study, and will be discussed in further detail.

There are literature reports that document the use of CO_2 as a CO source using ruthenium as a transition metal catalyst. This approach involves the *in-situ* reduction of CO_2 to CO which is subsequently incorporated into the double bond of the olefin.

3.2.1. Hydroformylation/reduction

The first report using $Ru_3(CO)_{12}$ as a catalyst for carbonylation of olefins was that of hydroformylation of cyclohexene in the presence of CO_2, hydrogen (H_2), lithium chloride (LiCl) as a promoter in N-Methyl-2-pyrrolidone (NMP) as a solvent. The main product of this reaction is cyclohexylmethanol at a yield of 86% and 3% of a minor product cyclohexanecarboxaldehyde. It was found that without LiCl, the complete hydrogenation of the olefin to an alkane took place. This means that the role of this salt is to suppress the hydrogenation to favor hydroformylation. This is reported to be a two-step reaction with a reverse water gas shift (RWGS) as a first step where H_2 reduces the CO_2 to CO which is then used for hydroformylation in the second step.[73]

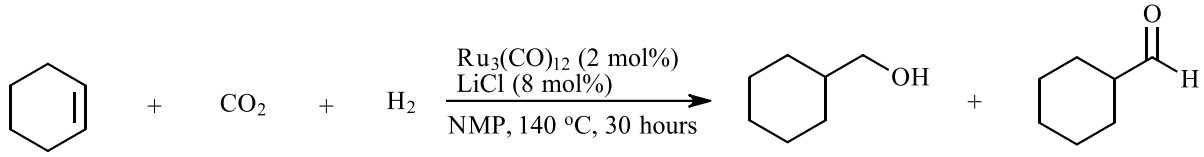

Scheme 3. 5. *Hydroformylation of olefins with CO_2 at (40 bars) and H_2 at (40 bars) in the presence of $Ru_3(CO)_{12}$ catalyst, LiCl promoter and N-Methyl-2-pyrrolidone solvent at 140 ^{O}C for 30 hours*

3.2.2. Hydroaminomethylation

This reaction involves a three step one-pot synthesis of saturated amines. It is similar to the above reaction, with an extra step involving a molecule with an N-H function and toluene as a solvent. The aldehyde formed from the in-situ hydroformylation of alkenes as outlined in the above reaction **(Scheme 3. 5)** undergoes condensation with the primary or secondary amine through the N-H function to give an imine/enamine which upon hydrogenation subsequently gives a corresponding saturated secondary or tertiary amine.[73 74]

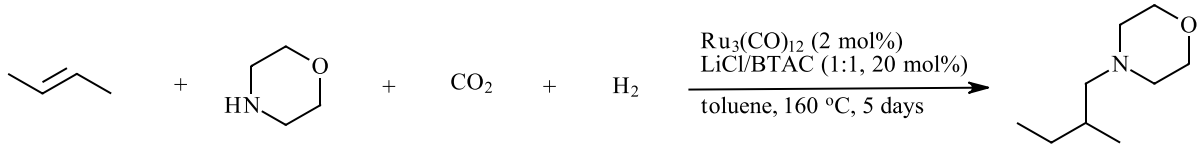

Scheme 3. 6*. Hydroaminomethylation of olefins with amines, CO_2/ H_2 (1:3 ratio) in the presence of $Ru_3(CO)_{12}$ (2 mol%), LiCl/ behentrimonium chloride (BTAC) (1:1) in toluene at 160 ^{O}C for 5 days*

3.2.3. Alkoxycarbonylation

The above reactions have opened different possibilities of using different substrates in carbonylation to obtain a variety of functionality. Recently, literature has reported a similar carbonylation reaction of olefins with CO_2, methanol (MeOH) as a reagent and a solvent in the

presence of an ionic liquid, 1-Butyl-3-methylimidazolium chloride [BMIM]Cl. In this reaction, MeOH was used as a CO_2 reducing agent and giving methyl cyclohexanoate as a product instead of an aldehyde. It is reported that the reaction is driven by the reduction of CO_2 by MeOH to CO or a formate through the hydrogen borrowing reaction. The alkoxycarbonylation is the reaction of interest in our work which we carried out and reported on our findings.

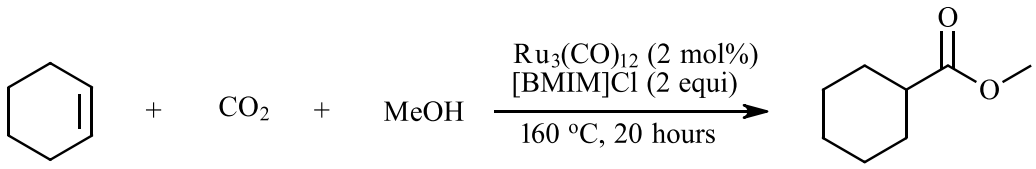

Scheme 3. 7. *Alkoxycarbonylation of olefins with CO_2 (40 bar) and methanol (20 ml) in the presence of $Ru_3(CO)_{12}$ (2 mol%) catalyst, 1-butyl-3-methylimidazolium chloride (2 equivalents) at 160 ^{O}C for 20 hours*

3.3. Objectives

The focus of our study in this chapter was on reproducing the methyl cyclohexanoate at lower CO_2 pressure, 11.568 atm, following the alkoxycarbonylation reaction in **Scheme 3. 7** with the following objectives.

i) Incorporating a carbonyl and a methoxy group from CO_2 and MeOH respectively into the cyclohexene structure catalyzed by $Ru_3(CO)_{12}$ obtained from a supplier.

ii) To determine the influence of additives such as [BMIM]Cl on the rate of conversion. In this instance, [BMIM]Cl was synthesized.

iii) In order to saturate the reaction solution with CO_2, the effect of dry ice was probed.

4. MATERIALS AND METHODS

4.1. Heterogeneous catalysis

4.1.1. Preparation of TiO_2 supported catalysts

For the synthesis of metal supported over a metal oxide, gold(III) chloride, nickel(II) nitrate hexahydrate, iron(III) nitrate nonahydrate and ruthenium(III) chloride salt precursors were used as sources of gold, nickel, iron and ruthenium respectively. Titanium (IV) oxide nanopowder of 21 nm particle size was used as a support of the above metals. 0.5% (11 mg) metal loading of Au and Ru per mass (2 g) of TiO_2 was used and 25% (0.75 g) metal loading of Fe and Ni per mass (2 g) of TiO_2 was used to obtain maximum dispersion and minimize the chances of agglomeration of active sites.

The TiO_2 support was firstly damped with 5ml of water then a precursor solution of each metal, made by dissolving the respective mass of precursor salt in 5ml of water, was added dropwise to their respective wet support. It is important to achieve a uniform distribution of the active sites on to the support therefore each mixture was continuously stirred at room temperature for 2 hours with a magnetic stirrer until a uniform mixture was obtained. Next, the solvent was evaporated out by drying each mixture in the oven at 70 ℃ for nitrate salts and 100 ℃ for chloride salts for 12 hours to try to achieve a uniform distribution of the active sites. After drying, the obtained catalysts were each transferred to a horizontal furnace for calcination at 550 ℃ for 16 hours under air flowing at 15 l/min.

4.1.2. Preparation of black Ru complex from $Ru_3(CO)_{12}$

The observation of a solution colour change, from pale yellow to black, prompted us to heat the orange $Ru_3(CO)_{12}$ crystals prior to performing the carbonylation reaction. Mild heating (70 ℃) of the orange $Ru_3(CO)_{12}$ crystals revealed that the catalyst itself undergoes a colour change from orange to black upon heating. A comprehensive literature survey revealed limited reports documenting this colour change – the significance being that $Ru_3(CO)_{12}$ might not be the only catalytically active species. In order to investigate this phenomenon, we carefully prepared all possible forms of $Ru_3(CO)_{12}$ (depending on the colour of the crystals). This was achieved by placing the orange $Ru_3(CO)_{12}$ in an inert atmosphere (argon gas was used) in a closed vessel at 70 ºC. The crystals were thinly and evenly spread across the surface of the container to increase the rate of conversion. The sample was left to fully transform from an

orange complex to a black complex for 3 weeks, was removed and stored at room temperature for further analysis.

4.1.3. Application of catalysts

Reactions were carried out in a stainless steel Berghof BAR 845 pressure reactor (150 bar/250 ℃/Bj. 86) equipped with a 250 ml teflon vessel, a lid with a teflon interior lining, magnetic stirrer, feeding valve connected to a CO_2 gas line, pressure gauge, safety rapture and a heating furnace. The autoclave was heated to 150 ℃ followed by the addition of the reactants, cyclohexene (40 mmol), water (40 mmol) and catalyst (25 mg). The autoclave was then pressurized with gaseous CO_2 (11.578 atm). The outlet was open for at least 1 minute to flush out the air that was inside, then closed to allow the reaction to run for 48 hours. At the end the autoclave was allowed to cool down to room temperature. The reaction mixture was then taken for analysis on GC-MS.

4.2. Homogenous catalysis

4.2.1. Synthesis of 1-Butyl-3-methylimidazolium chloride [BMIM]Cl

Preparation of [BMIM]Cl was carried out in a reflux set-up using equimolar ratios of 1-methylimidazole (15 ml, 0.183 mol) and 1-cholorobutane (19 ml, 0.183 mol) under argon atmosphere for 48 hours at 70 ℃ with continuous stirring on a hotplate in an oil bath. At completion, the solution was cooled to room temperature. Two phases were formed with the top layer being the unreacted material which was discarded. The product was washed 3 times using fresh ethyl acetate with each wash in a round bottom flask (using a separating funnel delays the process and causes a loss of product because it is viscous and sticky). After the wash, the product was heated in the oven overnight to remove the ethyl acetate. The small traces of ethyl acetate were removed under vacuum using a rotary evaporator at 70 ℃ for 2 hours and a pale-yellow viscous product was obtained.

4.2.2. Synthesis of methyl cyclohexanoate

Reactions were carried out in a stainless steel Berghof BAR 845 pressure reactor (150 bar/250 ℃/Bj. 86) equipped with a 250 ml teflon vessel, a lid with a teflon interior lining, magnetic stirrer, feeding valve connected to a CO_2 gas line, pressure gauge, safety rapture and a heating furnace. The autoclave was heated to 160 ℃ then added the mixture of [BMIM]Cl (3.48 g, 20 mmol), cyclohexene (1 ml, 9.87 mmol), methanol (20 ml, 494.3 mmol) and $Ru_3(CO)_{12}$ (63.9

mg, 0.1 mmol). The autoclave was then pressurized with CO_2 (11.578 atm, 118 mmol). The outlet was open for at least 1 minute to flush out the air that was inside, then closed to allow the reaction to run for 2, 4, 8, 12, 24 and 48 hours. At the end the autoclave was allowed to cool down to room temperature. Then reaction mixture was firstly sampled by head space analysis using a 100 μm polydimethylsiloxane (PDMS) solid phase microextraction (SPME) fiber bonded to fused silica with gentle heating at 35 ℃ on a hotplate for 20 minutes in a airtight vial to extract product from the mixture which was then analyzed using GC-MS. Secondly, the product was distilled from the mixture then analyzed by GC-MS by syringe injection. This sampling methods were done to avoid injecting the ionic liquid into the GC column since it does not boil and is not volatile therefore would block the column.

4.2.3. Control experiments with dry ice

Control experiments were conducted in a similar manner to the reactions highlighted in **section 4.2.1**. Solid CO_2 (about 30 g) was added to the mixture in the autoclave followed by gaseous CO_2, in an identical procedure as previously mentioned.

4.2.4. Control experiments without CO_2

Reactions were run in the similar manner as those in (**section 4.2.1**), in the absence of CO_2. The reaction mixture was purged with argon gas to expel any dissolved CO_2, in order to create an inert environment.

4.2.5. Control experiments with methanol-D_4

Experiments were performed in an analogous manner to that described in **section 4.2.1**, with the addition of 1 ml CD_3OD to 19 ml CH_3OH to reduce the expenses.

4.2.6. Control experiments without $Ru_3(CO)_{12}$

Reaction was run in the similar manner as those in **section 4.2.1** in the absence of $Ru_3(CO)_{12}$ catalyst.

4.3. Instrumentation

4.3.1. Gas chromatography-mass spectrometry (GC-MS)

Qualitative and quantitative analysis of synthesis products was performed on an Agilent technologies 7890A gas chromatograph and 7693 autosampler coupled with an Agilent technologies 7000A mass spectrometer triple quadrapole. The gas chromatograph was equipped with a Restek 13623 Rxi®-5sil MS capillary column (30 m x 250 μm x 0.25 μm). The following GC method was used: injection source, manual; inlet temperature, 250 ℃; carrier gas, Helium (40 psi on cylinder); pressure, 1.778 psi; total inlet flow 87.23 ml/min; septum purge flow 3ml/min; injection mode, split; split ratio, 150 : 1; control mode flow, 0.55781 ml/min; holdup time 1.8415 min; oven temperature program, 45 ℃ for 2 min, ramp to 75 ℃ at 25 ℃/min and hold for 1 min, ramp to 100 ℃ at 50 ℃/min and hold for 1 min, ramp to 150 ℃ at 100 ℃/min and hold for 1 min, ramp to 250 ℃ at 100 ℃/min and hold for 1 min. The MS method was as follows: thermal auxiliary temperature, 250 ℃; ion source, electron ionization; source temperature, 230 ℃; fragmentation energy, 70 eV; gain, 0.5; solvent delay, 0.5; peak width, 0.7 sec; scan type, MS 1; scan time 0.25 sec; acquisition range, 10 – 500 m/z.

4.3.2. Fourier transform infra-red spectroscopy (FT-IR)

ATR-FT-IR analysis was for structural characterization of [BMIM]Cl and $Ru_3(CO)_{12}$ catalysts. This was performed using a PerkinElmer spectrum 100 FT-IR spectrometer (PerkinElmer, USA). The spectra were obtained in attenuated total reflection (ATR) mode, 24 scans were run at a resolution of 4 cm^{-1} spanning the frequency range of 4000 to 600 cm^{-1}.

4.3.3. Nuclear magnetic resonance spectroscopy (NMR)

^1H NMR spectrum was recorded on a Bruker Avance III 600MHz spectrometer. Approximately 10 mg of sample was dissolved in 0.7 ml deuterated chloroform ($CDCl_3$). The sample was then transferred to a NMR tube and loaded onto the instrument for analysis. 16 scans were run for the experiment and the chemical shifts are reported in ppm.

4.3.4. Ultraviolet-visible (UV-VIS) spectrophotometry

Optical properties of the heterogeneous catalysts and metal oxide support were investigated using a PerkinElmer Lambda 950 UV-Vis diffuse reflectance NIR spectrophotometer in the range of 200 to 800 nm at a scan speed of 300 $nm.min^{-1}$.

4.3.5. Powder X-ray diffraction (PXRD)

The crystal structure of all catalysts was studied using PXRD. Their diffraction patterns were recorded using Bruker D2 phaser 2nd generation fitted with a Cu-Kα radiation source and Lynxeye detector. Radiation wavelength was 1.54184 Å and produced at 30 kV and 10 mA. Diffractograms were recorded at a 2θ range of 10-100º with step size of 0.04º while the PSD opening was 4.859º.

4.3.6. Transmission electron microscopy (TEM)

Morphology, particle size and arrangement of heterogeneous catalysts were studied using transmission elecron microscopy. Images were collected with a ZEISS Libra 120 Standard, operated at 120 kV, and Olympus Megaview G2 camera.

4.3.7. Energy-dispersive X-ray spectroscopy (EDX)

Data was collected on an Oxford INCA Penta-FET-X3 Si(Li) detector, accelerating voltage, 20 kV; livetime, 20 sec; tilt, 0; azimuth, 0; elevation, 45 degrees; real time, 29.31; magnification, 21314 X; normalized processing; number of iterations, 5; total spectrum counts, 94788.

4.3.8. Thermogravimetric analysis (TGA)

Decomposition studies were performed using a PerkinElmer TGA 4000. 2 – 5 mg of sample was loaded into the sample holder at 30 ℃, with nitrogen gas flow of 20 ml/min. For all isothermal analyses, the heating rate was set to 10 ℃/min until it reached the intended temperature, following this was a temperature hold time of 240 minutes. Non-isothermal analyses were performed at a heating rate which was set to 10 ℃/min until the required temperature was reached.

4.3.9. Differential Scanning Calorimetry (DSC)

Exothermic and endothermic studies were performed using a TA DSC 250. 2–5 mg of sample was placed in an aluminium pan and loaded onto the sample holder in a furnace at 30 ℃ with nitrogen flowrate of 50 ml/min. All analyses were non-isothermal with a heating rate of 10 ℃. Analyses without cycles was performed by heating the sample to 255 ℃. The analysis with 5 cycles was performed by heating the sample to 170 ℃ followed by cooling to 30 ℃. This step was repeated 5 times. On the last cycle, the sample was heated to 255 ℃.

4.4. Materials

Gold(III) chloride ($AuCl_3$), Nickel(II) nitrate hexahydrate ($Ni(NO_3)_2{\cdot}6H_2O$), Iron(III) nitrate nonahydrate ($Fe(NO_3)_3{\cdot}9H_2O$, Ruthenium(III) chloride ($RuCl_3$), cyclo-tris(tetracarbonylruthenium)(3 Ru—Ru) ($Ru_3(CO)_{12}$), Titanium dioxide (TiO_2), 1-methylimidazole ($C_4H_6N_2$), 1-chlorobutane (C_4H_9Cl), cyclohexene (C_6H_{10}) and methanol (CH_3OH) were all purchased from Sigma Aldrich. Ultra-pure water was obtained from the biochemistry department at Rhodes university, prepared using a Milli-Q water purification system. Dry CO_2 cylinder was purchased from Afrox.

4.5. Conclusion

In this chapter, we outlined the synthesis procedure and application of the catalysts, Au/TiO_2, Fe/TiO_2, Ni/TiO_2 and Ru/TiO_2, which were used in the heterogeneous catalysis section of the work. All the catalysts were prepared using wet impregnation method. A well detailed procedure of their application in a reaction between cyclohexene, water, and CO_2 in an attempt to synthesize cyclohexanecarboxylic acid at 150 ℃ for 48 hours was given.

A detailed application of $Ru_3(CO)_{12}$ as a catalyst in a homogenous catalytic reaction between cyclohexene, CO_2 and methanol in the presence of an ionic liquid, $[BMIM]^+Cl^-$ as a promoter was outlined. The synthesis procedure of the ionic liquid using and ATR-FT-IR spectroscopy were well detailed. Additionally, the preparation of black Ru complexes from $Ru_3(CO)_{12}$ was outlined.

All techniques, solid-state UV-VIS, TEM, EDX, PXRD, ^1H NMR, ATR-FT-IR, TGA, DSC and GC-MS used in this work were described in detail.

5. Results and Discussion

5.1. Heterogeneous catalysis

5.1.1. Catalyst characterization

The initial step involved the preparation of the catalysts intended for use in our reactions, followed by their characterization using several techniques. The outcomes of these processes are detailed below:

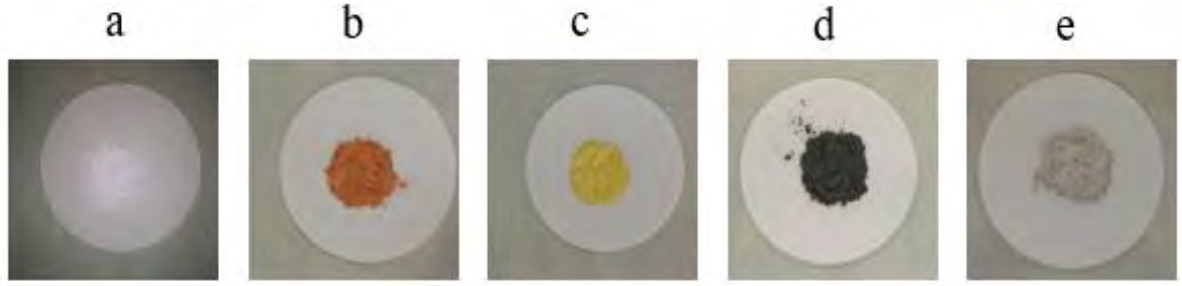

Figure 5. 1. *Images illustrating the support and catalysts after calcination. (a) white; TiO_2 bare support (b) orange; Fe/TiO_2 (c) yellow; Ni/TiO_2 (d) emerald green; Ru/TiO_2 (e) grey; Au/TiO_2*

The images of catalysts post calcination are displayed in **Figure 5. 1**, illustrating the differences between the catalysts. The bare TiO_2 support is white but with addition of metal precursors it changes to various colors which is the first indication that the metals have been successfully deposited onto the support.

These catalysts were then characterized using solid-state ultraviolet-visible spectrophotometry (UV-VIS), powder X-ray diffraction (PXRD), transmission electron microscopy (TEM), energy-dispersive X-ray spectroscopy (EDX) and Brunauer–Emmett–Teller (BET).

Optical properties of the bare support and the catalysts were investigated using solid-state UV-VIS spectrophotometry as a relatively sensitive technique in order to verify that the metals have been deposited onto the support. Analysis of the UV-VIS spectra were conducted to examine changes in absorbance and the band gap energy of the metal oxide support after transition metal deposition.

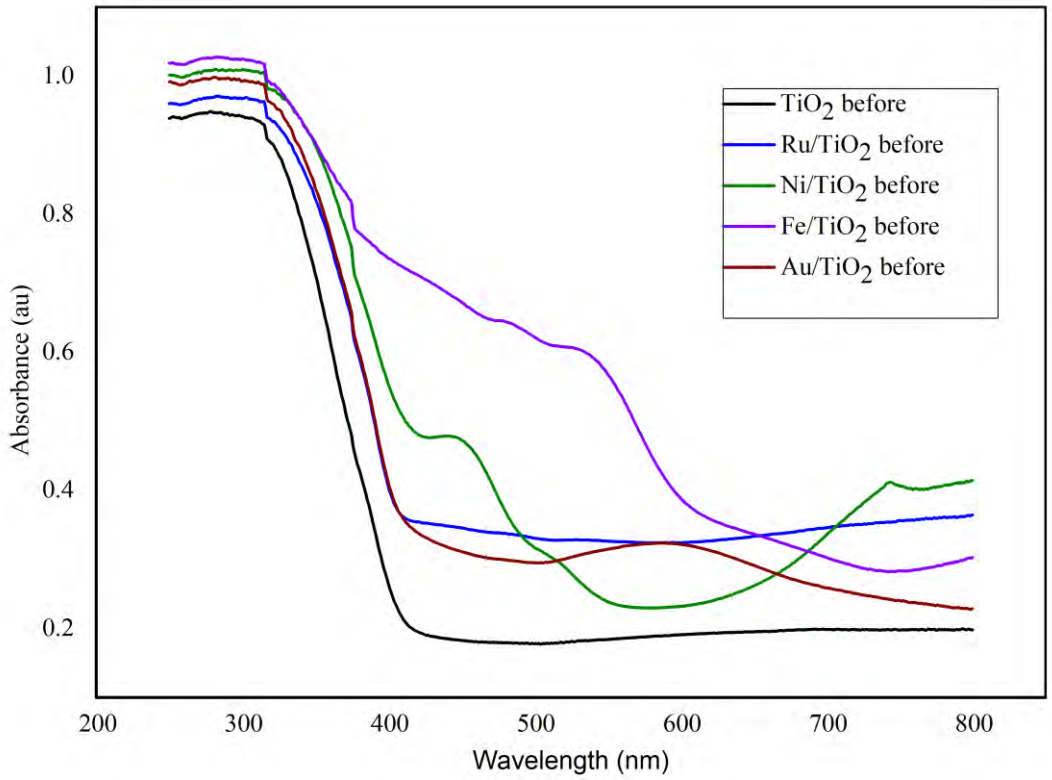

Figure 5. 2. *UV-Vis spectrum of the bare support (TiO_2) and that of the rest of the catalysts made of different metals (Au, Fe, Ni, and Ru) supported over TiO_2*

In the absorption profile of the bare TiO_2 there is minimal absorbance changes from 800 nm to 422 nm, followed by a sharp increase in absorbance at lower wavelengths. After the addition of different metals on to TiO_2, its absorption profile changed significantly for the transition metals we investigated. The profile of Ni/TiO_2 reveals that there is absorbance in the visible region which decreases until 600 nm then starts increasing abruptly from 0.23 au at 560 nm until it reaches maximum absorption of 1 au at 286 nm with an extra peak at 440 nm. In the absorption profile of Fe/TiO_2 there is an immediate sharp increase of absorbance in the visible region from 0.28 au at 730 nm to 1.02 au at 286 nm with an extra peak at 525 nm.

Ru/TiO_2 has a similar absorption profile pattern to that of bare TiO_2, but with a higher absorbance displayed in the 800-422 nm wavelength region. The absorbance then increases sharply from 0.36 au at 410 nm until it reaches maximum absorbance of 0.97 au at 286 nm. In the absorption profile of Au/TiO_2 there is an absorbance peak at 588 nm then the absorbance starts to increase sharply from 0.30 au at 461 nm until it reaches a maximum absorbance of 0.99 au at 286 nm.

The band gap energies of all the catalysts were calculated and compared to that of a bare support in order to verify their deposition onto the support. Furthermore, it was used as an indicator to establish whether the interaction between the metals and support is physical or chemical in nature. These calculations were performed using Tauc's method[75 76] of determining the band gap energy and are shown in the appendix.

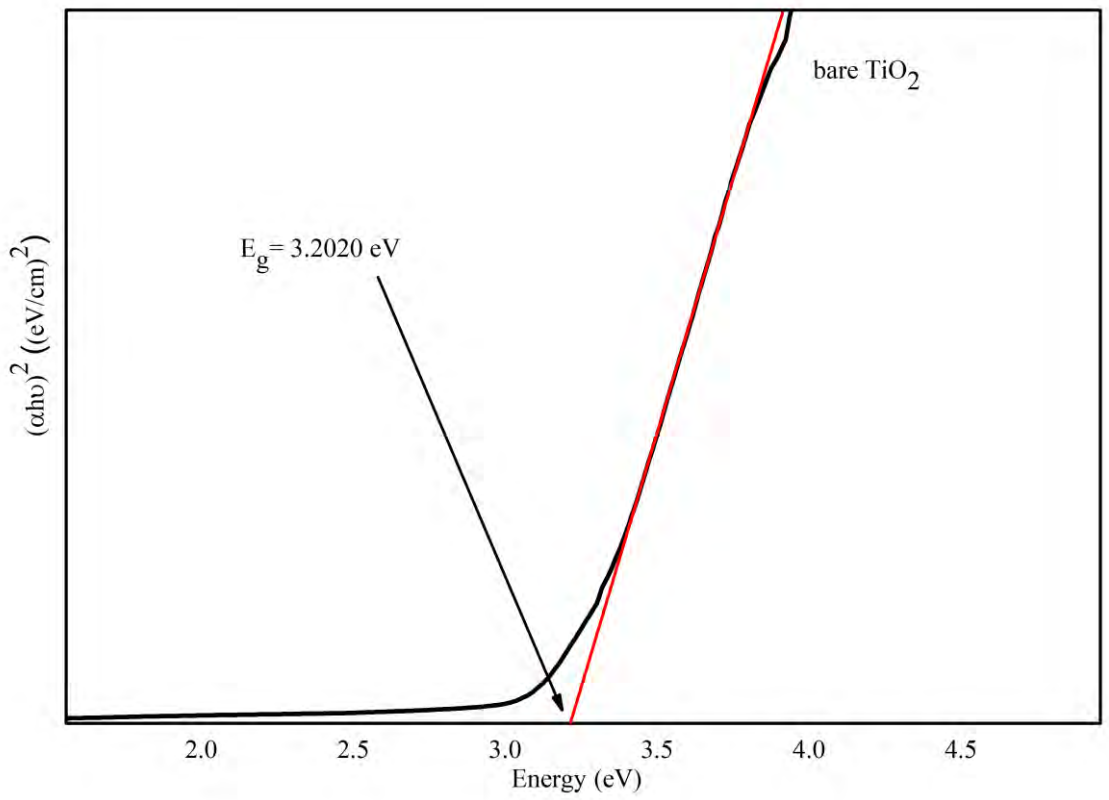

Figure 5. 3. *Determination of the band gap energy (E_g) of the bare TiO_2 from Tauc plots with the linear part extrapolated to x-axis with the red line for comparison after depositing different supported metals onto it*

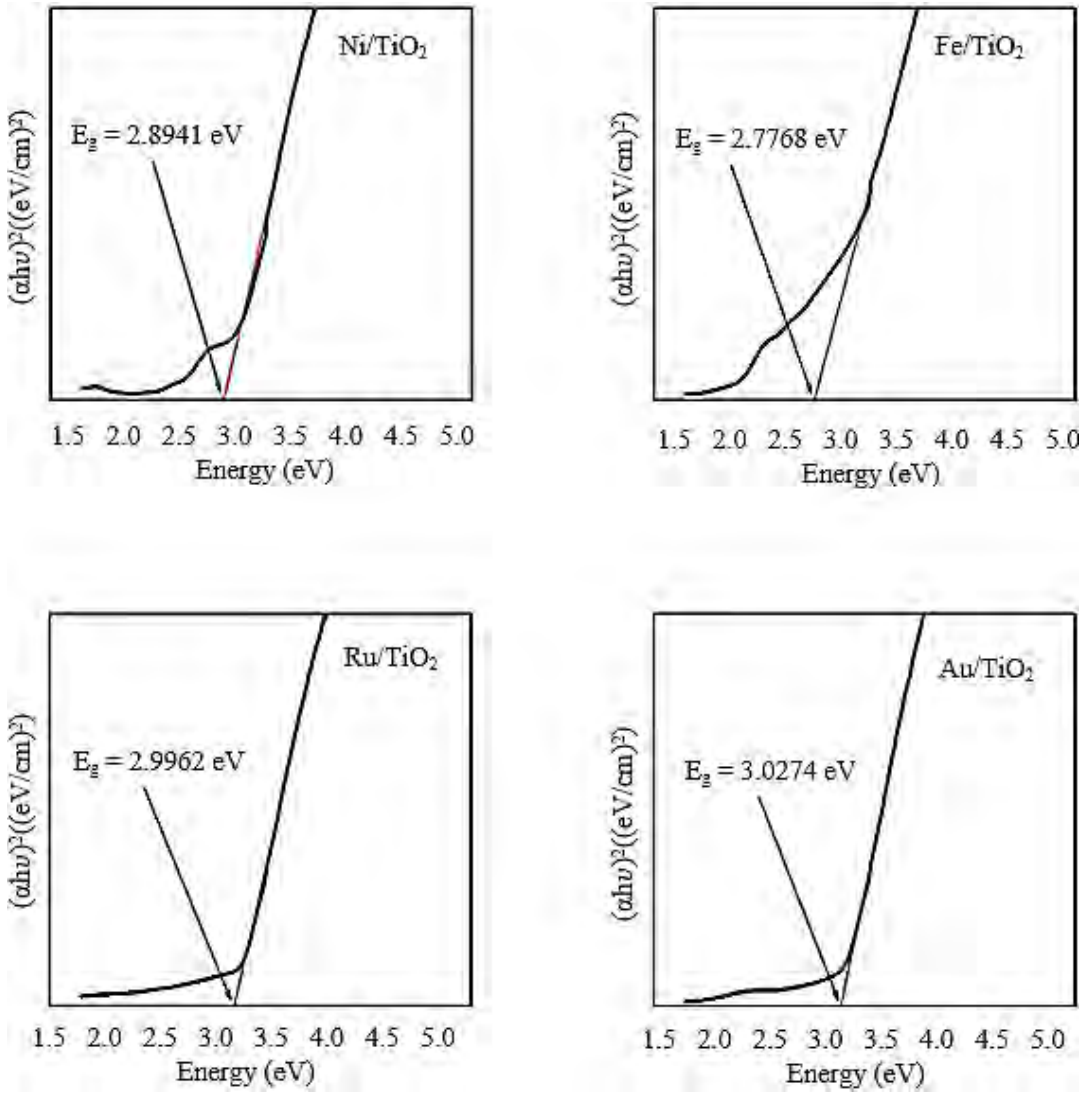

Figure 5. 4. *Determination of the band gap energy (Eg) of Ni/TiO2, Fe/TiO2, Ru/TiO2 and Au/TiO2 from the Tauc plots with the linear part extrapolated to x-axis with the red line, to highlight the changes with deposition of each metal*

From the band gap energies obtained in (**Figure 5.3 and Figure 5.4**), it is clear that with addition of a metal on to the support the band gap energy of TiO_2 is lowered. The value of the band gap obtained for the bare TiO_2 is 3.2020 eV, with deposition of Ni the value decreased to 2.8942 eV, 2.7768 eV for Fe, 2.9962 eV for Ru, and 3.0274 eV for Au. Generally, the band gap energy was lowered significatly for Fe and Ni compared to Au and Ru, which could be attributed to the larger amount used for Fe and Ni deposition. The changes in the band gap energy with addition of the respective metal indicates a chemical, rather than physical interaction, between the metal and the metal oxide support.

The structural properties of the bare TiO_2 and the catalysts were characterised using PXRD for the analysis of their diffraction patterns. Commercially procured TiO_2 was characterised to identify its phase before use. This was done since TiO_2 naturally exists as three main

polymorphs which are rutile, anatase and brookite - with the latter being less stable therefore less likely to occur.[77] The metal oxide support was also characterised post-calcination, in order to establish if any phase changes occurs during calcination, since elevated temperatures is known to convert brookite to anatase as well as rutile.[77] [79] Finally, the catalysts were characterised using PXRD to identify their crystalline structure and also determine if any distortions occurred in the TiO_2 crystal lattice.

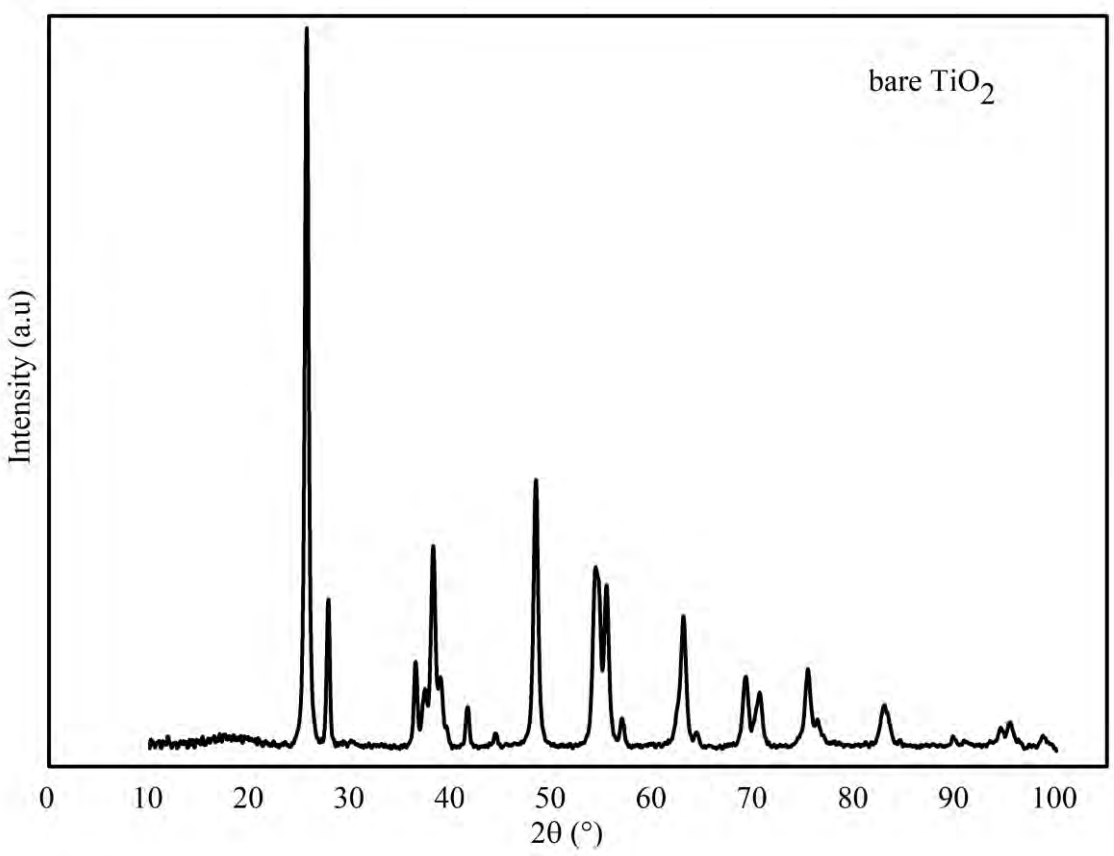

Figure 5.5. *X-ray diffractogram displaying the diffraction pattern of the bare TiO_2 before and after calcination*

The diffractogram of untreated TiO_2 displays peaks at 25.57˚, 27.74˚, 36.39˚, 38.10˚, 41.54˚, 48.24˚, 54.25˚, 55.33˚, 62.88˚, 68.91˚, 70.41˚, 75.37˚, 82.90˚. These peaks indicate a mixture of anatase and rutile phase in the TiO_2 sample with the peaks at 25.57˚, 38.10˚, 48.24˚, 54.25˚, 62.88˚, 68.91˚, 70.41 and 75..37˚ corresponding to anatase phase diffraction pattern[79] [80] while the peaks at 27.74˚, 36.39˚, 41.54˚, and 55.33˚ correspond to rutile phase diffraction pattern[77] [81]. The same sample of bare TiO_2 charcterised with PXRD before calcination was calcined at 550 ℃ and was analysed on PXRD again to check if there is any change in the diffraction pattern with calcination. The result is that the diffraction pattern before and after calcination is exactly the same meaning no phase transformation during calcination.

Figure 5.6 shows the PXRD patterns of the catalysts produced in this study. Illustrated in the diffraction pattern of Ni/TiO_2 we observe an additional peak at 33.38˚ which corresponds to the presence of Ni metal ion[82], and there is a minor shift in the diffraction peaks of TiO_2 to lower diffraction angles. This suggests a disruption in the crystalline structure of TiO_2 upon addition of Ni. This relates to the unit cell expansion distorting the lattice structure of TiO_2 as the Ni-ion is incorporated into the crystal lattice. The distortion is attributed to the larger size of the Ni^{2+} cation which has the ionic radius of 0.72 Å, compared to that of the Ti^{4+} cation which has an ionic radius of 0.68 Å. The incorporation of Ni^{2+} cation into the TiO_2 could possibly lead to the formation of oxygen vacancies on the surface of TiO_2.[79]

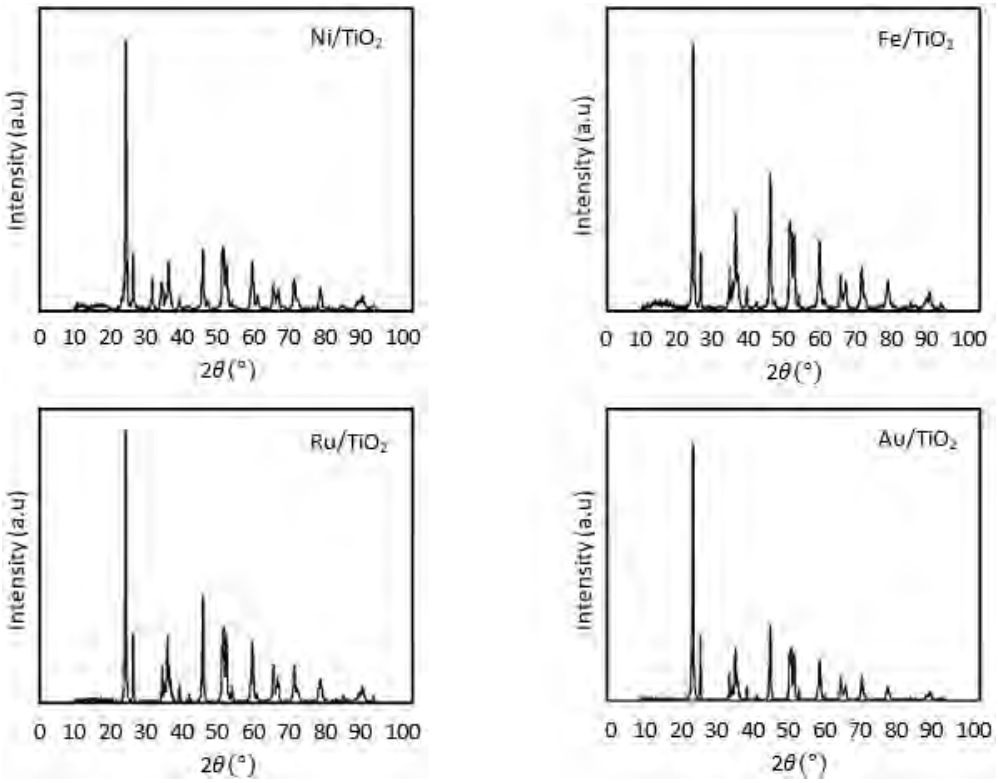

Figure 5.6. *X-ray diffractograms displaying the diffraction pattern of Ni/TiO_2, Fe/TiO_2, Ru/TiO_2 and Au/TiO_2 after calcination*

The diffraction pattern of Fe/TiO_2 is identical to that of bare TiO_2. The absence of the Fe peaks in the diffraction pattern shows that there was minimal distortion of the TiO_2 crystal lattice upon Fe-ion incorporation. This is because the size of the Fe^{3+} cation (0.64 Å) is similar to that of Ti^{4+} (0.68 Å).[80]

The diffraction patterns of Ru/TiO_2 and Au/TiO_2 are identical to that of bare TiO_2, there with no peaks indicating the presence of Ru or Au. The absence of these peaks is related to the amount of salts used as precursors to make these catalysts. Since low amounts were used, the metal ions may have been insufficient to be incorporated into the lattice structure of TiO_2. An

alternative hypothesis could be that the Ru and Au metal ions were present in amounts below the detectable limitations of the instrument.

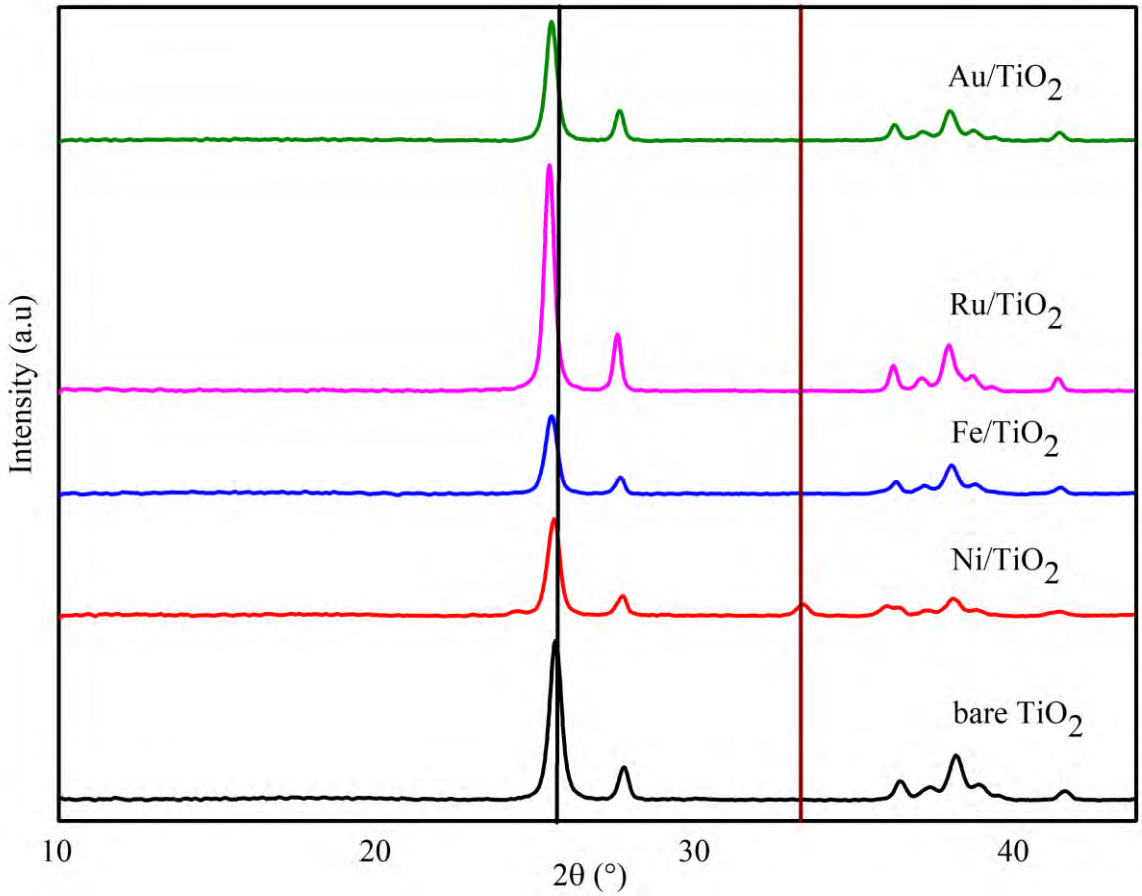

Figure 5.7. *Merged X-ray diffractograms of the catalysts and support at a selected region to demonstrate the tiny shift of the peaks, indicated by the black vertical line, and to demonstrate the presence of an extra peak in the Ni/TiO_2 catalyst at 33.38˚, indicated by the brown line.*

EDX elemental mapping was used to confirm the elemental composition of the bare TiO_2 and catalysts. The spectrum of bare TiO_2 shows only the expected peaks of titanium (Ti) and oxygen (O), indicating its purity. From **Figure 5.9**, it is evident that the modification of TiO_2 with the transition metal cations shows the additional peaks of the corresponding metal used to prepare the catalysts. Unfortunately, due to instrumental software limitations, we could not accurately integrate the peak areas in order to gain insight to the relative stoichiometric quantities of each element in the prepared catalyst.

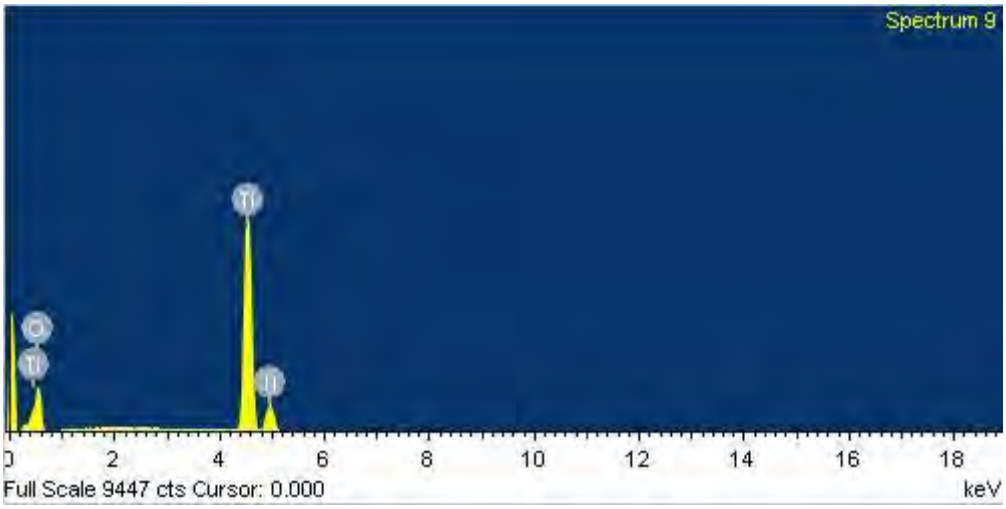

Figure 5. 8. *EDX spectrum showing the elemental mapping of the bare TiO_2*

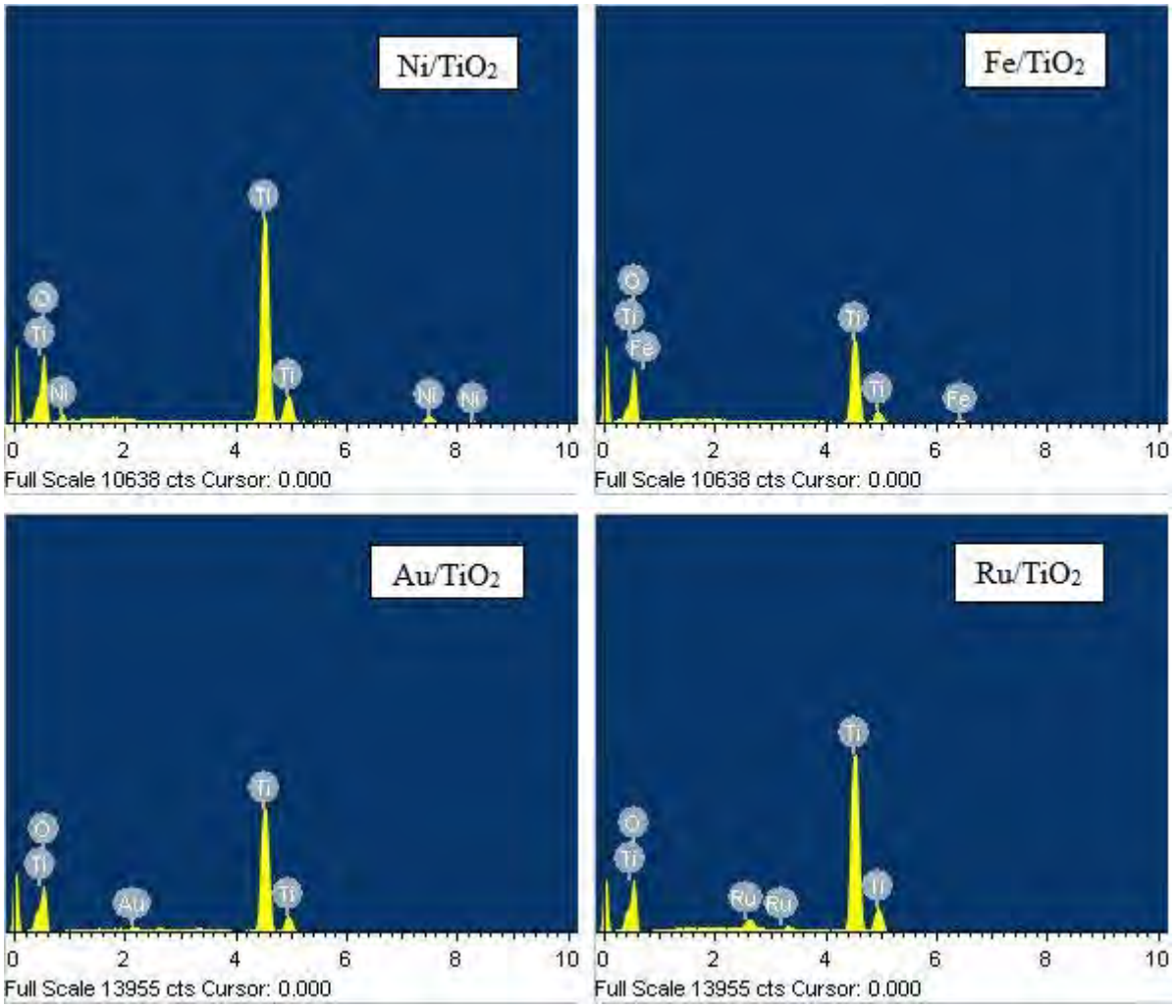

Figure 5.9: *EDX spectra showing elemental mapping of the catalysts; Ni/TiO_2, Fe/TiO_2, Ru/TiO_2 and Au/TiO_2*

The general morphology, arrangement and particle size distribution of both the catalysts and TiO_2 support were further investigated using transmission electron microscopy (TEM).

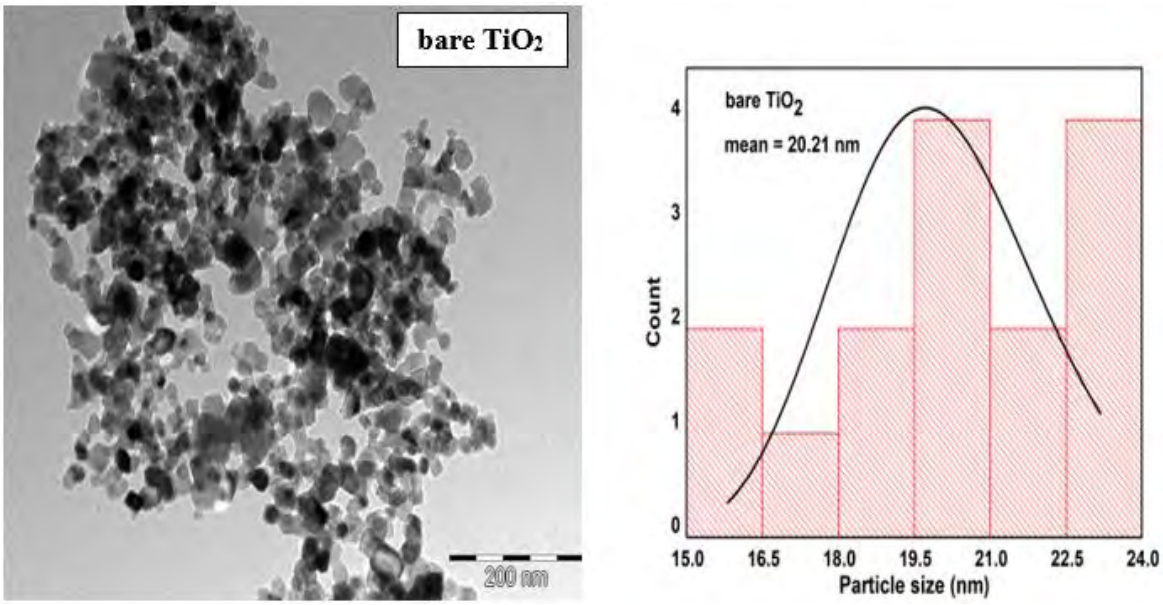

Figure 5.10: *TEM image, left, and average particle size, right, of bare TiO_2*

The TEM findings depicted in **Figure 5.10** illustrates that the untreated TiO_2 exhibits a morphology typified by predominantly aggregated spherical particles exhibiting a non-uniform size distribution. The particles are at a nanoscale, with an observed average grain size of ~20 nm. Interestingly, these findings remain consistent across the supported metal variants, as evidenced by their respective TEM images and particle size distributions, as illustrated in **Figure 5.11** and **Figure 5.12**. Remarkably, addition of the transition metals onto the support did not yield any significant impact on the average particle size, as indicated by the uniformity observed across all catalyst samples. This is in contrast to our expectation of increased particle size as a function of increasing calcination temperature. This is due to the fact that increased temperature leads to a decrease in porosity of the particles which causes it to coalesce through grain boundry diffusion.[83] [84] Nonetheless, this result seems favourable, since a particle size increase is typically associated with a decrease in surface area, which is undesireable.

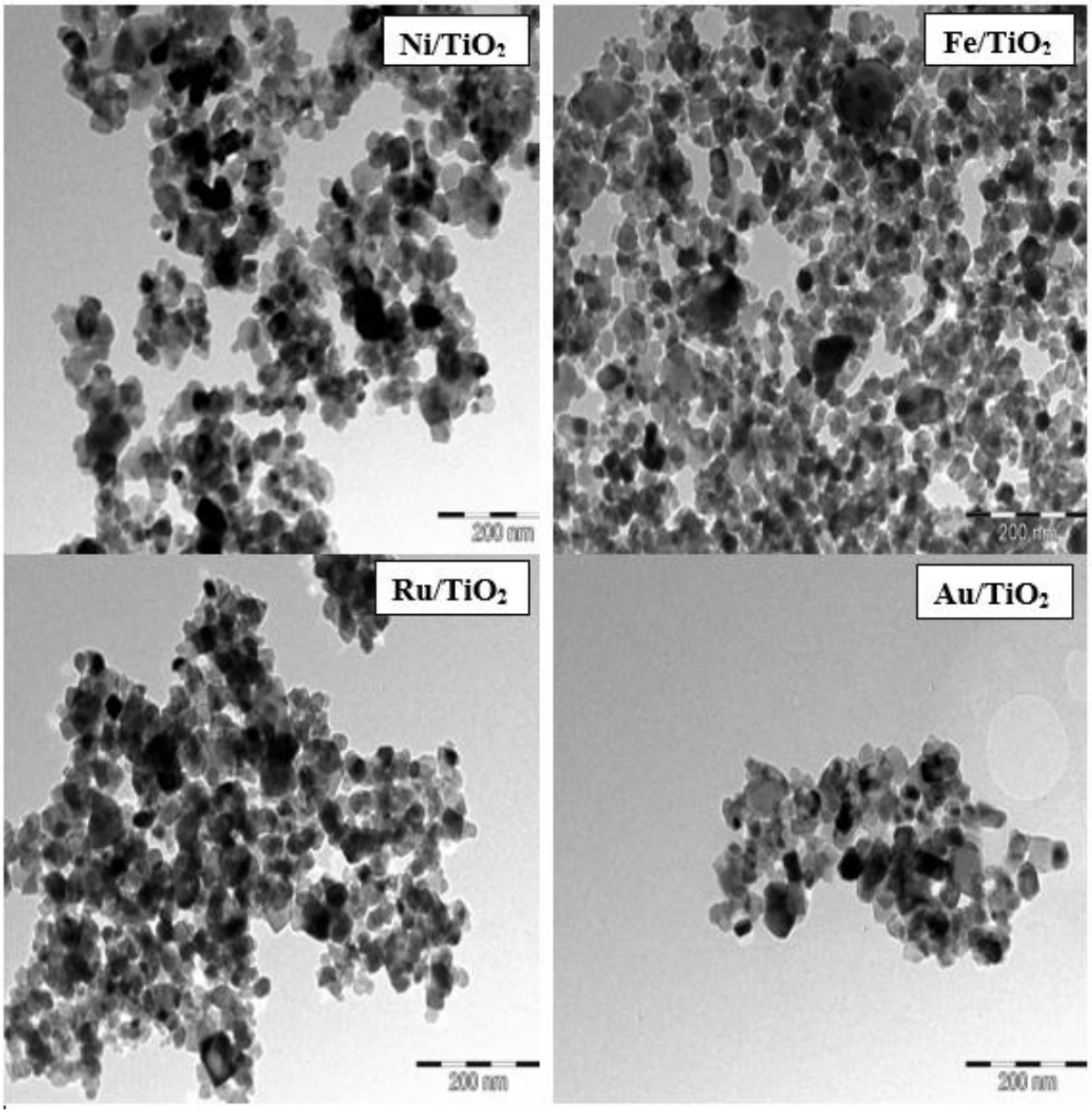

Figure 5.11: *TEM images of the produced catalysts showing particle morphology and extent of agglomeration*

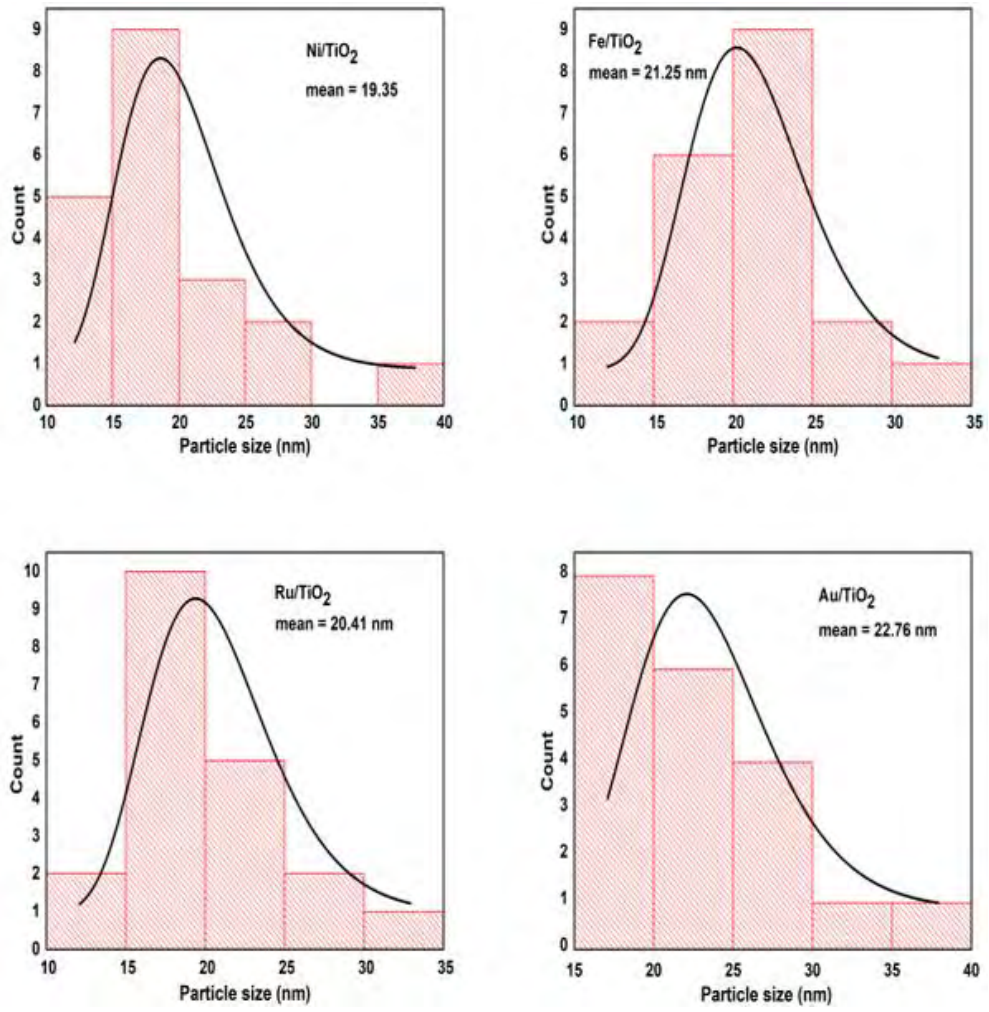

Figure 5.12: *TEM average particle size of catalysts; Ni/TiO_2, Fe/TiO_2, Ru/TiO_2 and Au/TiO_2*

The surface area, pore size and pore volume of each catalyst was determined using BET analyses as outlined in **Table 5.1**.

Table 5.1: *Surface properties of the prepared catalysts determined from BET analysis*

Catalyst	**Pore size (BJH), nm**	**Surface Area, (S_{BET}) m^2/g**	**Pore volume (BJH), cm^3/g**
TiO_2	28	41.15	0.3298
Fe/ TiO_2	8.4	126.8	0.3836
Ni/ TiO_2	33.52	36.92	0.2830
Ru/ TiO_2	58.90	14.10	0.20
Au/ TiO_2	6.90	208	0.5034

From **Table 5.1**, it is evident that there is a decrease in both surface area and pore volume upon the addition of nickel and ruthenium; while Au/TiO_2 demonstrates the largest surface area. These effects could indicate the coarsening of the particles after calcination, although further investigation into the exact nature of this effect is required.

5.1.2. Catalytic activity in the synthesis of cyclohexanecarboxylic acid

After preparing and characterizing all catalysts, we tested each in our attempt to synthesize cyclohexanecarboxylic acid from cyclohexene. This reaction involved reacting cyclohexene (40 mmol), H_2O (40 mmol) and CO_2 in the presence of each catalyst (25 mg) at 11 atm and 150 ºC. Aliquots of the products were removed from the reaction mixture at regular time intervals and analyzed *via* GC-MS.

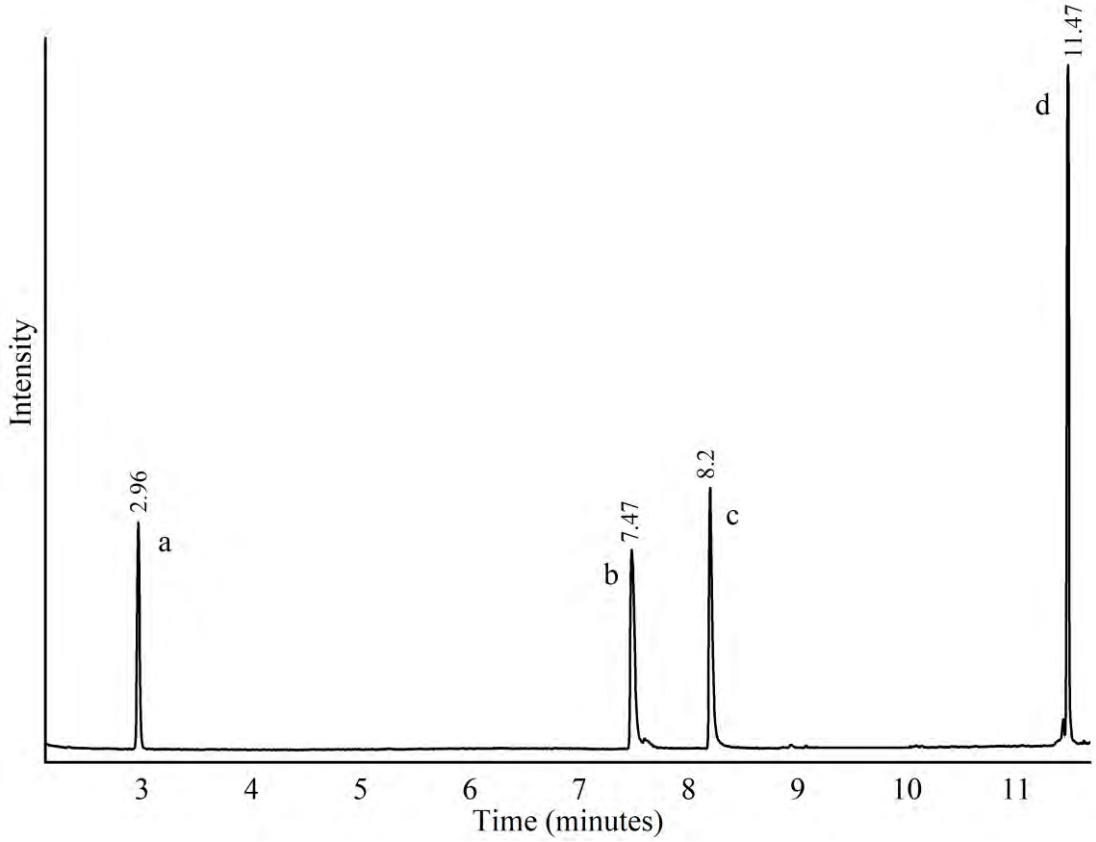

Figure 5.13. *Chromatographic profile of the products obtained in the synthesis of cyclohexanecarboxylic acid in the presence of Fe/TiO_2 catalyst after 48 hours (11 atm; 150 ^{O}C). The peaks labelled a-d are listed in* ***Table 5.2****.*

Figure 5.13 displays the chromatogramic profile obtained from the synthesis of cyclohexanecarboxylic acid from cyclohexene and CO_2 using Fe/TiO_2 as a catalyst; which was obtained after 48 hours. The chromatogram shows that several products formed during the

reaction, which was identified from the analysis of the m/Z fragmentation patterns (Figure A1-A4) in combination with NIST library comparison, **Table 5.3** Similar products were obtained using the Ni/TiO_2 and Au/TiO_2 catalytic systems, although the extent of conversion naturally differed, **Figure 5.14**. Slight differences in retention times occurred with Au/TiO_2, which is attributed to minor adjustment of instrument method.

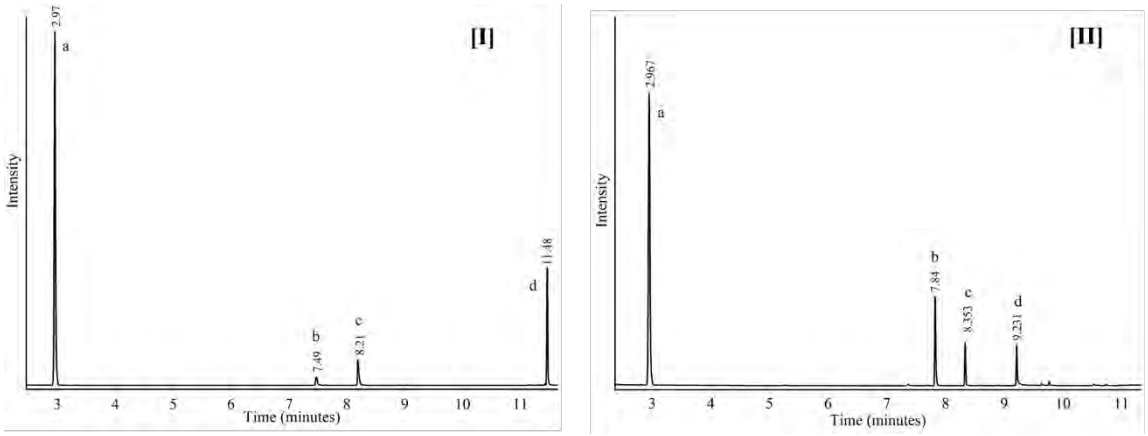

Figure 5.14: *Chromatographic profiles of the products for the synthesis of cyclohexanecarboxylic acid from cyclohexene, accelerated by* ***[I]*** *Ni/TiO_2 catalyst and* ***[II]*** *Au/TiO_2 catalyst. Pressure = 11 atm; Temperature = 150ºC; time = 48 hrs*

Table 5.4: *The list of compounds identified and labelled in the chromatograms, Figures 5.13 & 5.14, with corresponding % conversion for each catalyst*

Retention time(minutes)	Compound	Molar mass (g/mol)	% Conversion		
			Au/TiO_2	Fe/TiO_2	Ni/TiO_2
2.96 (a)	cyclohexene	82.14	63	16	69
7.47 (b)	cyclohexanone	98.15	19	14	1.5
8.2 (c)	cyclohexenone	96.13	10	19	6
11.47 (d)	cyclohexane-diol	116.2	8.7	50	23

The products obtained using the Ru/TiO_2 catalyst for the synthesis of cyclohexanecarboxylic acid were unexpectedly different to that demonstrated thus far, **Figure 5.15**. Analysis of the resulting chromatograms revealed two peaks at $t_r = 2.757$ min and $t_r = 2.963$ min. These peaks do not show pure Gaussian distribution profiles, suggesting a more complex sample matrix,

although this would require exhaustive deconvolution analyses. Nonetheless, a comparison of the fragmentation patterns with the NIST library reveals that compound (*a*) is cyclohexane ($t_r = 2.757$ min) and compound (*b*) is unreacted cyclohexene ($t_r = 2.963$). This implies that using Ru/TiO_2 as a catalyst leads to the formation of hydrogenated products rather than carboxylated products.

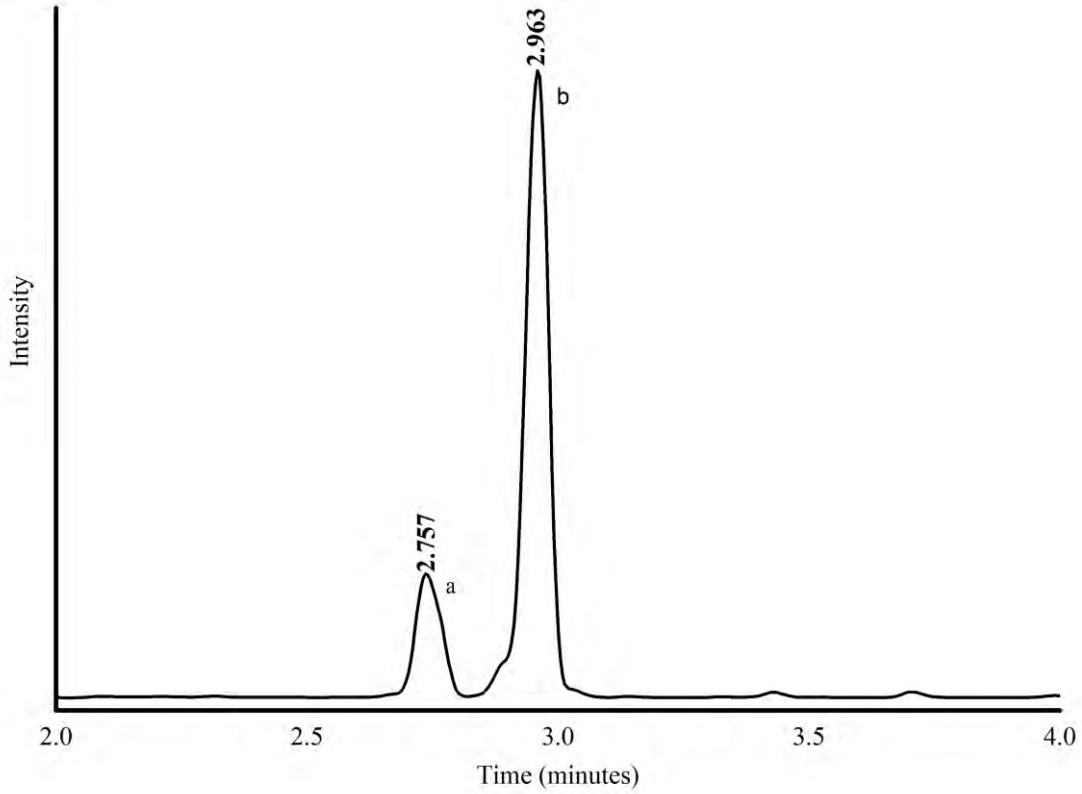

Figure 5.15*: Chromatographic profile of the products obtained using the Ru/TiO_2 catalyst, indicating hydrogenation rather than the anticipated carboxylation products.*

In an attempt to provide energetically favourable conditions for the caboxylation of cyclohexene, the reaction temperature was increased to 200 ºC. This increase in temperature did not affect the reaction products obtained from the reaction. Once the reactions were completed, the catalysts were isolated and dried overnight at 60 ºC. All the recovered catalysts were grey in colour as illustrated in **Figure 5.16**. These solids were once again analyzed using EDX and solid-state UV-Vis spectrophotometry.

Figure 5.16: *Image showing the colour change that took place on the catalyst during the reaction; Ni/TiO_2 before (left) and after (after) reaction at 200 ℃ as an example.*

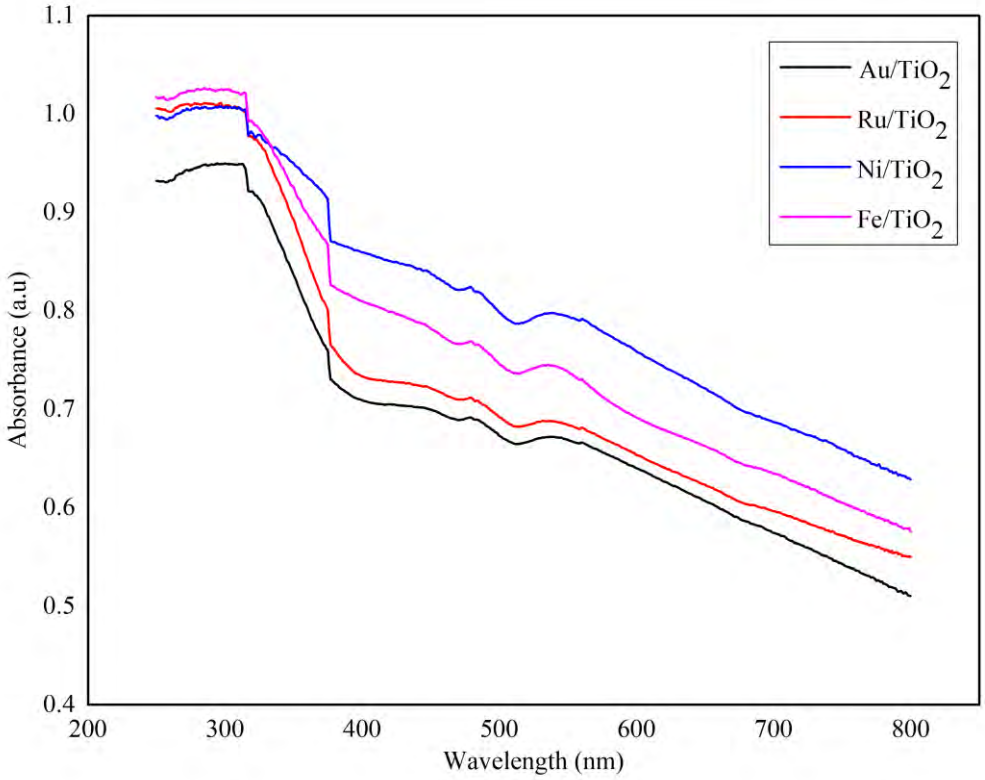

Figure 5.17: *UV-Vis spectra of the catalysts after the reaction between cyclohexene (40 mmol), water (40 mmol) and CO_2 (11 atm) after 48 hours at 200 ^{O}C*

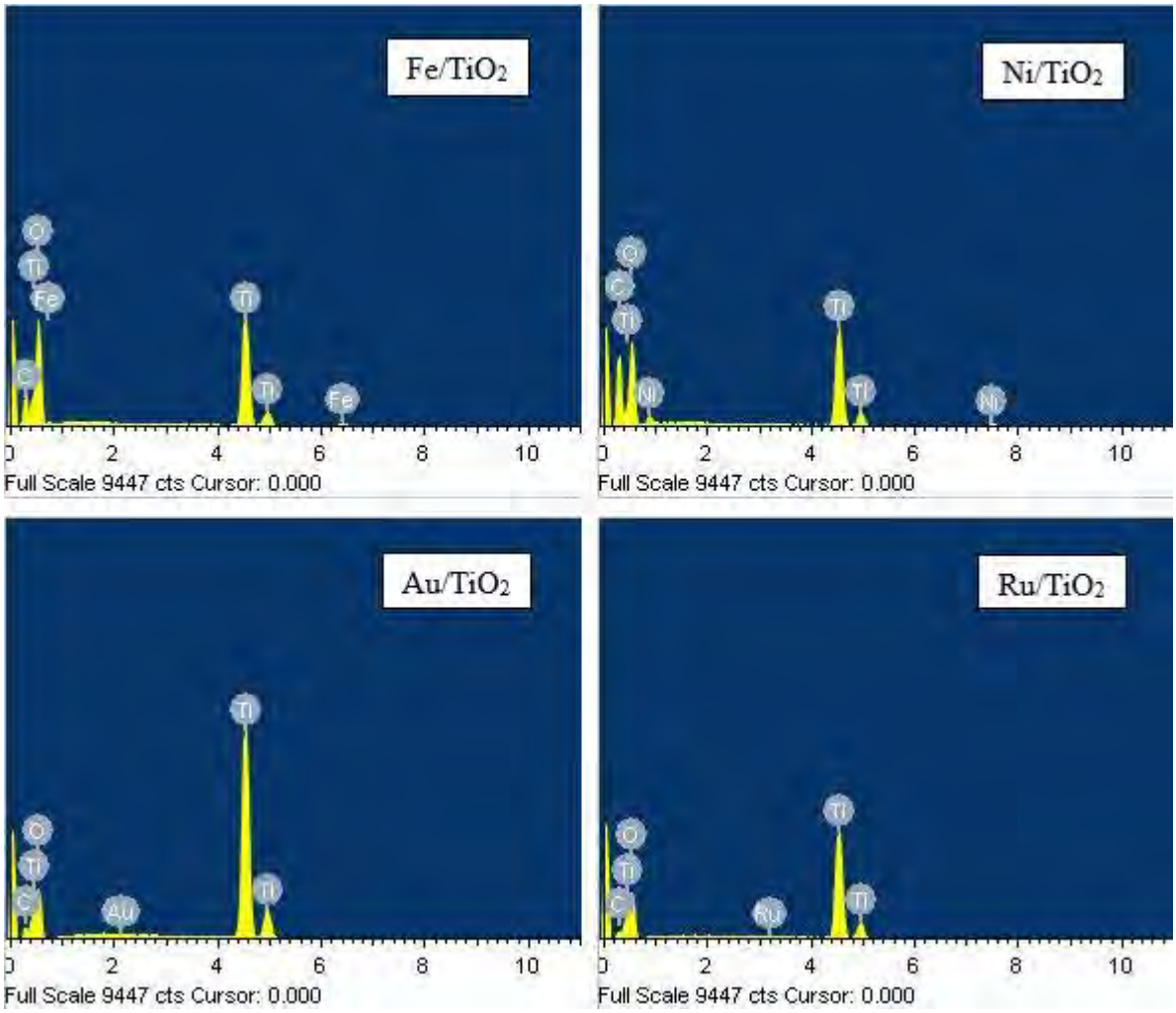

Figure 5.18: *EDX spectra showing elemental mapping of the catalysts; Ni/TiO_2, Fe/TiO_2, Ru/TiO_2 and Au/TiO_2 after the reaction at 200 ℃ to determine their elemental composition*

The EDX spectra of the catalysts after reaction shows the presence of an additional carbon peak (**Figure 5.18**), which was absent prior to perfoming the synthesis. The additional peak can be ascribed to carbon deposition on the catalysts, leading to catalyst poisoning. The source of the carbon deposited onto the catalyst could be from the olefin or the CO_2. In order to verify the carbon source, we repeated the experiment under inert conditions in the absence of CO_2. Physical inspection of the catalysts after this set of reactions revealed the same colour change as previously noted, albeit to a lesser extent. However, it was interesting to note that performing the reaction in the absence of olefin (while introducing CO_2 into the system), no colour change was observed – indicating that the decomposition of the olefin was responsible for poisoning the catalyst. Subsequent reactions were therefore performed at temperatures below 200 ºC in order to avoid olefin decomposition, and thus catalyst poisoning.

N-formylation of Amines with CO_2 [1]

The results above show us that no CO_2 has taken part in the reactions, regardless of this our interests was still to use CO_2 as a C1 source under mild conditions, therefore a slightly different approach was taken. A formylation reaction of a myriad amines with CO_2 and Hantzsch 1,4-dihydropyridine (a reductant) in the presence of Fe/TiO_2 was carried out. Interesting results were obtained and this work is in the process of being published.

The synthesis of the formylated product **A1** was chosen as our model reaction by employing *p*-toluidine (**1a, 4 mmol**), CO_2 (2 eq. **1b**), 1,4-dihydropyridine (**DHP,** 1 eq, **1c**), and Fe/TiO_2 (catalyst, 0.04 g, **1d**) in a planetary ball mill under neat (solventless), mechanochemical activation. Details of the conditions are given below according to the instrument makeup, but briefly, a milling speed of 500 rpm was applied for 60 minutes halting for 10 minutes every 30 minutes with 6 milling balls (4 mm size). (4 mm size, mass 0.52g). A second parallel jar was also filled with the same mixture under the same conditions to balance the mill and provide a replicate. The two reaction vessels were tightly closed to prevent the escape of CO_2. The Fe/TiO_2 acted as both a catalyst and a grinding auxiliary, facilitating energy transfer. This was especially important where the reagents were liquid (e.g. liquid amines); otherwise, too much liquid was ineffective in grinding. Following column chromatography purification, the expected formylated product **A1** was obtained in a 33% yield (**Scheme 5.1**).

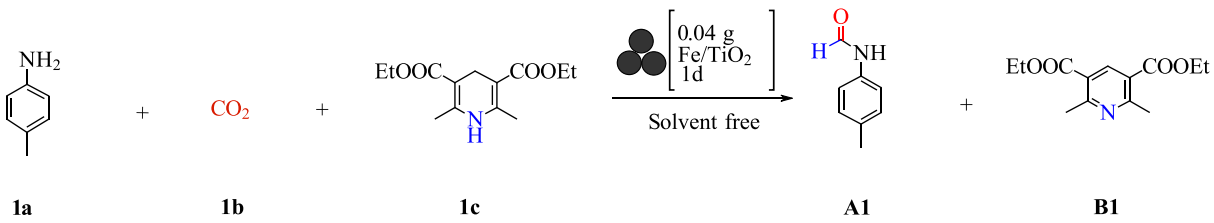

Scheme 5.1: *N-formylation of toluidine (4 mmol) using CO_2 (2 eq.) and 1,4-dihydropyridine (1 eq) in the presence of Fe/TiO_2 (40 mg) under mechanochemical conditions at a milling speed of 500 rpm with 6 milling balls (0.52 g) each for 60 minutes*

After that, the effect of various parameters, such as number of balls, revolution per minute/speed (rpm), and milling times on the model reaction, were explored. According to

[1] *This part is partially based on the publication: Sekaleli, B. T.; Salami, S. A.; Geswindt, T. E.; Smith, V.J; Krause, R. W. M. Mechanochemically Assisted N-Formylation of Amines with Carbon Dioxide and Hantzsch 1,4-dihydropyridine as the reductant Catalyzed by Fe supported over TiO2. *RSC mechanochemistry* (2024), *Manuscript prepared for publication (2024)*

reports in the literature, these parameters directly impact the active surface area and total mass, two crucial factors for the transmission of energy and the rise in internal temperature and pressure of the reaction.[85] Even though the reaction temperature rises during milling, as a result of friction and heat dissipation, planetary ball milling does not allow for the direct temperature control.[86] As a result, when the trials were carried out with more mill balls (4-10), the yields for **A1** increased from 27% to 48% (**Table 5.5**, **entries 1-4).** The findings demonstrated that ball mass significantly affects yields. Similarly, speed (rpm) has an effect on the yield, with the best yield (62%) for **A1** recorded at 800 rpm within 60 minutes (**Table 5.5, entry 5**). Finally, we investigated the effect of milling times, and as expected, this also improves the yield, but not as dramatically, only improving from 62% at 60 minutes to 74% after three hours. (**Table 5.5, entries 5-10).** The maximum yield (74%) of **A1** was recorded in 150 minutes at 800 rpm with ten (10) milling balls that had a diameter of 5 mm (**Table 5.5, entry 9)**. After this, zirconia jars and balls (ZJ diameter 6.4 mm, weight 0.384 g)) were used as a grinding vessel/material instead of stainless steel. Despite the modest yields (72%), the result indicated that the composition of the mechanochemical materials does not appear to have an impact on the reaction yield (**Table 5.5, entry 11)**.

Table 5.5: *Effect of technical parameters on the mechanochemically assisted N-formylation reaction*

Entry	Catalyst loading	Speed/rpm	Milling ball number	Time/min	Yield%	Material
1	0.04	500	4	60	27	Steel
2	0.04	500	6	60	33	Steel
3	0.04	500	8	60	48	Steel
4	0.04	500	10	60	48	Steel
5	0.04	800	10	60	62	Steel
6	0.04	850	10	60	59	Steel
7	0.04	800	10	90	65	Steel
8	0.04	800	10	120	69	Steel
9	0.04	800	10	150	74	Steel
10	0.04	800	10	180	74	Steel
11	0.04	750	10	150	72	Zirconia

Reaction conditions: Fe/TiO_2 0.04 g, 4 mmol of p-toluidine (0.43 g), CO_2 2eq. (0.86 g), DHP 1eq. 0.43 g), NB. Reaction was carried out with ten balls (diameter: 5 mm, weight 0.52 g) for 150 minutes.

We next investigated the *N*-formylation processes in a variety of solvents such as *n*-hexane, THF, $CHCl_3$, CH_3CN, MeOH, and DMSO with the results shown in (**Figure 5.19**). The results show that the reaction performed poorly in weakly polar or non-polar solvents, while polar

solvent such as MeOH and DMSO gave better yields (**A1** was produced in 56% and 72% yields, respectively within 150 minutes). This may be due to the solubility of CO_2 in polar solvent and will be investigated further. Encouraged by these results we evaluated the effect of water and ionic liquid [EMIM]Br on the reaction. Ionic liquids (ILs) have attracted much attention for several decades due to their exceptional properties like including nonvolatility, immiscibility with nonpolar or weakly polar organic solvents, and thermal and chemical stability.[87] [88] [89] [90] ILs have been used as effective catalysts and separable solvents in recent years. It is noteworthy that the characteristics of ILs may be readily modified to various desired reactions by altering the structures of cations and anions.[91] ILs with rationally designed structural components, such as amino acid, azolate, phenolate, pyridine, etc., are effective catalysts in CO_2 capturing and conversion into valuable products or chemicals.[92]

To our delight, the ionic liquid significantly increased the product yield (**Figure 5.19**), while water had the opposite effect (27%), despite being a polar solvent. This is likely due to solubility difficulties, although we have recently started to examine the use of an additional solid support.

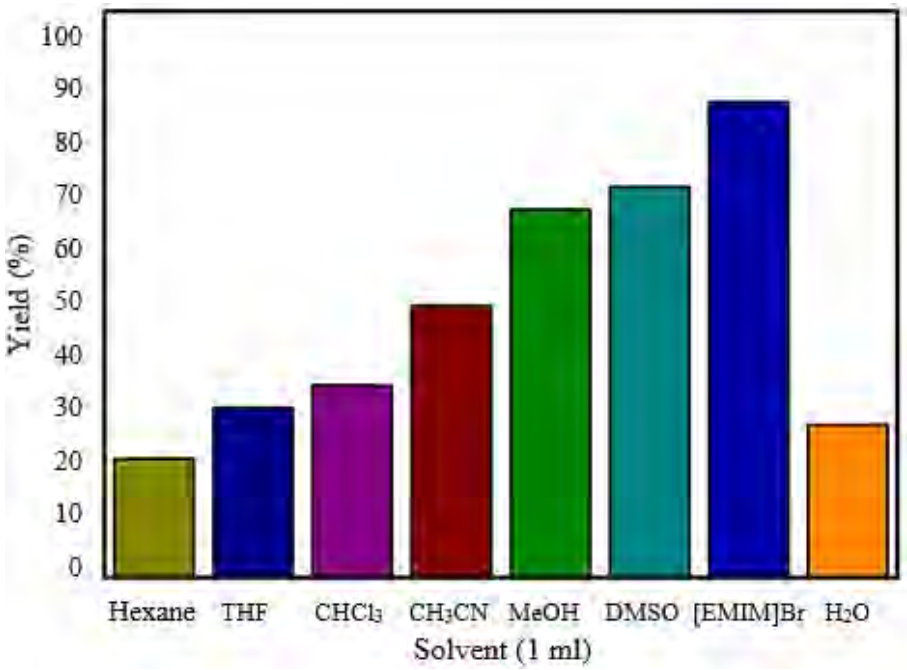

Figure 5.19: *Solvent optimization of the model reaction by varying the type of solvent used while keeping the other parameters constant*

While we attempted to use a range of supported metal catalysts (data not presented here), including Ru, Au, Zn, and Ni, it was the Fe/TiO_2 that demonstrated excellent catalytic activity

for the *N*-formylation reaction, achieving complete conversion of *p*-toluidine in good yield and purity. It should be noted that the same catalyst performed unsatisfactorily in the absence of [EMIM]Br, indicating that the IL was critical in increasing the activity and the yield of the reactions, and this effect deserves further attention.

It is well known that DHP is easily oxidized even in the presence of air at room temperature. On the other hand, conventional DHP reactions required an excess DHP or inert gases. As a result, the impact of the molar equivalents of CO_2/DHP on catalytic performance was examined. As seen in (**Figure 5.20**), the molar equivalent of CO_2/DHP was modified to enable the *N*-formylation of amines under best condition. The *N*-formylation reaction was significantly impacted by the CO_2/DHP ratio according to the results obtained. The reaction went quite smoothly as the molar ratio of CO_2/DHP grew up to 2/1, and good yield were attained (**Figure 5.20**). However, excess CO_2 (high molar ratio of CO_2/DHP) is unfavorable for the formation of **A1**. The result revealed that the reaction could be conducted under the best conditions (CO_2/DHP = 2/1, for 150 min at room temperature) in the presence of Fe/TiO_2 (0.04 g).

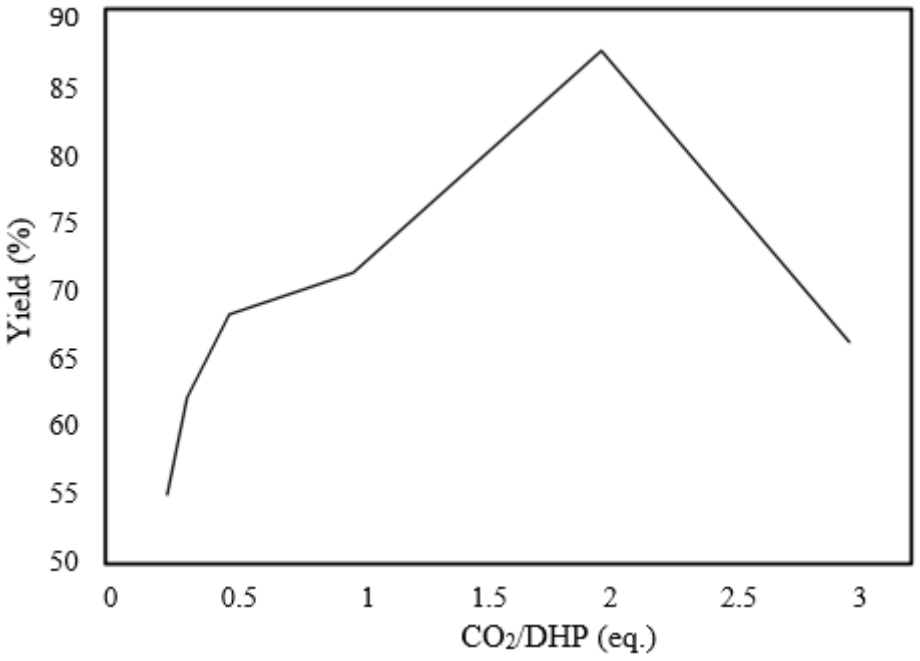

Figure 5.20: *Optimization of the molar equivalent by varying the ratio of CO_2/DHP to see how the reaction changes*

Catalytic investigations were next carried out to improve the product reaction yields by varying the quantity of the catalyst from 0.01 g to 0.1 g while keeping the other experimental parameters

constant. It is noteworthy that when the catalyst quantity was raised to 0.06 g, the conversion rate steadily improved from 87% to 96% (***Figure 5.21***). It is, however, noteworthy that in the absence of a catalyst, formylation yields of ~54% were still obtained. This could indicate there might be another catalytic species (***Figure 5.21***). In this respect, the Li group has demonstrated that certain ionic liquids can act as a formylation catalyst, which is supported by our observations of no reaction in the absence of IL and Fe/TiO_2.[94] The optimal catalyst quantity for a successful formylation for these present studies was determined to be 0.06 g (***Figure 5.21***).

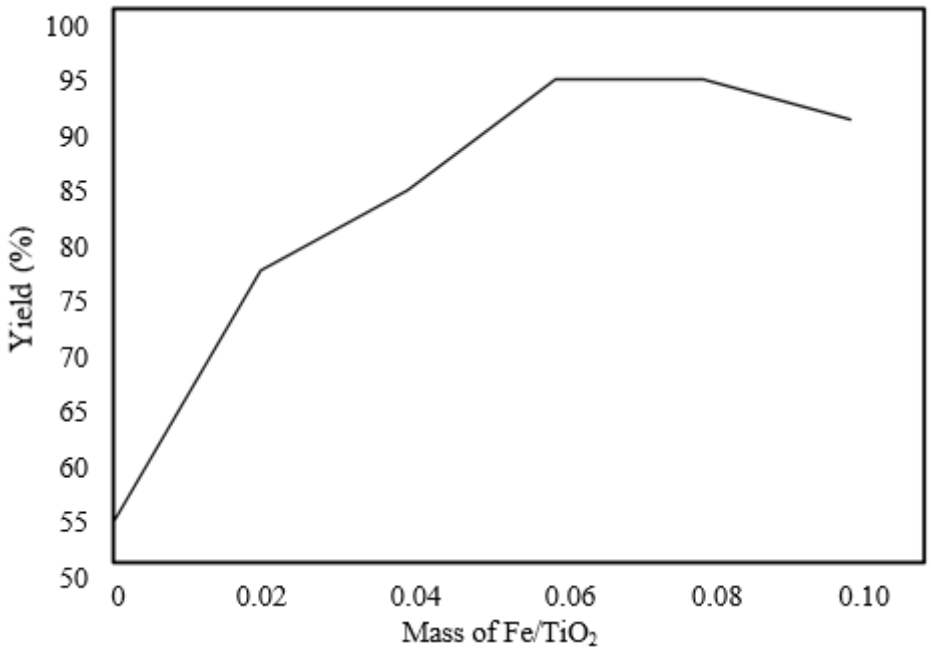

Figure 5.21: *Investigating the effect of catalyst Fe/TiO_2 on the model formylation reaction by varying the mass of catalyst used with each reaction while keeping the other parameters the same*

Following the above optimized reaction conditions, we set out to assess the applicability of this unique technique for the construction of versatile formamides. The scope of the formylation was evaluated with various amines (primary, secondary, aromatic, aliphatic) and we were excited to discover that the functional group and substitution pattern on the phenyl ring of primary aromatic amines had only a little impact on the result of the transformation. When primary or secondary aliphatic amines with various substituents were subjected to the *N*-formylation reaction, the corresponding formamides **A4, A16, A24,** and **A29** were produced in near quantitative yields (86-95%) (

***Scheme 5.2*)**.

The formylation of the sterically hindered amines, such as **A26** also proceeded smoothly in excellent yield (86%) and high purity. This reaction was also active for an amine containing

anthraquinone **A19**, and the product was obtained in 80% yield. Similarly, unsaturated aliphatic and cyclic amines, such as propargylamine and cyclohexylamine were well tolerated (**A4/A16** in yields of 83% and 93%, respectively). This formylation was also suitable for weakly nucleophilic aromatic amines. As an example, the reaction with aniline afforded **A17** in a 92% yield. Methyl groups **A1, A2**, and electron-withdrawing (**A3** = R-COOR, A5 = NO_2, A6 = COOH, A8 = F, A9 to A13 = Cl, I, Br) substituents on the aromatic ring were well tolerated, giving excellent yields above 83%. Particularly noteworthy was the good yield (95%) of the *N*-formylation product **A28** for the reaction involving *N*-methylaniline. Under the optimized conditions, heterocyclic amines, including furan, thiazole, pyridine, and imidazole moieties, were also compatible with the reaction and generated **A20-A23, A25-A27** in 77-95% yield. Interestingly, the reaction involving diamines such as *o*-phenylenediamine, and 1,8-diaminonaphthalein afforded only the di-formylated products (**A15, A18)** in good yields (80-84%).

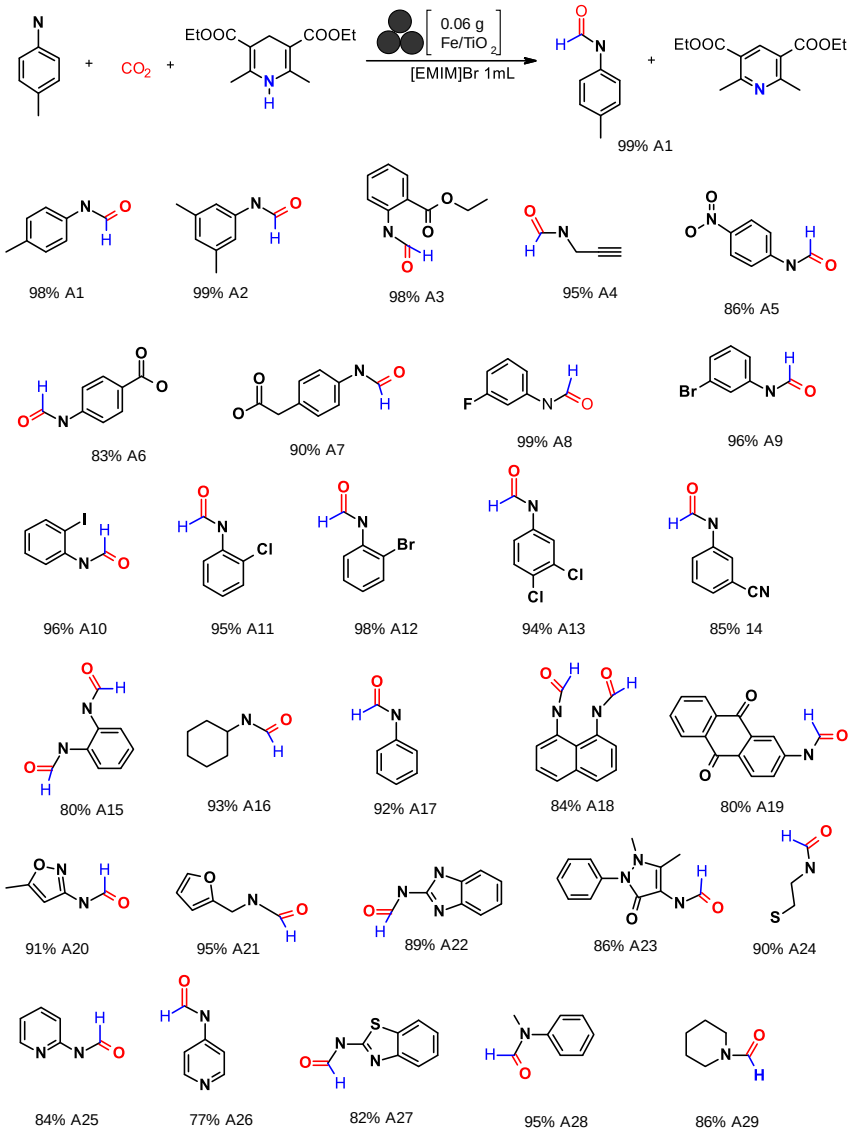

Scheme 5.2: *Products obtained with N-Formylation of amines catalyzed by Fe/TiO₂ using CO₂ and DHP in the presence of IL under mechanochemical condition. The pure product was obtained following column chromatographic purification and characterized using FTIR, NMR.*

Despite the low cost of the catalyst, we briefly investigated its reusability (**Figure 5.22**). It was discovered that the catalyst could be recycled at least five times with a good yield of formamide without any significant loss in catalytic activity. In each instance, approximately >90% of the Fe/TiO_2 was simply recovered from the reaction mixture by washing with ethyl acetate. The small loss of activity (~2% per repeat), correlates well with the small loss of catalyst mass during the washing and re-weighing manipulations, mostly due to some very fine particles produced during ball milling. However, in order to verify if there was any physical change in the catalyst surface, some pre- and post-reaction characterization was undertaken.

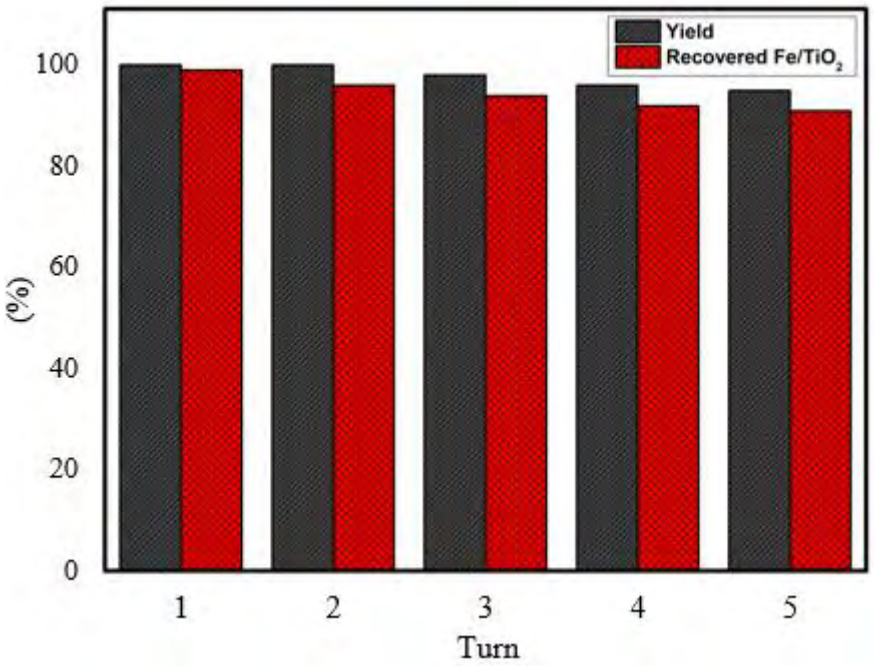

Figure 5.22: *Efficiency of the recycled catalyst in the N-formylation of ethyl anthranilate under same reaction conditions*

The catalyst before and after reaction was then characterized using PXRD, ATR-FT-IR and DSC.

The XRD patterns of the Fe/TiO_2 catalyst before reaction exhibit a number of diffraction peaks which are observed at 25.5°, 27.7°, 36.2°, 37°, 37.9°, 38.7°, 41.5°, 48.2°, 54°, 55.3° and 56.7° (**Figure 5.23** and **Figure 5.24**). After the catalyst was used in the reaction, the diffraction pattern almost unaltered, demonstrating the sturdiness of the catalyst even under harsh mechanical force induced by the ball milling. However, there are new peaks arising from the organic materials being adsorbed on the catalyst. These new peaks are seen at 10.3°, 16.3°, 19.2°, 20.5°, 29.4°, 30.1°, 30.9°, 34.1° and 40.2°. Furthermore, there's a slight shifting of the original peaks to higher diffraction angles indicating a unit cell contraction which is as a result of the repeated high impact force of the milling balls delivering shock on the structure of the catalyst.

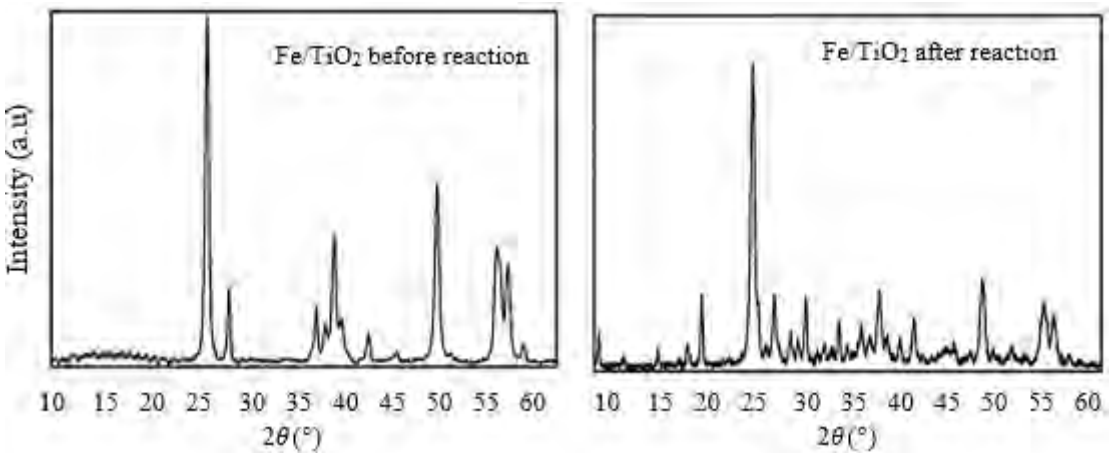

Figure 5.23: *PXRD diffractograms showing the diffraction pattern of Fe/TiO_2 before and after the formylation reactions*

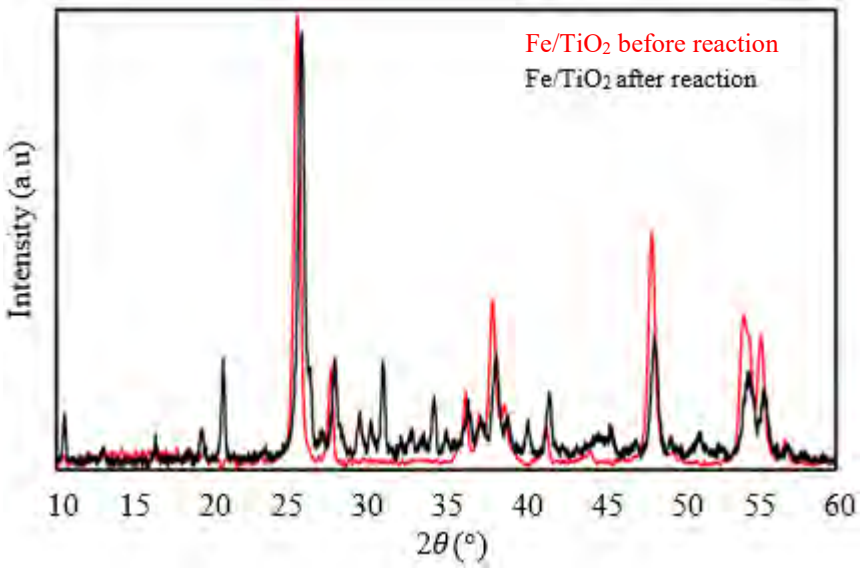

Figure 5.24: *Overlaid diffractograms of Fe/TiO_2 before and after reaction highlighting the differences.*

As seen in (**Figure 5.25)**, the chemical composition of the Fe catalyst was preserved, but it was still possible to see traces of the residual formamides and substrate molecules on the recovered catalytic system. The FT-IR spectra of the employed catalytic system revealed new peaks at 3341 cm^{-1} and 1714 to 821 cm^{-1} on the recovered Fe/TiO_2 following five recycles, which are attributed to the aromatic CH groups and aldehyde group of the residual formamide (***Figure 5.25***).

The FT-IR spectrum of the catalyst before reaction displays the (Ti-O) bending vibrations at 428 cm^{-1}, there are no other bands observed on the spectrum. The FT-IR spectrum of the catalyst after reaction on the other hand shows the (Ti-O) bending vibrations at 447 cm^{-1}.

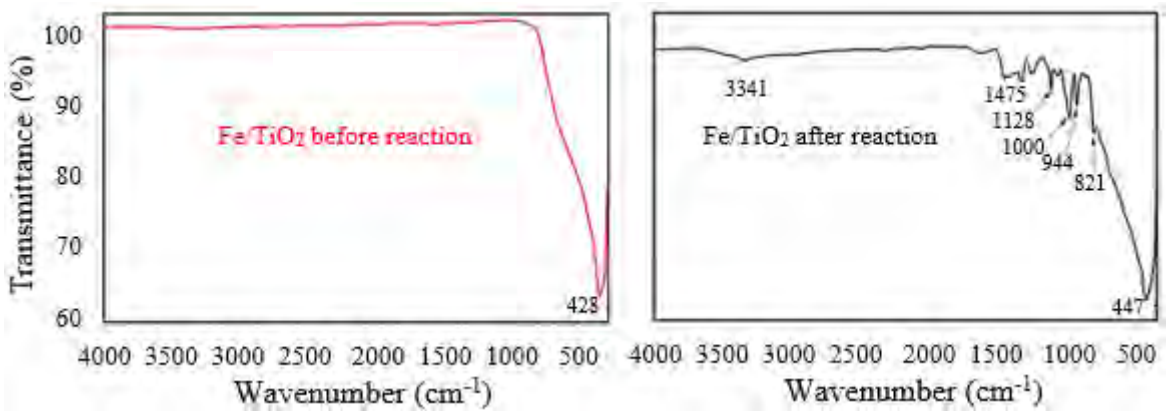

Figure 5.25: *FT-IR spectra of Fe/TiO_2 before and after the formylation reactions*

The thermograms of the catalyst before and after reaction show different events. On the thermogram of the catalyst before reaction there is no clear event seen. The thermogram of the catalyst after reaction on the other hand displays three distinct thermal events at 68 ℃, 102 ℃ and 138 ℃. These thermal events correspond to the phase change or melting of the substrates that adsorbed on to the surface of the catalyst during the mechanochemical reaction (

Figure 5.26).

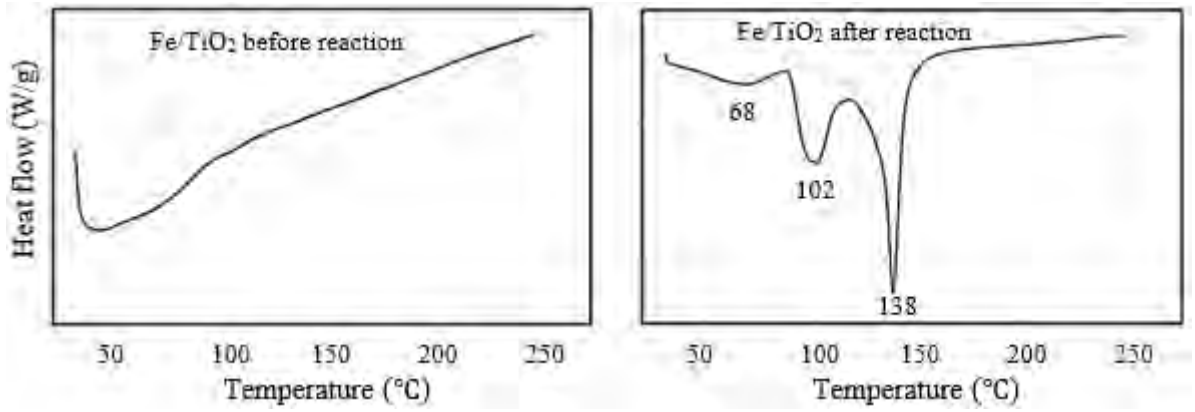

Figure 5.26: *DSC thermograms of Fe/TiO2 before and after formylation reactions*

Furthermore, the efficiency of our catalytic system was assessed by comparing the *N*-formylation of amine with CO_2 and DHP utilizing the present Fe catalyst system to the catalytic performance of other catalysts reported in the literature (**Table 5.6**). The *N*-formylation of various optimized experimental conditions was chosen as the model reaction for comparison. The findings demonstrated that our catalyst system, when compared to previously published catalysts, had a comparable yield to formamide; nevertheless, the present catalytic system offers a more promising path toward sustainability through mechanochemistry.

Table 5.6: *Comparison of efficiency of various conditions in the N-formylation of aniline using CO_2 as the carbonyl source.*

Entry	Catalyst	Reductant	Solvent	Time	Yield%	Ref.
1	DUT-5-CoH	$H_2/PhSiH_3$	THF	20 h	99	[11]
2	[PPN][$Ru(CO)_3Cl$	H_2	hexane	10 h	99	[9]
3	NGU/K-900	$PhSiH_3$	CH_3CN	6 h	99	[10]
4	Ru/PNP pincer complex	H_2	THF	16 h	99	[1]
5	ACH-AA	$PhSiH_3$	CH_3CN	6 h	99	[41]
6	Fe/TiO_2	DHP	[EMIM]Br	2.5 h	99	Present study

5.2. Homogenous catalytic approaches for the esterification of olefins

5.2.1 Synthesis of 1-Butyl-3-methylimidazolium chloride $[BMIM]^+Cl^-$

The first objective in this part was to synthesize $[BMIM]^+Cl^-$, an important additive in our reaction without which the targeted product (ester) cannot be obtained. This ionic liquid was synthesized using 1-methylimidazole and 1-chlorobutane as starting materials as illustrated in **Scheme 5.3**.

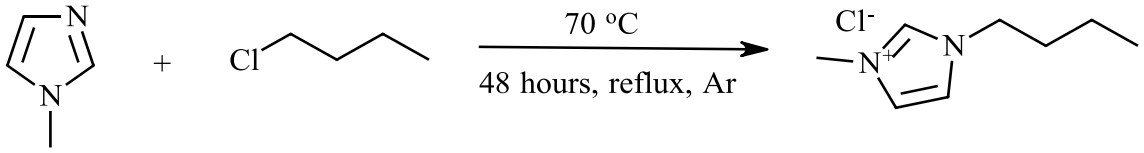

Scheme 5.3: *Synthesis of 1-butyl-3-methylimidazole from equimolar amounts of 1-methylimidazole and 1-chlorobutane at 70 ℃ for 48 hours under inert conditions*

This is a Menshutkin type of reaction that happens through S_N2 quaternization between a neutral tertiary amine, 1-methylimidazole, and a neutral alkyl halide, 1-chlorobutane. As a result, two ions of opposite charge are formed through a polar transition state, which eventually separate forming an organic salt with an organic cation and an inorganic anion.

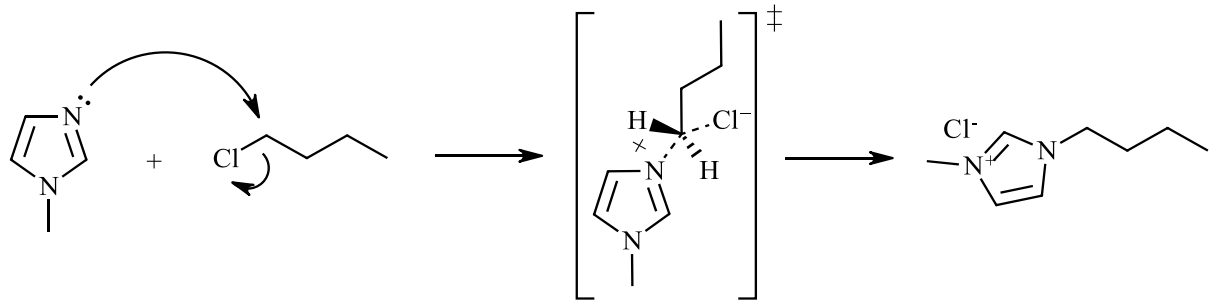

Scheme 5.4: *Illustration of the S_N2 quaternization reaction between 1-methylimidazole and 1-chlorobutane*

Once the product was isolated, it was characterized using ^{1}H NMR and ATR-FT-IR spectroscopy.

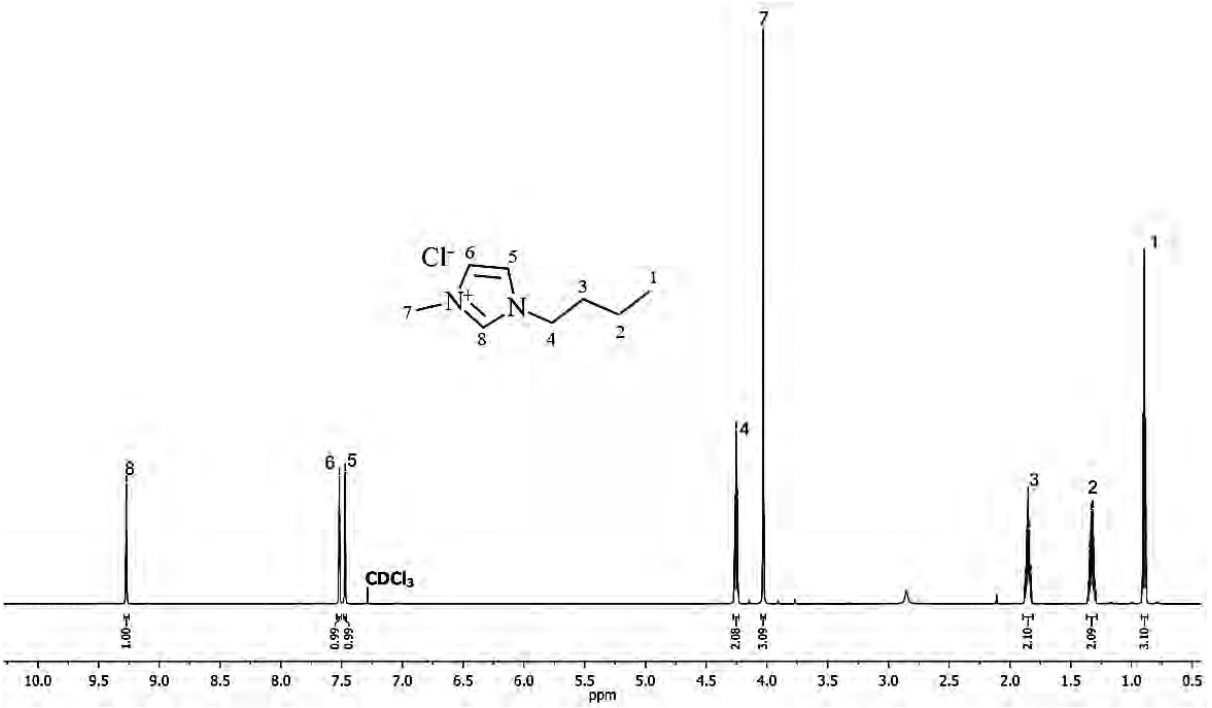

Figure 5.27: *^{1}H-NMR spectrum of [BMIM]Cl obtained after a reaction between equimolar amounts of 1-methylimidazole and 1-chlorobutane at 70 °C for 48 hours under reflux in an inert atmosphere, (600 MHz, CDCl3): δ (ppm) 9.25 (s, 1H, C2-H), 7.6 (t, 1H, C4-H), 7.44 (t, 1H, C5-H), 4.24 (t, 2H, C7-H), 4.03 (s, 3H, C6-H), 1.8 (m, 2H, C8-H), 1.27 (m, 2H, C9-H), 0.86 (t, 3H, C10-H)*

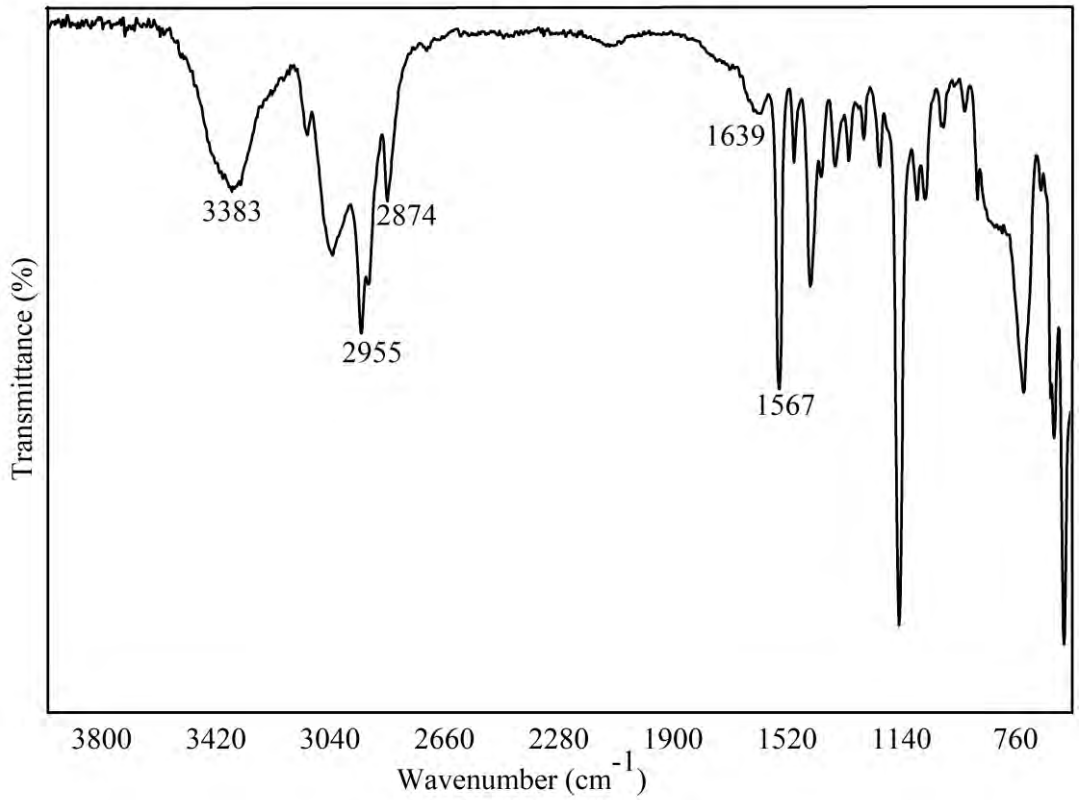

Figure 5.28: *FT-IR spectrum of [BMIM]Cl obtained after a reaction between equimolar amounts of 1-methylimidazole and 1-chlorobutane at 70 °C for 48 hours under reflux in an inert atmosphere*

As illustrated by the FT-IR spectrum in **Figure 5.28**, the quaternary amine salt formation was confirmed by the band at 3383 cm^{-1}, the bands at 2955 and 2874 cm^{-1} correspond to the asymmetric and symmetric (C-H) stretching vibrations of the methyl groups. Finally, the (C=C) and (C=N) bond stretching vibrations are represented by the bands at 1639 and 1567 cm^{-1}, respectively.

5.2.2 Synthesis of methyl cyclohexanoate from cyclohexene

The preparation of methyl cyclohexanoate was carried out using cyclohexene, methanol and CO_2 as starting reagents in the presence of $Ru_3(CO)_{12}$ as a catalyst and [BMIM]Cl as an additive. The inspiration to perform this reaction was drawn from the green chemistry perspective, where CO_2, an abundant waste material, can be reused as a C1 synthon. To delineate the progress of the reaction, a series of experiments were performed as a function of time. The reaction is presumed to occur through the mechanism outlined in **Scheme 5.5.** The resulting product was characterized *via* GC-MS in order to identify the compounds and calculate the percentage conversion as a function of time. Confirmation of the compounds

identified was done by comparison of the m/Z fragmentation pattern to that documented in the NIST library, **Figures 5.29 and 5.30.**

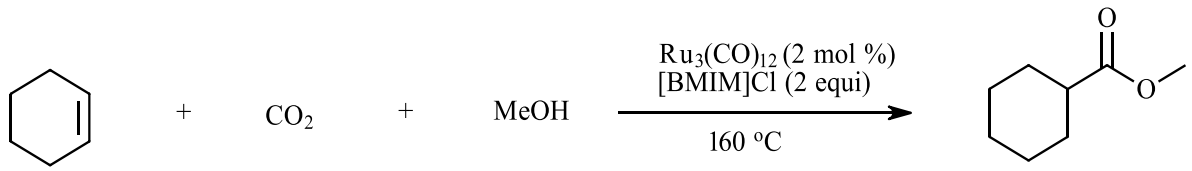

Scheme 5.5: *Synthesis of methyl cyclohexanoate from cyclohexene (9.87 mmol), CO_2 (11.578 atm), MeOH (494.3 mmol) in the presence of 2 mol % $Ru_3(CO)_{12}$ and 2 equivalents [BMIM]Cl ionic liquid at 160 ℃.*

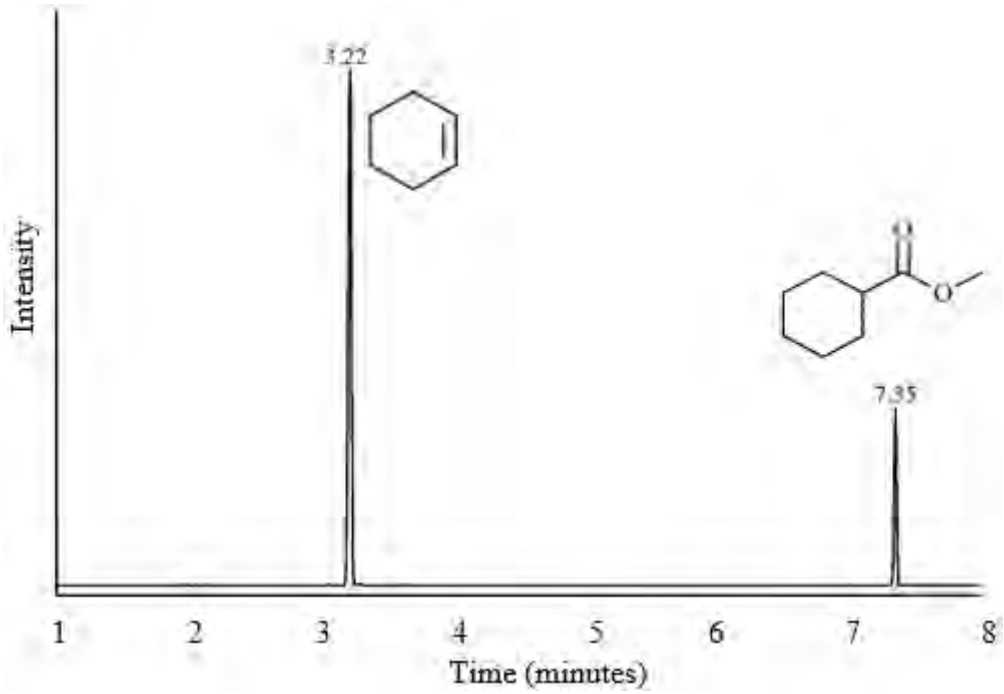

Figure 5.29: *Chromatographic profile of the reaction products after 48 hours for the reaction between cyclohexene (9.87 mmol), methanol (494.3 mmol) and CO_2 (11.578 atm) in the presence of 2 mol % $Ru_3(CO)_{12}$ and 2 equivalents [BMIM]Cl ionic liquid at 160 ℃. Retention time at; 3.22 minutes is unreacted cyclohexene; 7.35 minutes is methyl cyclohexanoate*

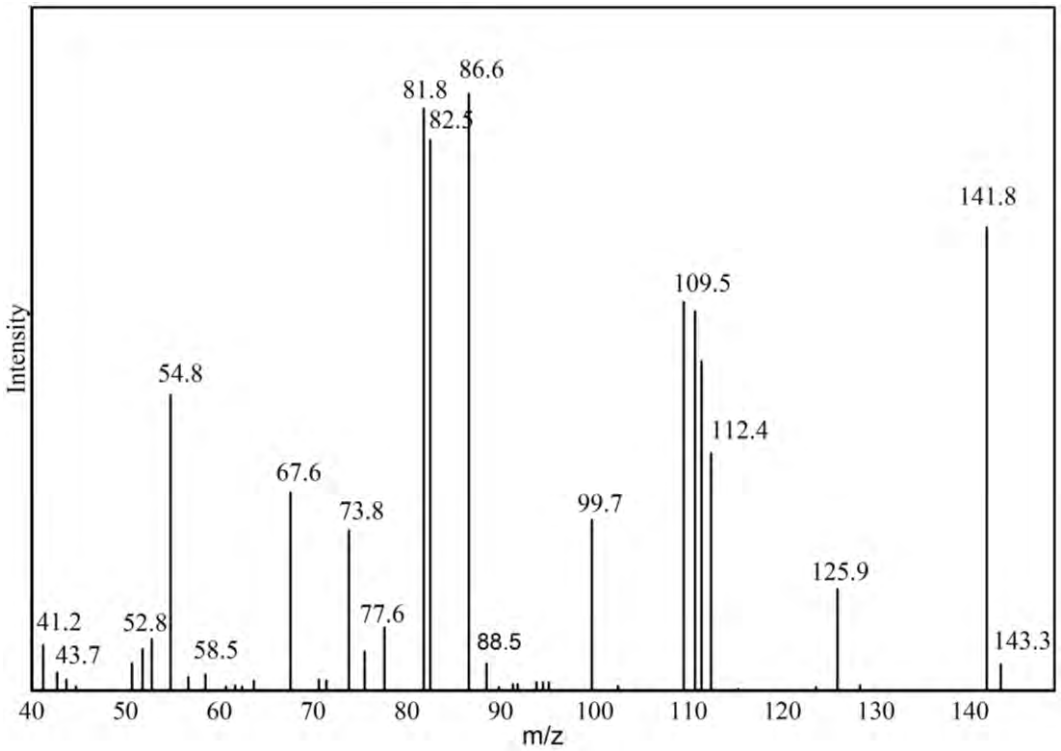

Figure 5.30: *Mass spectrum of the compound at the retention time of 3.22 minutes on the chromatogram with the mass of 141.8 g/mol, identified as methyl cyclohexanoate*

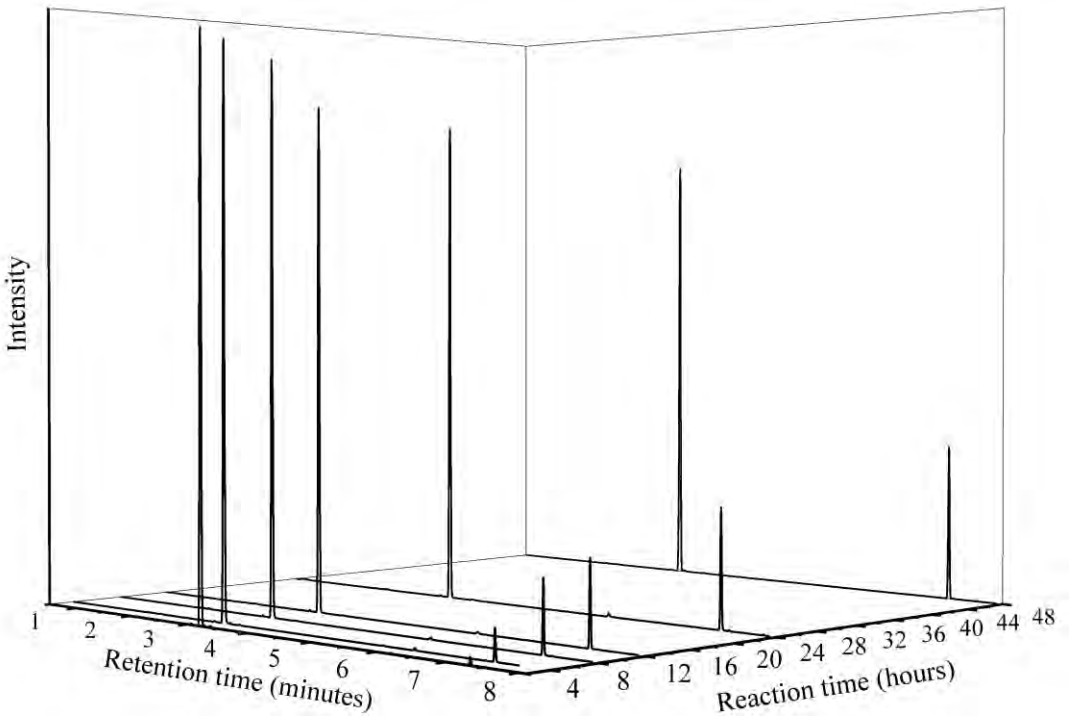

Figure 5.31: *Chromatographic traces of products obtained as a function of overall reaction time. P = 11 atm; 160 °C. Unreacted cyclohexene – tr = 3.22 min; methyl cyclohexanoate – tr = 7.35 min*

The percentage yield of the obtained ester as a function of time was calculated relative to the unreacted cyclohexene detected in the reaction mixture (**Table 5.5**), and the corresponding calibration curves are presented in the appendix.

Table 5.5: *Percentage concentration and yield of methyl cyclohexanoate determined from calibration data*

Reaction time (hours)	Peak area $\times 10^7$ (AU)	% Concentration	Product % yield
2	5,27	98,5	1,50
4	4,82	90,0	10,0
8	4,56	85,3	14,7
12	4,40	82,2	17,8
24	4,04	75,4	24,6
48	3,91	73,0	27,0

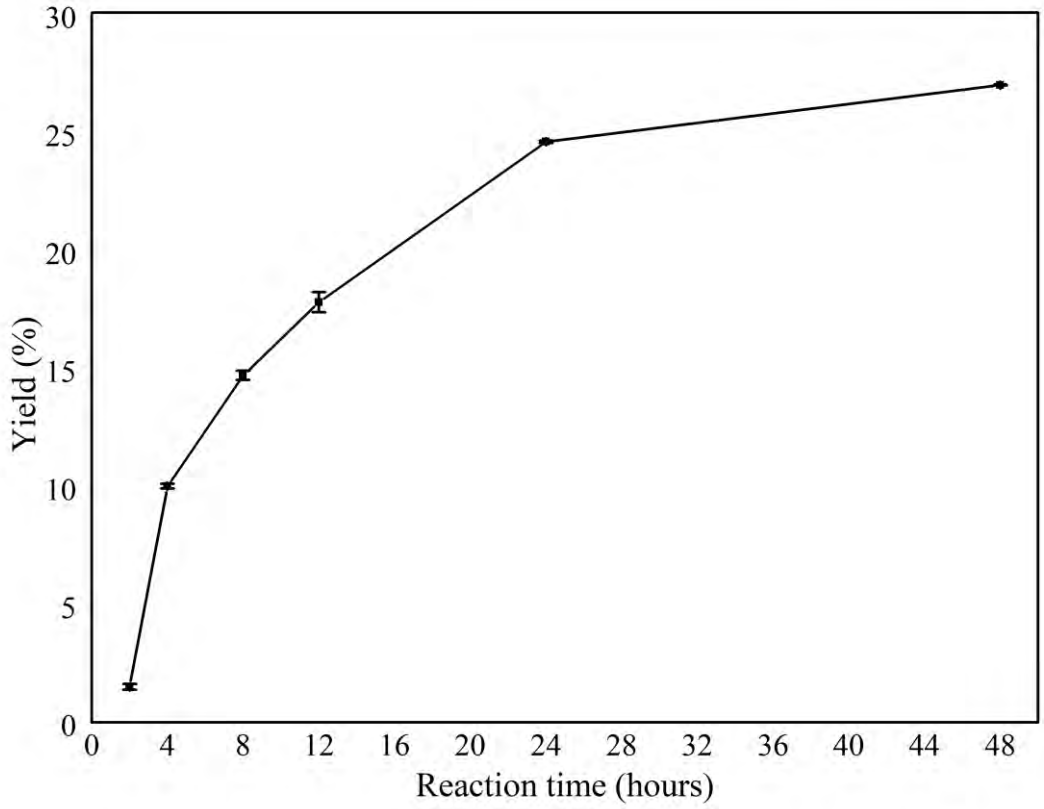

Figure 5.32: *Percentage yield of methyl cyclohexanoate as a function of reaction time. Reaction conditions: cyclohexene (9.87 mmol), methanol (494.3 mmol) and gaseous CO_2 (11.578 atm) in the presence of 2 mol % $Ru_3(CO)_{12}$ and 2 equivalents [BMIM]Cl ionic liquid at 160 °C.*

Since CO_2 is considered as a reagent, we wanted to establish if the reaction rate would be influenced if the reaction solution was saturated with CO_2. Therefore, we saturated the reaction solution with dry ice to determine any change in the rate of formation of methyl cyclohexanoate. These reactions were performed in an analogous manner as the previous reactions and time intervals, and the products analysed using GC-MS.

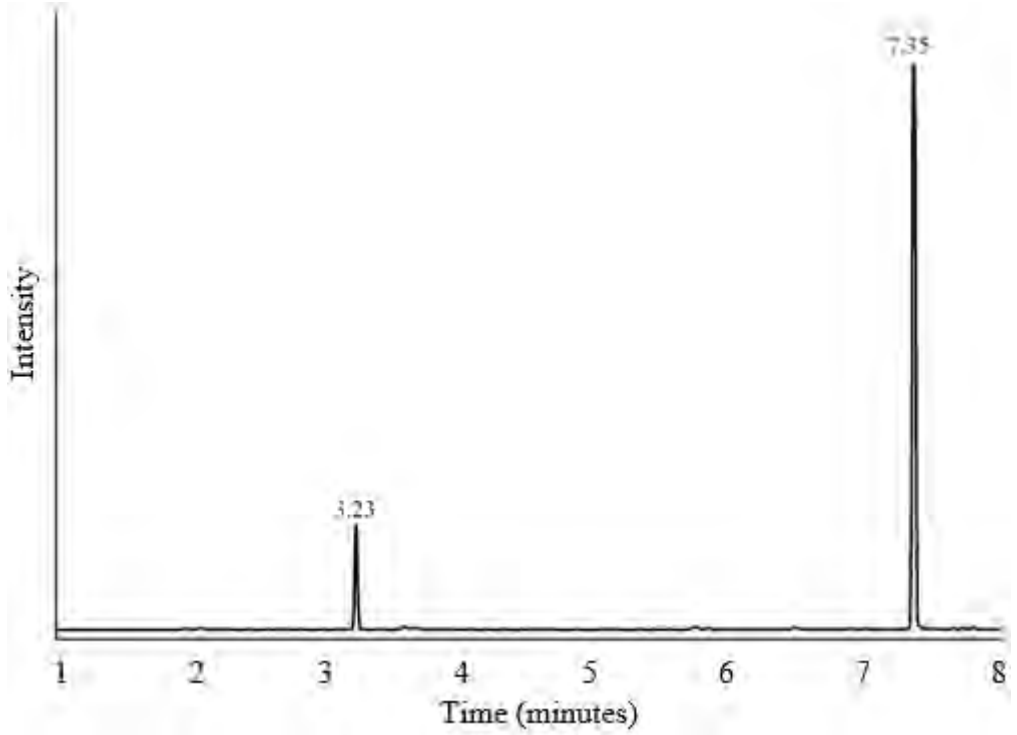

Figure 5.33: *An example of the chromatographic profile obtained after allowing the reaction to proceed for 48 hours. Reaction conditions: cyclohexene (9.87 mmol), methanol (494.3 mmol), excess solid CO_2 (≈ 20 g) at 11 atm and 160 ℃. The peak at t_r=7.35 min is methyl cyclohexanoate*

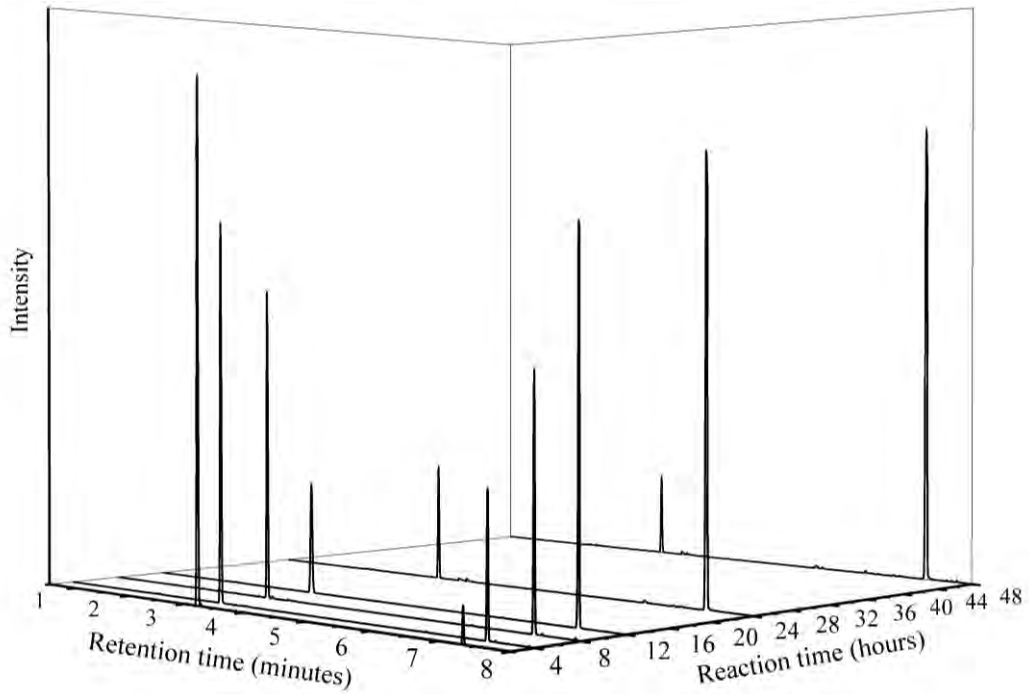

Figure 5.34: *Merged 3d total ion chromatograms of products obtained after reaction as a function of time 2, 4, 8, 12, 24 and 48 hours of reaction between cyclohexene (9.87 mmol), methanol (494.3 mmol) and excess solid CO_2 (≈ 20 g) at 160 ℃. Retention time at; 3.22 minutes is the unreacted cyclohexene; 7.35 minutes is methyl cyclohexanoate.*

By saturating the reaction solution with CO_2, we observed a dramatic increase in the rate of conversion of cyclohexene to methyl cyclohexanoate, (**Table 5.6**). This dramatic increase in methyl cyclohexanoate formation from 27 % to 87 % after 48 hr is mainly attributed to the increased dissolution of CO_2 in the solution as opposed to performing the experiment under a CO_2 atmosphere.

Table 5.6: *Results showing product yield with the addition of solid CO_2 obtained by calibration curve Percentage concentration and yield of methyl cyclohexanoate determined from calibration data*

Reaction time (hours)	Peak area $\times 10^7$ (AU)	% Residual cyclohexene	Product % yield
2	5,34	95,0	5,00
4	3,73	65,5	34,5
8	2,95	51,2	48,8
12	1,58	26,1	73,9
24	1,13	17,8	82,2
48	0,83	12,4	87,6

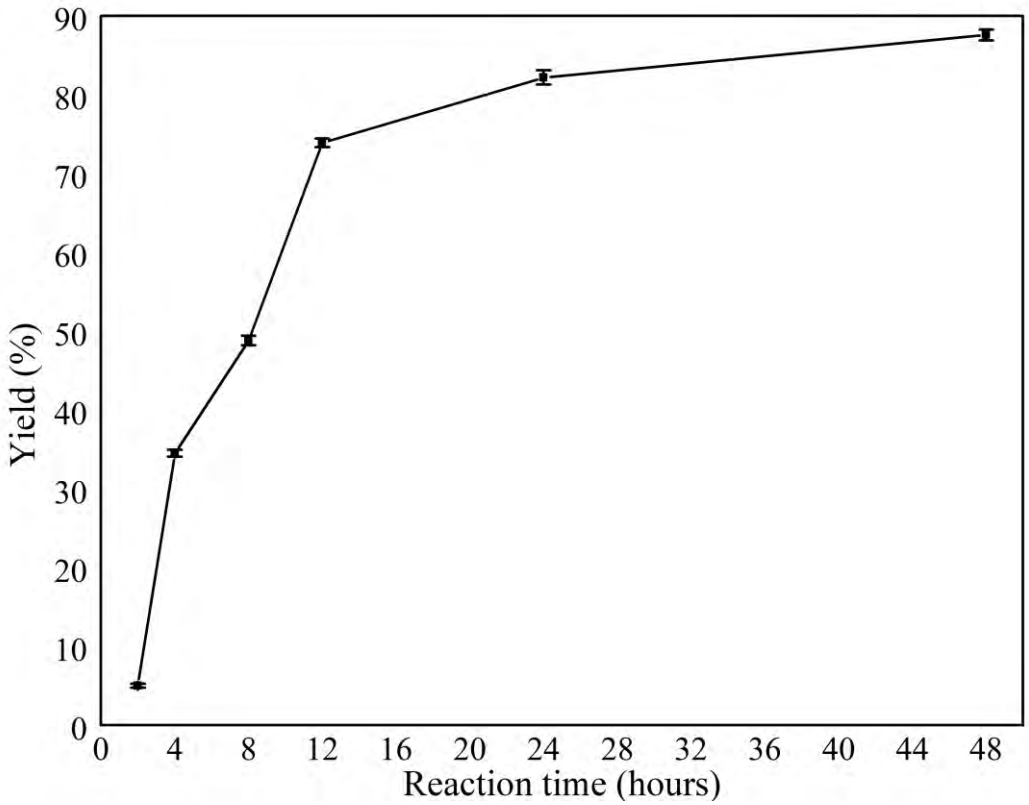

Figure 5.35: *Graph of time against percentage yield for the reaction between cyclohexene (9.87 mmol), methanol (494.3 mmol) and solid CO_2 (11.578 atm) in the presence of 2 mol % Ru3(CO)12 and 2 equivalents [BMIM]Cl ionic liquid at 160 ℃.*

In order to verify if CO_2 dissolution (or CO_2 in general) participates in the reaction, we repeated the experiments under completely inert conditions, purging the reaction solutions with argon gas to displace dissolved CO_2. These experiments illustrated no methyl cyclohexanoate formation even after 72 hours, which exemplifies the importance of CO_2 in the reaction.

Since we used methanol as one of the reactants, we presume that the methoxy group is as a result of methanol consumption. This was verified by repeating the reaction with the addition of deuterated methanol (CD_3OD, 1 ml), with the expectation of obtaining an isotopically labelled ester product. The reaction was allowed to proceed for 48 hours under identical reaction conditions used initially, and the products analysed using GC-MS. The fragmentation pattern obtained demonstrated the production of methyl cyclohexanoate with a molecular weight four units higher; thus, confirming that the methoxy group originated from methanol.

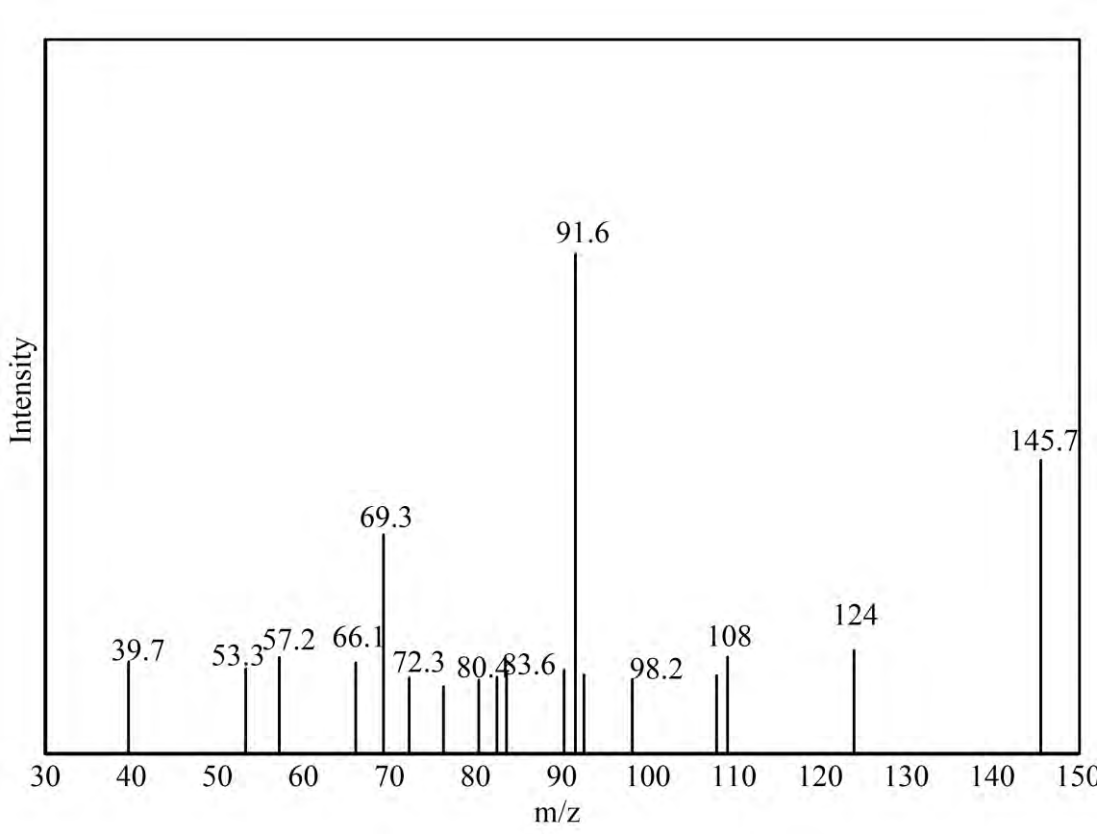

Figure 5.36: *Mass spectrum of ^2H labelled methyl cyclohexanoate*

It was also important to establish if these reactions occur in the absence of the added catalyst as well as the ionic liquid used. We established that the esterification reaction does not occur in the absence of $Ru_3(CO)_{12}$ as the catalyst. This indeed proves that $Ru_3(CO)_{12}$ plays an integral role in lowering the activation energy of this reaction at moderate temperatures and pressures.

Similar results were obtained in the absence of $[BMIM]^+Cl^-$, indicating that the ionic liquid also plays an important role in the reaction. From a literature survey[94 95] this can be due to several reasons, including:

- Enhancing the solubility of reactants and catalysts
- Stabilizing the reactive intermediates formed during the catalytic reaction by surrounding these species with a solvating shell, thus promoting the desired reaction pathway
- Modifying various reaction factors such as acidity/alkalinity, polarity and hydrogen bonding capabilities within the reaction environment.

The exact role that $[BMIM]^+Cl^-$ plays in the presented reaction system is still contentious, and is a possible area of investigation for future studies.

Finally, it is important to determine the catalytic turnover – the ability of a catalyst to undergo multiple cycles of catalysis without being consumed in the reaction itself. These experiments were performed by recovering $Ru_3(CO)_{12}$ used in the initial reaction by evaporation of the organic reagents and products, while the catalyst and ionic liquid remained as a viscous liquid. This was verified by GC-MS analysis which only showed trace amounts of reactants/products being present. To the residue, we added similar amounts of cyclohexene, methanol and CO_2 and the reaction was allowed to proceed for 48 hours at 160 ºC and 11 atm.

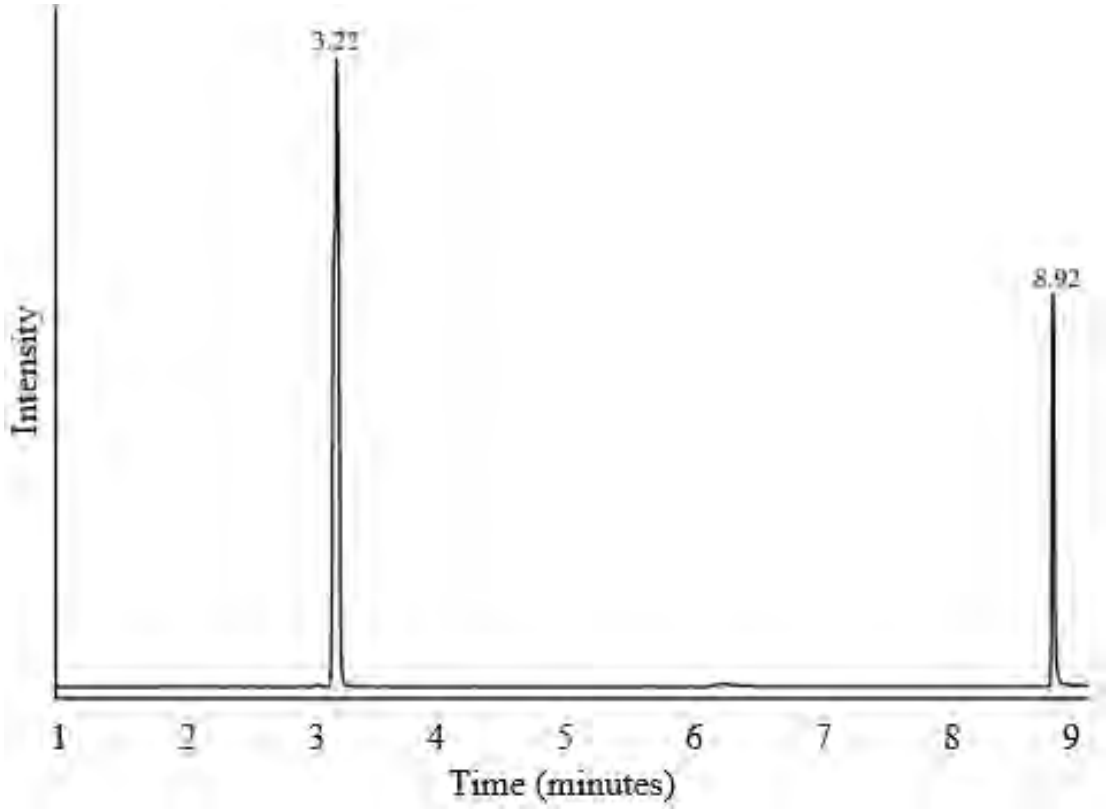

Figure 5.37: *Chromatographic profile of the products obtained when using recycled catalyst and ionic liquid after 48 hrs.*

The chromatograms obtained after analysing the reaction solution suggests the formation of a different product to methyl cyclohexanoate, indicated by the presence of a new peak at t_r = 8.92 min (**Figure 5.37**). The m/Z fragmentation pattern corresponding to the species eluting at 8.92 min suggest a product with a mass 14 units higher than that of methyl cyclohexanoate, (**Figure 5.38)**. The reason(s) for the formation of a different product is still unknown, but there is a strong experiment indication that the $Ru_3(CO)_{12}$ catalyst undergoes a structural change in geometry, which is known to impact catalytic performance and may lead to alterations in reactions pathways and product formation. Currently, there are limited literature reports detailing $Ru_3(CO)_{12}$ catalytic turnover numbers, or reports that $Ru_3(CO)_{12}$ undergoes structural changes which could influence in catalytic activity. Our current hypothesis is that under the reaction conditions, the $Ru_3(CO)_{12}$ complex forms higher nuclearity ruthenium carbonyl clusters. In turn, these clusters might catalyse different reactions.

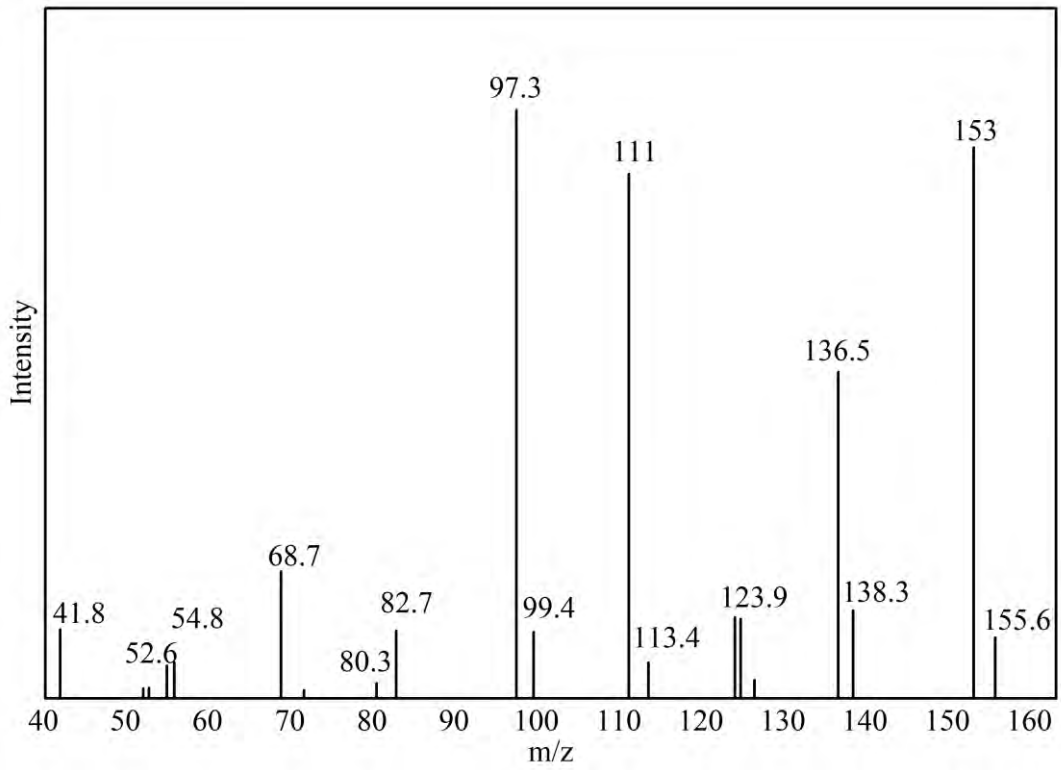

Figure 5.38: *Mass spectrum of the product obtained after reaction as a function of time, after 48 hours of reaction between cyclohexene (9.87 mmol), methanol (494.3 mmol) and CO_2 in the presence of recycled Ru complex and ionic liquid solution at 160 ℃.*

During the course of these investigations, there was one prominent change that was observed in the reaction mixtures (**Figure 5.39**). The colour of all the reaction solutions turned from yellowish to black after the reaction, with the colour change intensifying with increasing reaction time. This drastic colour change posed the question: "What is going on in our reaction?" Such an abrupt change could indicate a formation of a new chemical species with different optical properties.

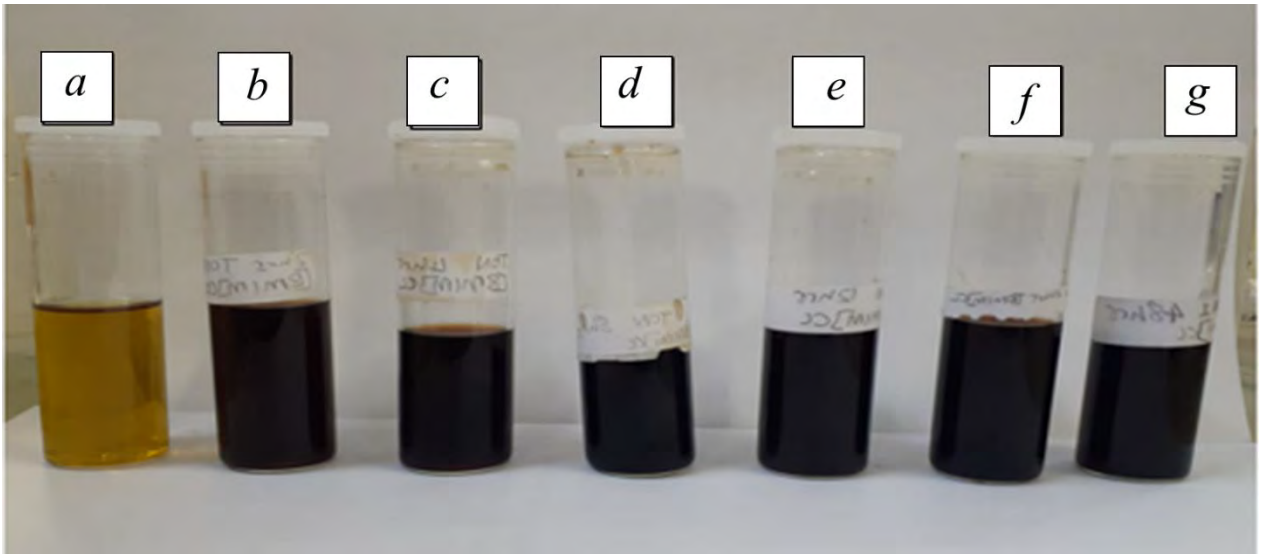

Figure 5.39: *Image depicting colour observations of solutions (a) before reaction, and solutions post-reaction after (b) 2 hours, (c) 4 hours, (d) 8 hours, (e) 12 hours, (f) 24 hours, (g)48 hours.*

To establish what is happening, we set-up a fractional distillation for one of the solutions from the reaction to separate each volatile compound. The distillates were observed to be clear and transparent, while the Ru complex and ionic liquid solution that was left behind remained black. Additionally, we heated each reaction component individually at 160℃ (MeOH, C_6H_{10}, [BMIM]Cl and $Ru_3(CO)_{12}$) to ensure that none of these components was the cause of these observations. No colour change was observed for MeOH, C_6H_{10}, and $[BMIM]^+Cl$; while $Ru_3(CO)_{12}$ changed colour from orange to black upon heating.

This result implies that $Ru_3(CO)_{12}$ transforms into a different species when heated above 70 ºC, therefore the colour changes observed during the course of the reactions are linked to the transformation of $Ru_3(CO)_{12}$ as a result of the reaction temperature, 160 ℃. This information is quite important since it implies that the $Ru_3(CO)_{12}$ moiety might not be the only catalytically active species present, which is in stark contrast to what is currently documented in literature[96] [97]. Furthermore, a thorough literature survey revealed limited information of the colour changes observed during these reactions, as well as the different catalytically active Ru species involved.

5.3. Conclusion

In the first section of this chapter, synthesis of heterogeneous catalysts, Au/TiO_2, Fe/TiO_2, Ni/TiO_2 and Ru/TiO_2 was performed. Utilizing nitrate salt precursors for base metals (Fe and

Ni) 25 % metal loading was used, while for precious metals (Au and Ru) 0.5 % metal loading on to the support was used with chloride salt precursors. An extensive characterization was performed on the catalysts using solid-state UV-VIS, TEM, EDX, PXRD and BET techniques to confirm the deposition of the metals onto the metal oxide support as well as to study the changes that accompany this deposition.

UV-VIS showed a change in band-gap energy of the support from 3.20 eV to 2.89, 2.77, 2.99 and 3.02 eV for Ni, Fe, Ru and Au respectively. EDX spectrum of each catalysts displayed all the corresponding elements as expected. The morphological studies using TEM showed that the particle size of the catalysts was unchanged after deposition with an average size of 20 nm and a spherical shape. PXRD results for Fe/TiO_2 displayed no change after deposition due to similarity in size of Ti^{4+} (0.68 Å) Fe^{3+} cation (0.64 Å). Due to the larger size of Ni^{2+} (0.72 Å) the diffractogram of Ni/TiO_2 showed new peaks showing the disruption of the lattice struicture of TiO_2 by the Ni metal. The diffractograms of Au/TiO_2 and Ru/TiO_2 were similar to that of bare TiO_2 due to low percentage loading or the low detection limit of the instrument. BET analysis showed a decrease in pore volume and surface area upon addition of Ni and Ru, while upon Au and Fe addition there was a pore volume increase and surface area increase.

The catalysts were subsequently applied in a reaction between cyclohexene, water and CO_2 (11 atm) at the temperature of 150 ℃. This reaction was performed in attempt to synthesize the corresponding cyclohexane carboxylic acid. Unfortunately, the results from GC-MS analysis showed that the reactions using Fe/TiO_2, Ni/TiO_2 and Au/TiO_2 as catalysts produced oxidation products namely cyclohexenone, cyclohexanone and cyclohexane diol at different yields. Ru/TiO_2 on the other hand produced a hydrogenation product, cyclohexane. Upon the elevation of the temperature to 200 ℃ in an attempt to promote formation of desired product, all the catalysts were poisoned.

One of the catalysts, Fe/TiO_2 was further applied to *N*-formylation of primary and secondary amines in the presence of Hantzsch 1,4-dihydropyridine, CO_2, $[EMIMI]^+Br^-$ under mechanochemical conditions. Under relatively mild, reaction conditions, the *N*-formylation reaction furnished the anticipated formamides in good to excellent yields (75-99%).

In the second section, homogeneous catalysis was applied. The reaction was performed using cyclohexene, CO_2, methanol in the presence of $Ru_3(CO)_{12}$ as a catalyst and $[BMIM]^+Cl^-$ as a promoter. $[BMIM]^+Cl^-$ was successfully synthesized and characterized using ^1H NMR and

ATR-FT-IR then used in the reaction while the catalyst was utilized as obtained from the supplier. This reaction was performed to get a methyl cyclohexanoate as a product which was synthesized successfully with a yield of 27% when using gaseous CO_2. The yield improved to 87% when using solid CO_2 indicating a better absorption into the reaction. The color changes observed in the reaction media from yellowish to black as a result of possible transformation of $Ru_3(CO)_{12}$ prompted a further investigation on the catalyst alone.

6 Characterization of $Ru_3(CO)_{12}$ with thermal treatment

6.1 Introduction

In the previous chapter we saw colour changes in our reaction solutions and we want to establish its cause. The initial thought was that it could be due to the formation of ruthenium metal oxides, which is known to be black in colour. This was later discarded as there were no indication of oxidation state change of Ru^0 (in combination with studies conducted under completely inert conditions). This is further substantiated with reference to the hard-soft acid-base (HSAB) principle which states that hard acids favour coordination with hard bases while soft acids prefer soft bases. Non-polarizable small acceptor or donor atoms with high charge density are regarded as hard acids or bases respectively, while polarizable large acceptor or donor atoms with low charge density are classified as soft acids or bases respectively.[98 99] Since there are no other ligands involved in the experiments, there would be nothing to stabilize the "harder" metal center if oxidation does take place.

A number of literature reports were explored where $Ru_3(CO)_{12}$ was used as a catalyst with reactions involving CO_2 and olefins. These studies focussed on the the mechanistic aspects of how this cluster complex catalyses these reactions. The use of $Ru_3(CO)_{12}$ as a catalyst for reactions involving olefins and CO_2 in literature has been applied in hydroformylation, hydrocarboxylation and oligomerization reactions.

Hydroformylation can happen in different approaches. Firstly literature reports the use of syngas and alkenes in the presence of $Ru_3(CO)_{12}$ as a catalysts precursor, 2,2-bipyridine (BIPY) as a promoter and tetrabutylphosphonium bromide (Bu_4PBr) as an ionic liquid solvent to regioselectively obtain oxo-alcohols and aldehydes[100]

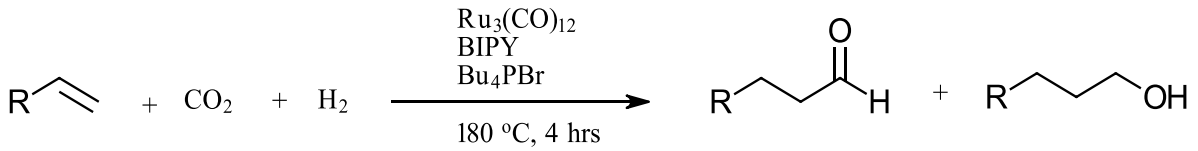

Scheme 6. 1: *Hydroformylation of olefins with CO_2 and H_2 in the presence of 2,2-bipyridine promoter, tetrabutylphosphonium bromide ionic liquid and $Ru_3(CO)_{12}$*

It has been postulated that the above reaction follows a number of steps of which the first step is the formation of an anionic ruthenium carbonyl cluster through the protonation of $Ru_3(CO)_{12}$.

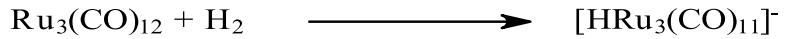

Scheme 6.2: *Protonation of $Ru_3(CO)_{12}$ with H_2 to form an anionic ruthenium carbonyl cluster $[HRu_3(CO)_{11}]^-$*

The next step is the reaction of $[HRu_3(CO)_{11}]^-$ with the promoter BIPY to form a chelate complex.

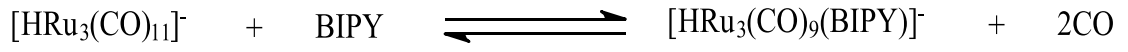

Scheme 6. 3: *Complexation of $[HRu_3(CO)_{11}]^-$ with BIPY to form a chelate complex $[HRu_3(CO)_9(BIPY)]^-$ that will act as a catalyst in the hydroformylation reaction*

The proposed mechanism for the catalytic reaction is as follows:

- Association of the olefin into the chelate complex
- Hydride transfer to coordinated olefin to form an alkyl-ruthenium cluster
- Release of an alkane
- Association of CO and H_2 molecules to form the corresponding oxo-alcohol and aldehyde

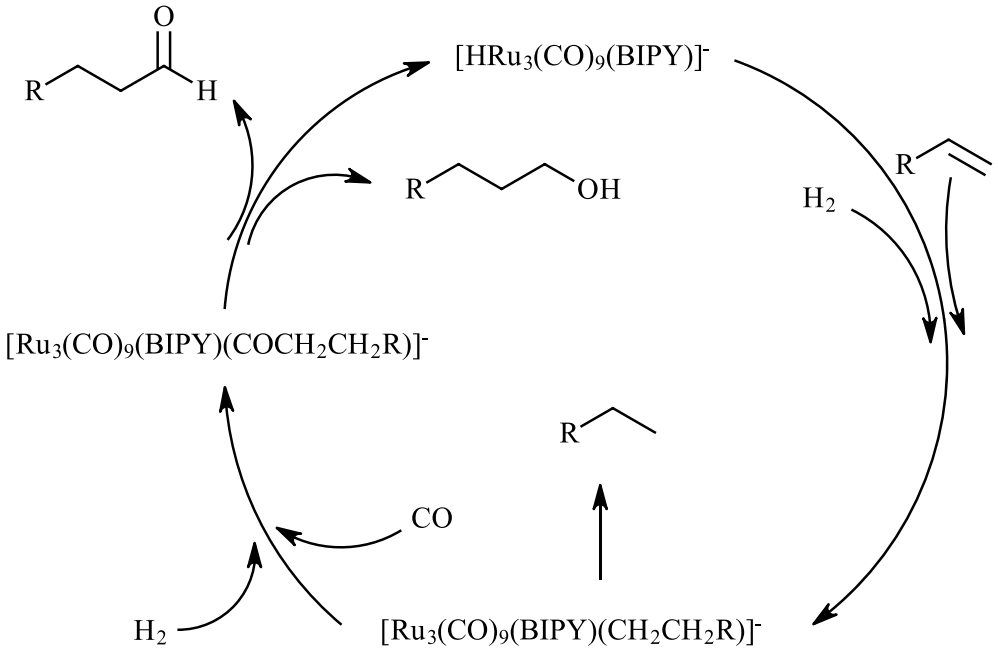

Scheme 6.4: *Illustration of the general reaction mechanism of the hydroformylation reaction between olefins, CO_2 and H_2 facilitated by the in-situ formed chelate complex $[HRu_3(CO)_9(BIPY)]^-$*

Secondly, hydroformylation reactions have been reported in literature to happen through water gas shift reactions (WGSR) under basic and acidic conditions. The important starting materials here are CO and H_2O. During the catalytic cycle, H_2 is produced in situ through the reduction of H_2O by CO. The produced H_2 is in turn used up together with the CO to incorporate into the double bond of the olefin to produce an aldehyde and alcohol. An example of this reaction from literature is the hydroformylation of an olefin in the presence of CO, H_2O, THF and $Ru_3(CO)_{12}$.[101]

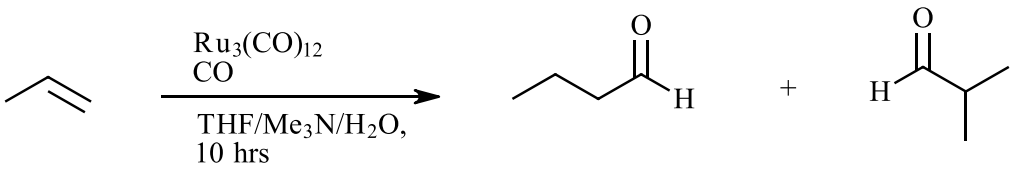

Scheme 6.5: *Hydroformylation of olefins with CO and H_2O through a water gas shift reactions under acidic/basic conditions in the presence of $Ru_3(CO)_{12}$ in THF for 10 hours*

Under acidic conditions, it is assumed that the very first step is to convert $Ru_3(CO)_{12}$ in situ to catalytically active specie $Ru_2(CO)_9$ then the catalytic cycle proceeds. It is postulated that the mechanism takes place as follows:

- Protonation of the active carbonyl complex to form a ruthenium carbonyl hydride cation, $[HRu_2(CO)_9]^+$
- Coordination of CO to form a neutral ruthenium carbonyl hydride, $HRu_2(CO)_{10}$
- Activation of the carbonyl by H_2O to form a metallacarboxylic acid, $HRu_2(CO)_9COOH$, with the release of a proton
- Decarboxylation to form another ruthenium carbonyl hydride, $H_2Ru_2(CO)_9$, releasing CO_2
- Reductive elimination to regenerate the catalytically active specie, releasing H_2

This type of reaction is not only applied for hydroformylation, it is also applied for reduction of a myriad of functional groups in organic synthesis.[101 102]

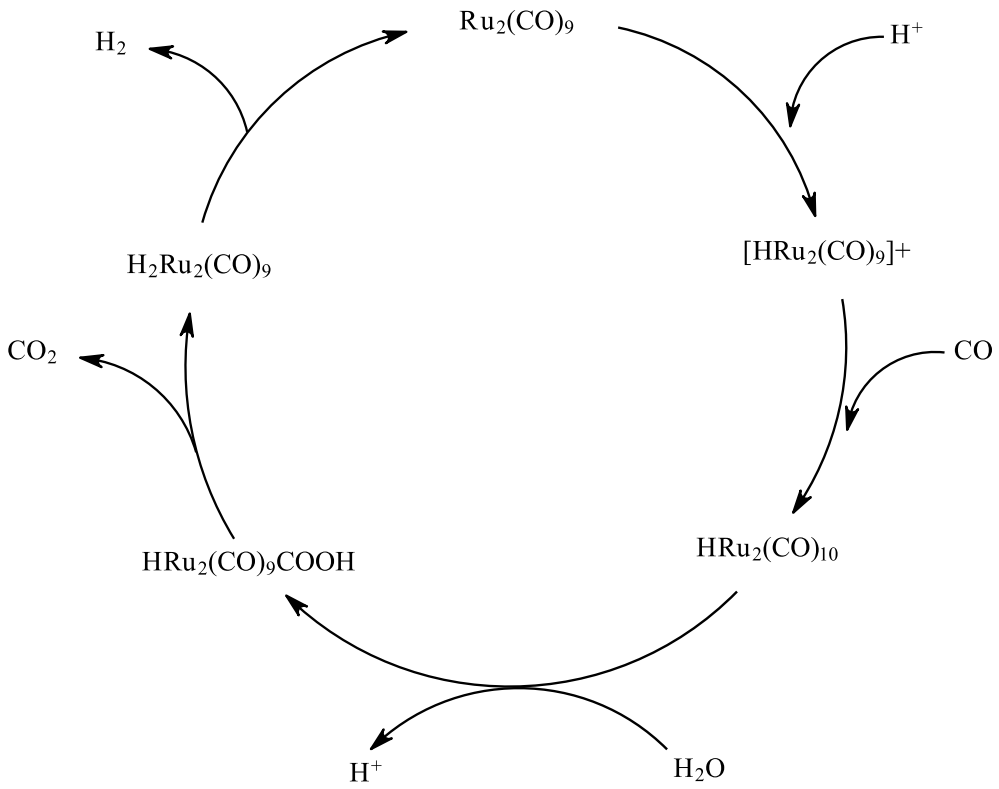

Scheme 6.6: *General mechanism of hydroformylation of olefins with CO and H_2O through a water gas shift reactions under acidic conditions with the conversion of $Ru_3(CO)_{12}$ to $Ru_2(CO)_9$*

Basic conditions on the other hand follow a different mechanism of reaction;[101 103]

- Activation of CO ligand through hydroxylation to form a metallacarboxylic acid, $Ru_3(CO)_{11}COOH$
- Decarboxylation of $Ru_3(CO)_{11}COOH$ to form a ruthenium carbonyl hydride anion, $[HRu_3(CO)_{11}]^-$
- Protonation of $[HRu_3(CO)_{11}]^-$ with H_2O to form a neutral ruthenium carbonyl hydride, $[H_2Ru_3(CO)_{11}]$
- Reductive elimination of H_2 forming $Ru_3(CO)_{11}$
- Coordination of CO to regenerate $Ru_3(CO)_{12}$

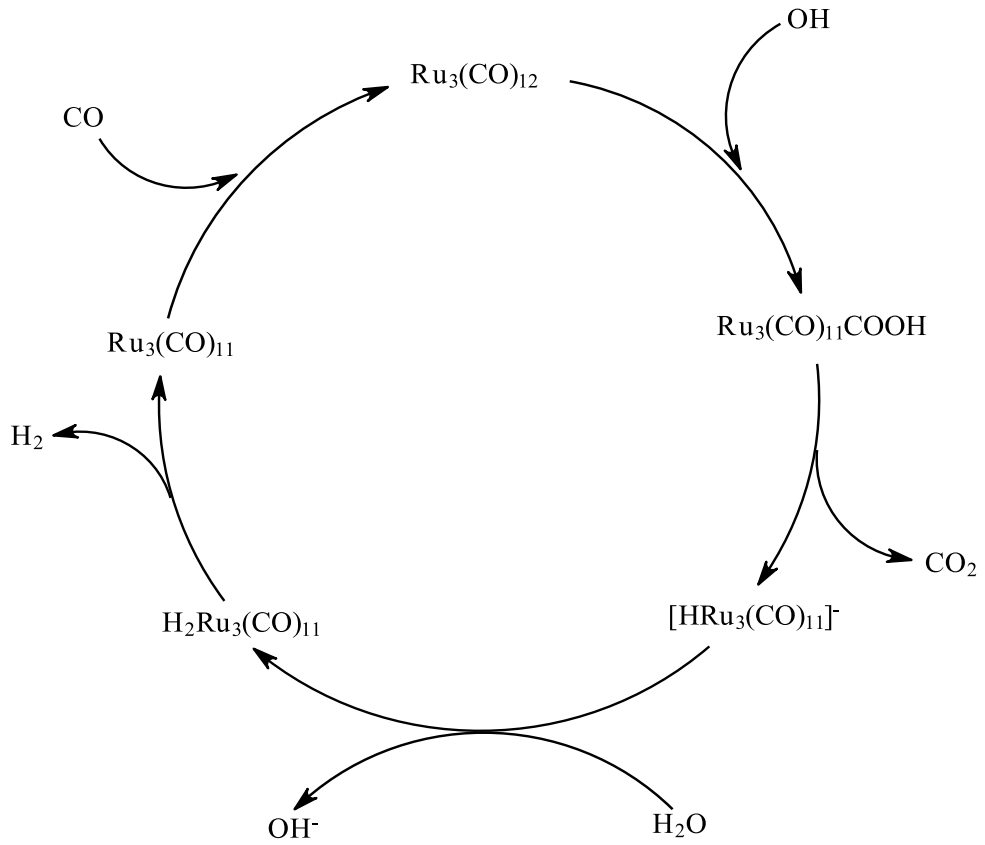

Scheme 6.7: *General mechanism of hydroformylation of olefins with CO and H_2O through a water gas shift reactions under basic conditions*

Lastly, reverse water gas shift reaction (RWGSR) is another process which hydroformylation is proposed to proceed by. An example of such a reaction is reported whereby cyclohexene, CO_2, H_2 are used as starting materials in the presence of $Ru_3(CO)_{12}$ as a catalyst, N-Methyl-2-pyrrolidone (NMP) as a solvent and LiCl as a promoter.[104 105]

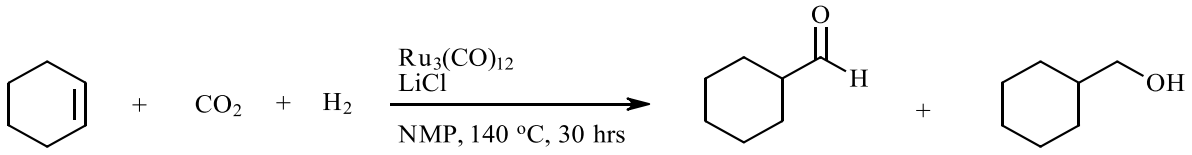

Scheme 6.8: *Hydroformylation of olefins with CO_2 and H_2 through a reverse water gas shift reactions in the presence of $Ru_3(CO)_{12}$ and LiCl promoter in N-methyl-2-pyrrolidone at 140 ℃ for 30 hours*

The literature only describes the mechanism of this reaction in two steps, no clear indication of how $Ru_3(CO)_{12}$ takes part in the catalytic cycle, the only thing stated is that $[H_3Ru_4(CO)_{12}]$ and $[HRu_3(CO)_{11}]^-$ complexes are identified as active species. It is hypothesized that H_2 reduces

CO_2 to CO, then the solution of the syngas produced in situ is used up for hydroformylation of the cyclohexene to produce cyclohexanecarboxaldehyde and cyclohexylmethanol.

Hydrocarboxylation is another type of carbonylation reaction that has been reported with $Ru_3(CO)_{12}$ and tetrakis(acetato)dirhodium(II) ($Rh_2(OAc)_4$ as a bimetallic catalyst. An example, is the carbonylation of a methyl group, from a phenyl ring of anisole, with CO_2 and H_2 in the presence of lithium iodide (LiI) and 1-hexyl-3-methylimidazolium tetrafluoroborate ([HMIM]BF_4) ionic liquid as promoters.[106]

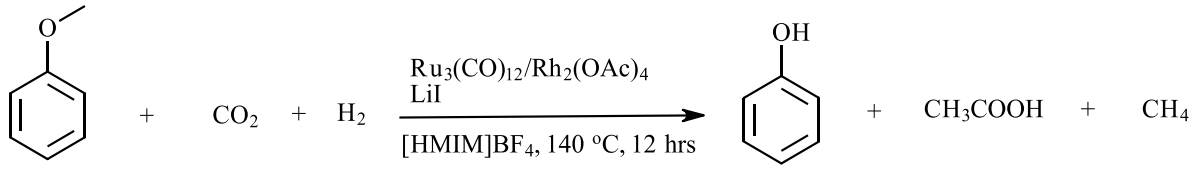

Scheme 6.9: *Carbonylation reaction of a methyl group on a phenyl ring of anisole, with CO_2 and H_2 in the presence of $Ru_3(CO)_{12}$/($Rh_2(OAc)_4$, LiI, [HMIM]BF_4 at 140 ℃ for 12 hours*

It is reported that the first step of the reaction mechanism is RWGSR, which is specifically catalyzed by $Ru_3(CO)_{12}$ and [HMIM]BF_4 while $Rh_2(OAc)_4$ and LiI catalyze the cleavage of the methyl group of anisole to react it with CO produced in the first step and H_2 to form the rest of the products. For the sake of our work, the only mechanism that will be reported on is that involving $Ru_3(CO)_{12}$.

The ionic liquid is particularly important in this reaction, without which the reaction does not take place. Moreover, within the ionic liquid itself the anion, BF_4^-, plays the most important role by interacting with $Ru_3(CO)_{12}$. The following mechanism has been proposed for this reaction;

- Ligand exchange between [HMIM]BF_4 and $Ru_3(CO)_{12}$ releasing CO, which will be used up in the reaction, and forming $[Ru_3(CO)_{11}(BF_4)]^-$
- Formation of a hydride complex $[HRu_3(CO)_{11}]^-$ through reaction of $[Ru_3(CO)_{11}(BF_4)]^-$ and H_2 releasing HBF_4
- Incorporation of CO_2 into the hydride complex to form a formate complex $[Ru_3(CO)_{11}(OCOH)]^-$
- Reaction of previously formed proton with the formate regenerating the starting complex $Ru_3(CO)_{12}$

- Incorporation of CO_2 into the hydride to form $[Ru_3(CO)_{11}(OCOH)]^-$ which then releases CO forming another formate $[Ru_3(CO)_{10}(OCOH)]^-$

- The formate then reacts with H_2 to form $[H_2Ru_3(CO)_{11}(OCOH)]^-$ which subsequently releases H_2O to regenerate the initially formed hydride complex $[HRu_3(CO)_{11}]^-$

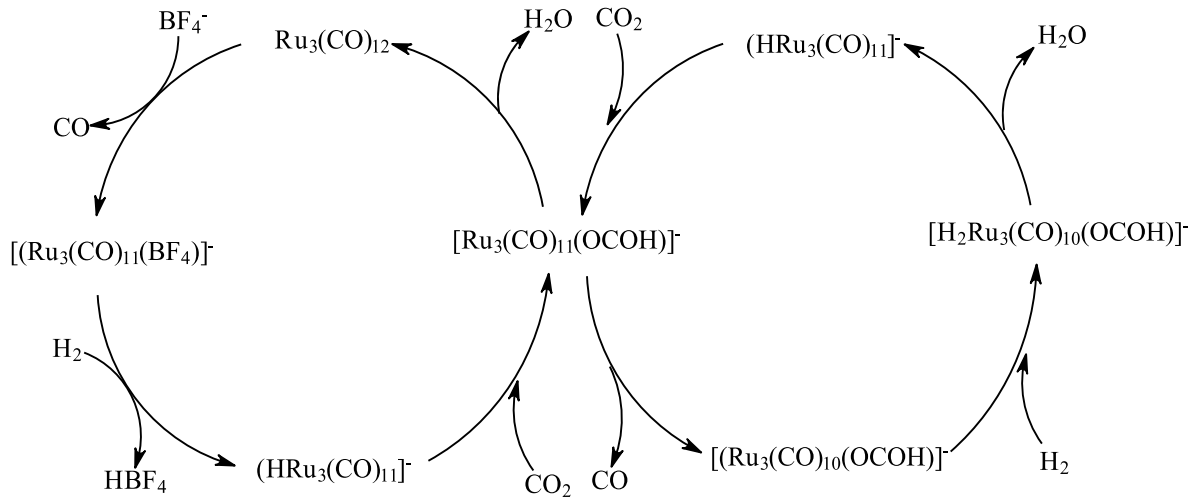

Scheme 6.10: *General mechanism illustrating carbonylation reaction of a methyl group on a phenyl ring of anisole, with CO_2 and H_2 in the presence of $Ru_3(CO)_{12}$/($Rh_2(OAc)_4$, LiI, [HMIM]BF_4 at 140 °C for 12 hours*

Lastly, oligomerization of ethylene has been reported to take place in the presence of $Ru_3(CO)_{12}$ in heptane as a solvent to form butene.

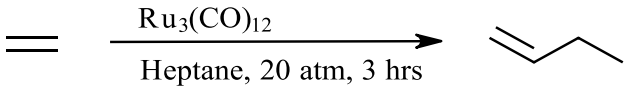

Scheme 6.11: *Oligomerization of ethylene to butene facilitated by $Ru_3(CO)_{12}$ in heptane at 20 atm for 3 hours*

It is presumed that for this reaction to happen ruthenium carbonyl hydride species must be formed as intermediates. Therefore, the following mechanism is postulated;

- Formation of a hydride releasing a CO

- Addition of ethylene which then forms ethyl derivative

- Ethylene insertion

- β-hydride elimination to form butene.

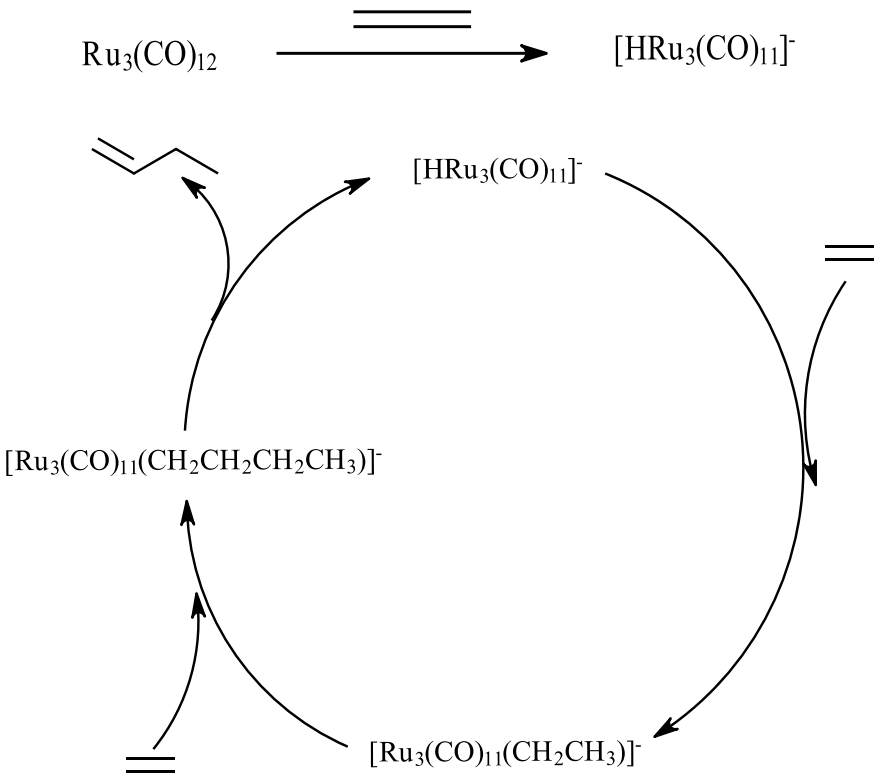

Scheme 6.12: *Mechanism of Oligomerization of ethylene to butene facilitated by $Ru_3(CO)_{12}$ in heptane at 20 atm for 3 hours*

Transition metal carbonyl compounds seems to be among the most versatile group of transition metal compounds. This versatility comes from the interaction of the metal and the carbonyl ligands. Firstly, the π-backbonding where the electrons from the d-orbital of the metal center move to the empty and degenerate π-antibonding LUMO of the carbonyl ligand. Secondly, the σ-donation of electrons from the ligand HOMO to the d-orbital of the metal center. This compounds can occur as mononuclear, binuclear and polynuclear/cluster complexes, which $Ru_3(CO)_{12}$ falls under.[107 108]

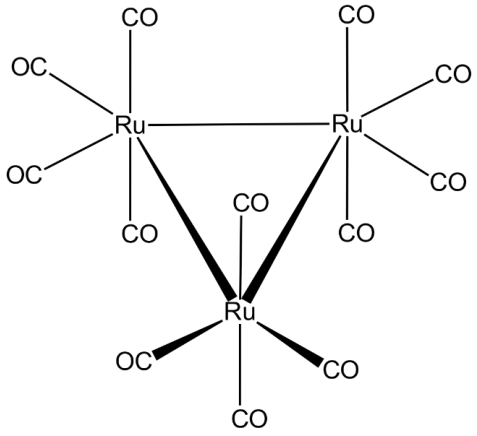

Figure 6.1: *Molecular structure of cyclo-tris(tetracarbonylruthenium)(3 Ru—Ru)*[109]

$Ru_3(CO)_{12}$ is a polynuclear triangular cluster with ruthenium atoms forming a triangle which is almost equilateral with 12 terminal carbonyls attached onto them (**Figure 6.1**) giving the compound a D_{3h} symmetry.[108 110 111] The accurate structure of the compound has axial Ru-CO bond lengths of 1.942 Å and equatorial Ru-CO bond lengths of 1.921 Å. The axial Ru-C-O bond angles are bent ranging from 172° to 173° because of the Van der Waals repulsions between the axial oxygen atoms. On the other hand, the equatorial Ru-C-O bond angles are linear with bond angles of 178° – 180°.[112]

The kind of reaction this complex follows depend on the type of electron transfer that is involved in a reaction regardless of whether it is inter or intramolecular transfer. The initial reaction step could either involve, electron addition (reduction) to the LUMO via nucleophilic attack, removal of electrons (oxidation) from the HOMO via electrophilic attack or it could be an intra-molecular transfer which is normally influenced by pyrolytic reactions. As electrophilic attack happens, π-backbonding decreases while nucleophilic attack increases π-backbonding. It is these π-backbonding adjustments by the CO ligands that facilitate more reactivity of the cluster with electrophilic and nucleophilic reagents. [113 114 115]

Going down the group the distance between HOMO and LUMO of metal carbonyl clusters increases as well as metal-metal bond strength, resulting in thermostability and chemical inertness. Ruthenium being in the same group as iron and osmium the reactivity of $Ru_3(CO)_{12}$ can be compared to that of triosmium dodecacarbonyl, $Os_3(CO)_{12}$ and triion dodecacarbonyl, $Fe_3(CO)_{12}$. It has been reported in literature that $Ru_3(CO)_{12}$ reacts with halogens giving monomeric species, $Ru(CO)_4X_2$, through cleavage of the metal bonds followed by

polymerization of the monomeric species to produce $Ru_3(CO)_{12}X_6$ species without the loss of CO groups.[113 116]

$Os_3(CO)_{12}$ on the other hand reacts with halogens to produce compounds with the formula, $Os_3(CO)_{12}X_2$. This difference in reactivity is stated to be related to the stability of the metal-metal bond.[117] Other literature reports that $Fe_3(CO)_{12}$ undergoes cleavage of the triangular moiety on its reaction with other substrates while $Ru_3(CO)_{12}$ regularly forms more stable trinuclear species. This difference in reactivity is linked to increase in stability of metal-metal bond going down the group.[118]

$Ru_3(CO)_{12}$ has been applied in catalysis for the activation of C=C, C=O, C=N double bonds of organic molecules. A few examples of this application is, the oligomerization of ethylene at atmospheric pressure and 100 ℃.[119] It has also been used as a homogenous catalyst for water gas shift reaction[120] and for hydroformylation of alkenes with CO_2 and H_2 in the presence of promoters at 150 ℃ to form aldehydes.[121] It is important to note that at the end of all these reactions different species of ruthenium carbonyl were identified e.g. $[Ru_3H_2(CO)_9(MeC{\equiv}CMe)]$, $[Ru_3H_2(CO)_9(EtC{\equiv}CEt)]$, $[Ru_3H(CO)_9(MeCCHCEt)]$, $[H_3Ru_4(CO)_{12}]^{-1}$, $[HRu_3(CO)_{11}]^{-1}$.

It has also been reported in literature that in a reaction where temperature conditions are high enough to allow a breakdown of the complex, these metal carbonyl clusters undergoes decomposition followed by condensation whereby the decomposed species bind again to form larger carbonyl clusters and most interestingly form carbide complexes.[122] There are a number of studies reported in literature that show how the $Ru_3(CO)_{12}$ cluster behaves and changes with temperature in different reactions in wet conditions (in solvents) and in dry conditions (without solvent).

It is reported that when $Ru_3(CO)_{12}$ is heated in benzene or cyclohexane, the complex forms a new cluster complex which crystallizes as red needles. The cluster was found to decompose above 235 ℃ under vacuum. Upon mass spectroscopic analysis, the molecular weight was found to be 1050 g/mol. The conclusion was that this cluster complex is $Ru_6(CO)_{18}$.[123] A development was made on this new cluster to accurately determine its structure. The same cluster was synthesized and with mass spectroscopic and XRD data the structure was deduced to be $Ru_6C(CO)_{17}$ a carbide cluster complex[124] which was also obtained when heating $Ru_3(CO)_{12}$ in chlorobenzene at 160 ℃.[119]

Some decomposition studies reported $Ru_3(CO)_{12}$ deposited on carbon in order to follow its decomposition in He at 39.9 ℃ and H_2 at 64.9 ℃. It was found that after 19 hours the complex completely decomposed without forming any stable cluster. There was no report on the intermediate clusters as a function of time except that as time progressed, the intensity of the carbonyl bands kept on decreasing until complete decomposition.

Transformation in H_2 on the other hand was also monitored with FT-IR and after only 10 minutes new species started forming, eventually the complex transformed to $H_4Ru_4(CO)_{12}$ after 21 hours. When the temperature was increased to 400 ℃ the $Ru_3(CO)_{12}$ complex eventually decomposed to metallic Ru in both He and H_2. The same study also reported that in solution, the $Ru_3(CO)_{12}$ incorporated some ligands into its structure forming new complexes as well as transforming into the following complexes; $Ru(CO)_5$, $Ru_5C(CO)_{15}$, $[Ru_6(CO)_{16}C]^{2-}$, $Ru_6(CO)_{17}C$ and $[Ru_6(CO)_{18}]^{2-}$.[125] Another study has shown that $Ru_3(CO)_{12}$ decomposes to metallic Ru and CO gas under argon and nitrogen using TGA and DSC.[126]

More literature reports show that pyrolysis of $Ru_3(CO)_{12}$ in a sealed tube transforms to $Ru_6C(CO)_{17}$ of which upon carbonylation with CO at 70 ℃ produces $Ru_5C(CO)_{15}$ and $Ru(CO)_5$.[127] Work that was done on thermal decomposition of $Ru_3(CO)_{12}$ under variable temperature mass spectrometry in the gas phase shows results that are far different. At 226 ℃ the complex stayed intact. From 226 ℃ to 626 ℃ the complex transformed to eleven analogues; $Ru_3(CO)_{11\ to\ 1}$. Above 626 ℃ all CO ligands were removed completely leaving Ru_3 species.[108] No carbide clusters were observed in this study.

Studies on the decomposition of $Ru_3(CO)_{12}$ impregnated onto TiO_2 interestingly reported that $Ru_3(CO)_{12}$ when deposited on TiO_2 at -173 ℃ adsorbs molecularly but when deposited at 27 ℃ it adsorbs dissociatively forming $Ru_3(CO)_9$. When the temperature is elevated to 127 ℃, 227 ℃ and 357 ℃ the complex transforms to $Ru_3(CO)_8$, $Ru_3(CO)_7$ and $Ru_3(CO)_3$ respectively.[128]

It is important to highlight that only one article from literature reported the color change in their reaction but does not explain what is the color change attributed to, therefore there is no consensus in literature about this. For that reason, the ambit of this study is to possibly determine the nature of this color change and the consequences of this changes.

Table 6.1: *Summary of possible decomposition products of $Ru_3(CO)_{12}$ according to literature*

Species	Molecular mass
$Ru_3(CO)_{11}$	611.33
$Ru_3(CO)_{10}$	583.33
$Ru_3(CO)_9$	555.33
$Ru_3(CO)_8$	527.33
$Ru_3(CO)_7$	499.33
$Ru_3(CO)_6$	471.33
$Ru_3(CO)_5$	443.33
$Ru_3(CO)_4$	415.33
$Ru_3(CO)_3$	387.33
$Ru_3(CO)_2$	359.33
$Ru_3(CO)$	331.33
Ru_3	303.33
$Ru_6C(CO)_{17}$	1094.33
$Ru_5C(CO)_{15}$	937
$[Ru_6(CO)_{16}C]^2$	1066
$[Ru_6(CO)_{18}]^{2-}$	1110

6.2 Results and discussion

The pure $Ru_3(CO)_{12}$ was placed in the oven at 70 ℃ for 3 weeks to allow complete transformation and it changed color from orange to black. From here the obtained product from the oven will be referred to as "black Ru complex" while the pure sample will be referred to "$Ru_3(CO)_{12}$". (**Figure 6.2**) shows the complex before and after applying heat.

Figure 6.2: *Image showing $Ru_3(CO)_{12}$ before (left) and after placing in the oven (right)*

The two samples, black Ru complex and $Ru_3(CO)_{12}$, were then characterized with different techniques, energy-dispersive X-ray spectroscopy, fourier transform infrared, powder X-ray diffraction and matrix-assisted laser desorption/ionization-time of flight mass spectrometry. The following results were obtained:

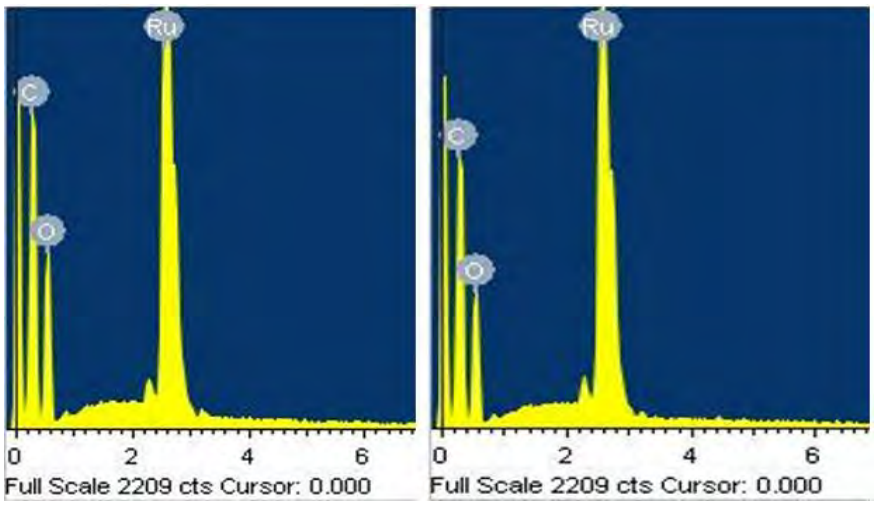

Figure 6.3: *EDX spectra of $Ru_3(CO)_{12}$ (left) and black Ru complex*

Results obtained from EDX display similar spectra for both orange and black Ru complex. The elemental contents of $Ru_3(CO)_{12}$ after heating at 70 ℃ are the same as before heating, both samples contain carbon, oxygen and ruthenium. This indicates that, there could be a rearrangement of the metal cluster forming a new specie/s without loss of the CO ligands or it could mean that there was an incomplete decomposition of the metal cluster with loss of some of the CO ligands.

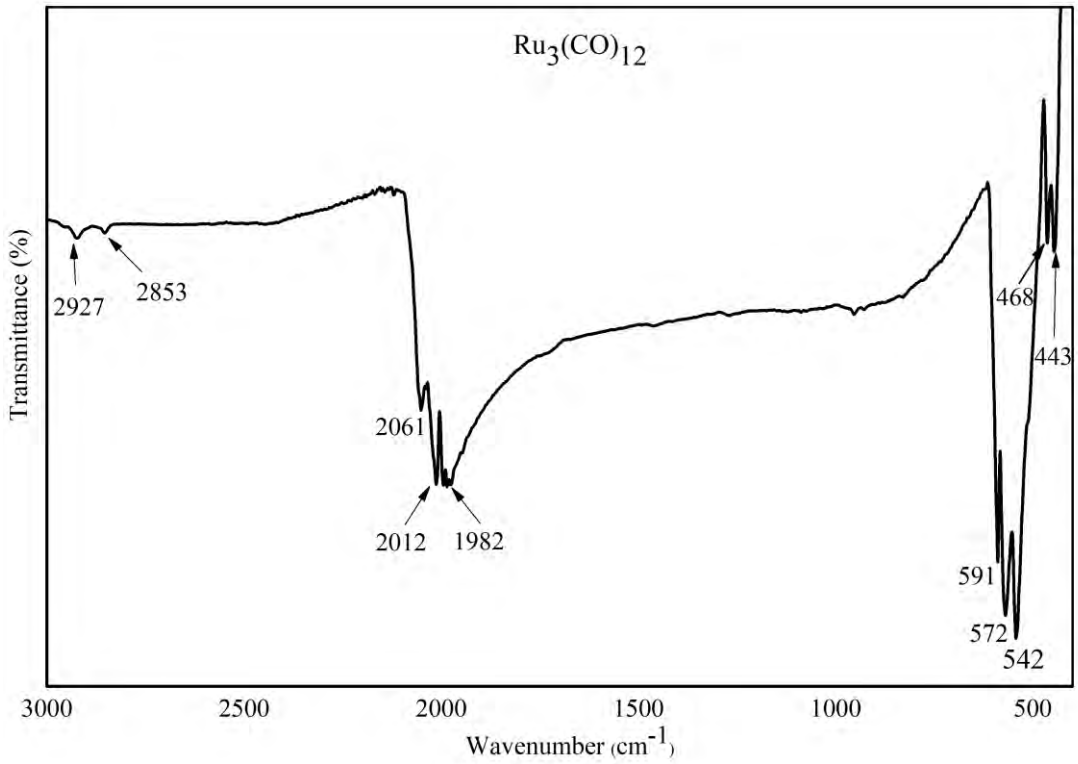

Figure 6.4: *FT-IR spectrum $Ru_3(CO)_{12}$ before subjecting it to heat*

The IR spectrum of $Ru_3(CO)_{12}$ displays three groups of bands; at 2927 to 2853 cm^{-1}, 2061 to 1982 cm^{-1} and 591 to 443 cm^{-1}. The more characteristic bands at 2061 to 1982 cm^{-1} are indicative of terminal carbonyl stretching vibrations while the bands at 591 to 443 cm^{-1} arise from metal carbon stretching vibrations.

Even though FT-IR as a technique can't necessarily show the exact number of carbonyl ligands, it is important to note that there is a significant overlap of modes of like symmetry. This is helpful to identify structural changes on $Ru_3(CO)_{12}$ in carbonyl region when the symmetry changes due to transformation of the complex to a bigger complex or removal of carbonyl ligands during decomposition.

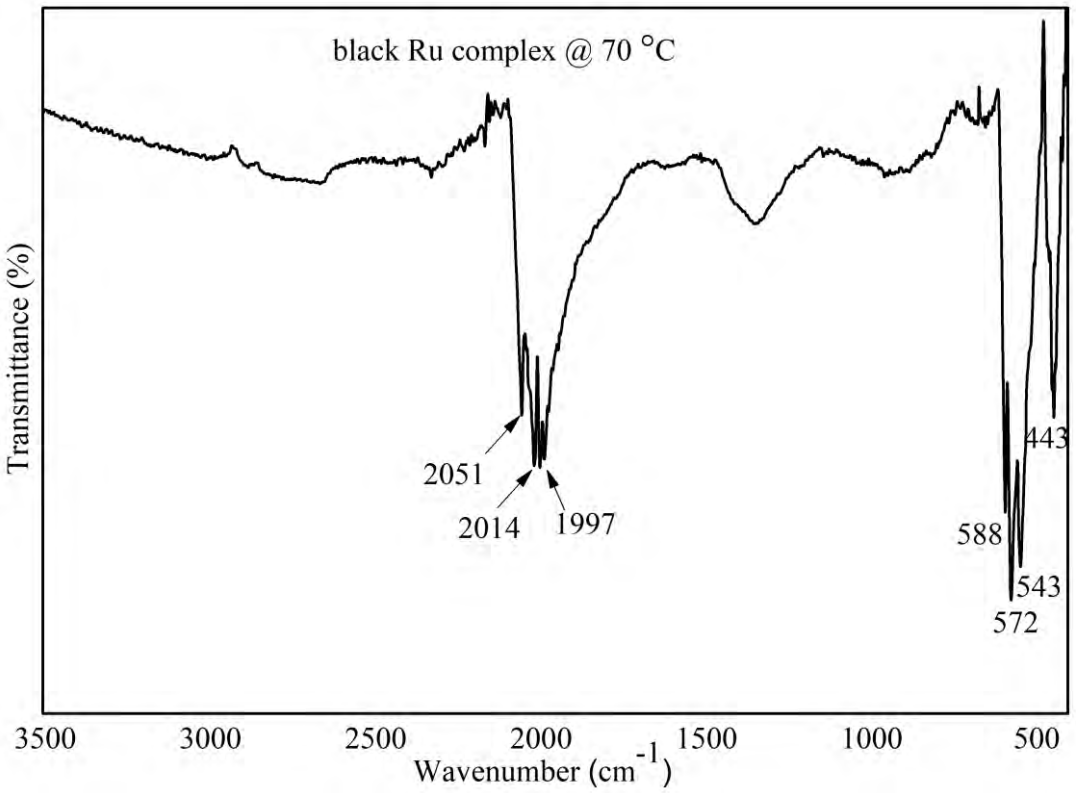

Figure 6.5: *FT-IR spectrum of the black Ru complex obtained after applying heat on the orange one at 70* ℃

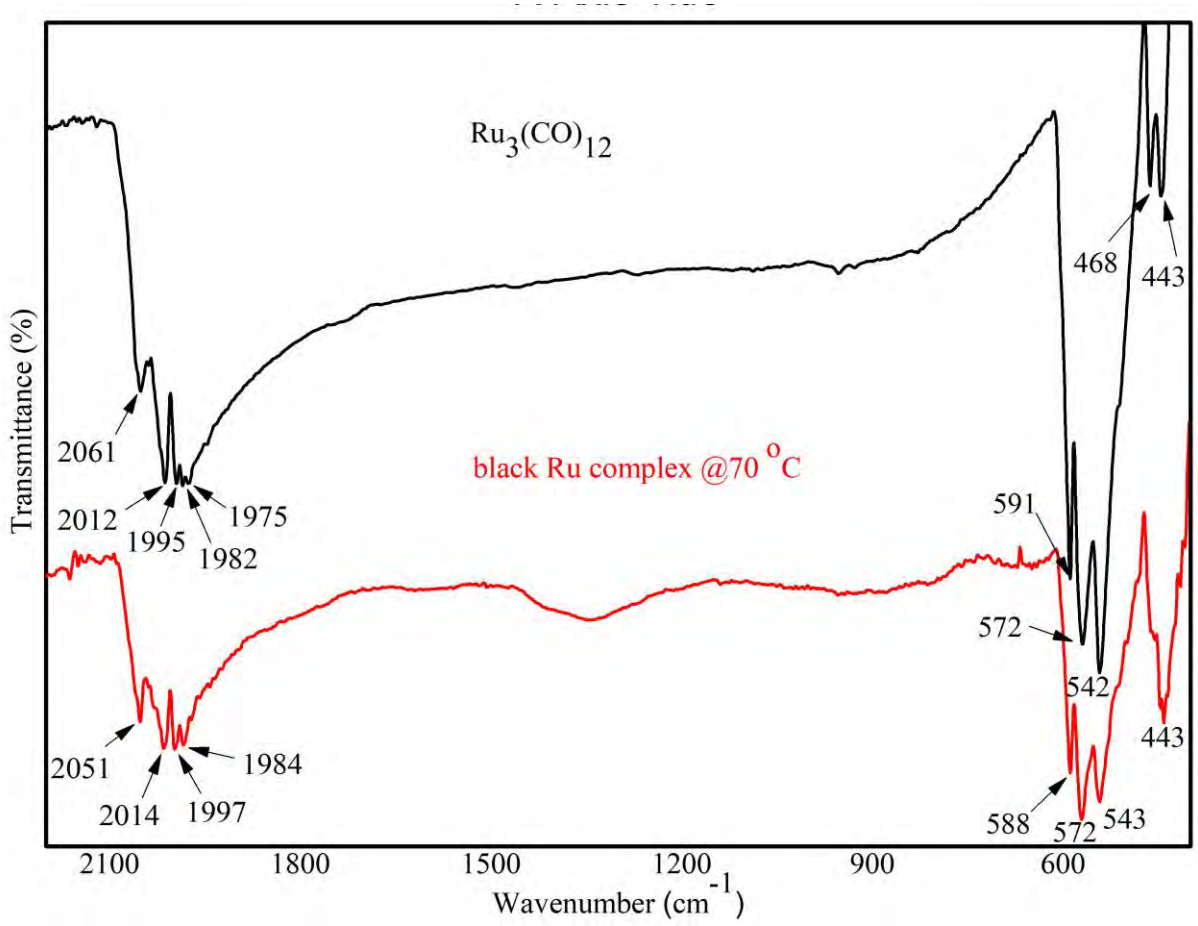

Figure 6.6: *Merged FT-IR spectra of $Ru_3(CO)_{12}$ and black Ru complex to highlight the differences*

There are a number of significant changes in the IR spectrum of $Ru_3(CO)_{12}$ after heating it at 70 °C. The bands at 2927 and 2853 cm^{-1} disappeared entirely. In the carbonyl region, the band at 2061 cm^{-1} has shifted to 2051 cm^{-1}, 2012 cm^{-1} shifted to 2014 cm^{-1}, 1995 cm^{-1} shifted to 1997 cm^{-1}. The magnified spectra in (**Figure 6.7**) shows that the band at 1975 has shifted to 1970 cm^{-1}. There's also an appearance of new carbonyl bands at 1958 and 1943 cm^{-1}. In the metal carbon region, the band at 591 shifted to 588 cm^{-1}, 542 shifted 543, 468 shifted to 464 cm^{-1}. There's also appearance of new bands at 455, 447, 435, 415 and 408 cm^{-1}.

This small shifts in wave numbers imply a change in bond lengths. A change to higher wavenumber means the bond length of the carbonyl or metal carbon bond has become shorter, conversely a change to lower wavenumber means elongated bond length of the carbonyls or metal carbon bond indicating a change in symmetry of the cluster. The appearance of new carbonyl and metal carbon bands indicate a change in symmetry of the cluster.

Within the structure of the $Ru_3(CO)_{12}$ the carbonyls producing the bands at 2012, 1995, 1982 and 1975 cm^{-1} seem to be of equal intensities meaning their dipole moment is similar, while

the carbonyl at 2061 cm^{-1} has a lower intensity which means that it has the lowest dipole moment amongst all the carbonyls. Black Ru complex on the other hand has carbonyls bands with different intensities; the bands at 2014 and 1997 cm^{-1} have the highest intensities meaning higher dipole moment while the bands at 1984, 1970, 1958 and 1943 cm^{-1} have respectively decreased intensities therefore decreasing dipole moment.

Similar changes are observed in the metal carbon bands, in the $Ru_3(CO)_{12}$ the band at 542 cm^{-1} has the highest intensity, followed by 572 cm^{-1} then 591 cm^{-1}, the bands at 468 and 443 cm^{-1} on the other hand have almost similar intensities. In contrast, the metal carbon bands of the black Ru complex look different, the band at 572 cm^{-1} has the highest intensity followed by 543 cm^{-1} then 588 cm^{-1}, the bands from 464 to 408 cm^{-1} on the other hand all have different intensities with 443 cm^{-1} having the highest intensity. Since the components of the complex haven't changed, they still are Ru, C and O we can relate the change in dipole to change in bond lengths. The lower the dipole moment seen from lower intensity, the shorter the bond and vice versa.

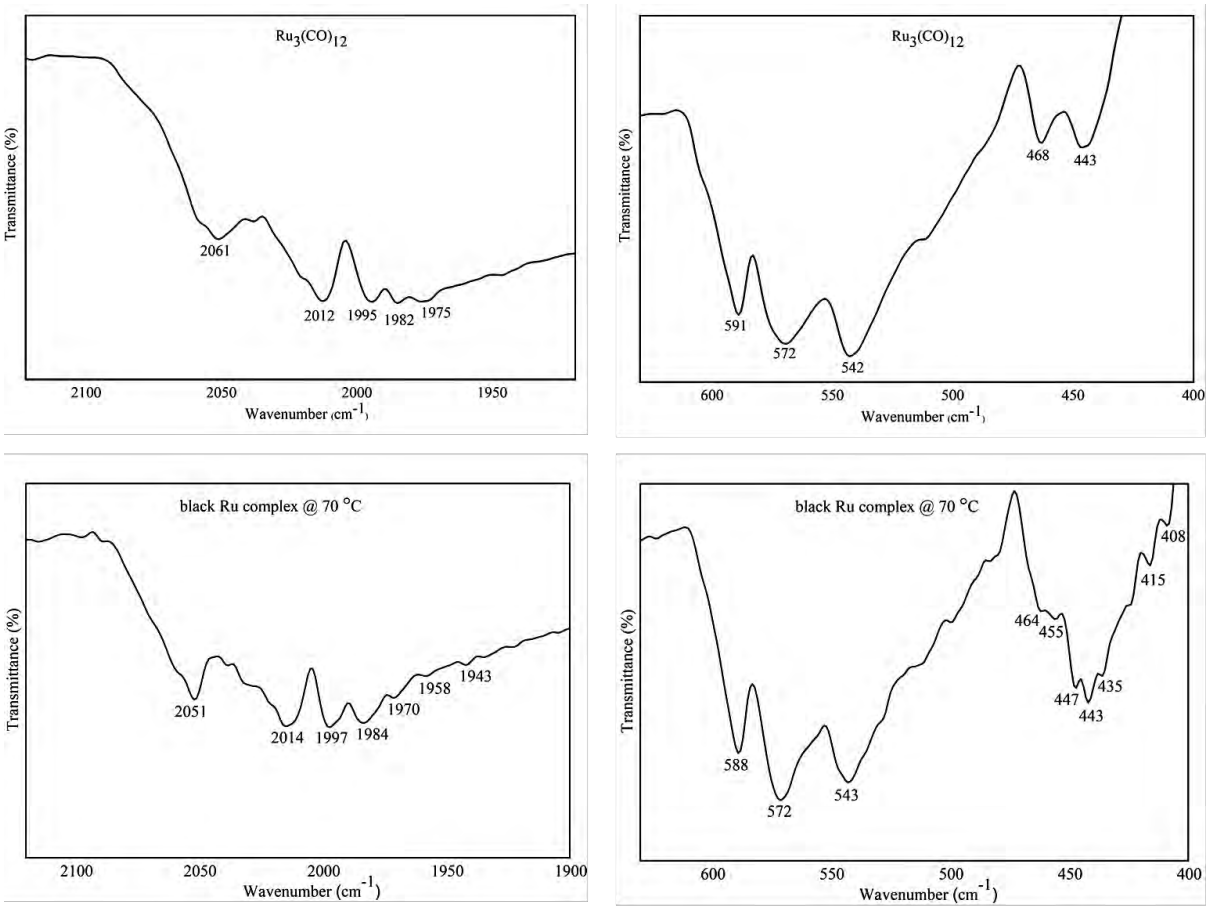

Figure 6.7: *Enlarged ATR-FT-IR spectra of "orange" and "black" $Ru_3(CO)_{12}$ highlighting the differences in the carbonyl and the metal–carbon bands*

The elongation and shortening of the bond lengths in the complex implied by the changes seen on the IR spectrum of the black Ru complex arise from the intra-molecular electron transfer between the Ru metal centers and the carbonyl ligands through σ-donation from the HOMO of the carbonyl ligands which causes shortening of the CO bond length. It also happens through π-donation from the metal d-orbital to the carbonyl ligand LUMO resulting in the elongation of the CO bond length.

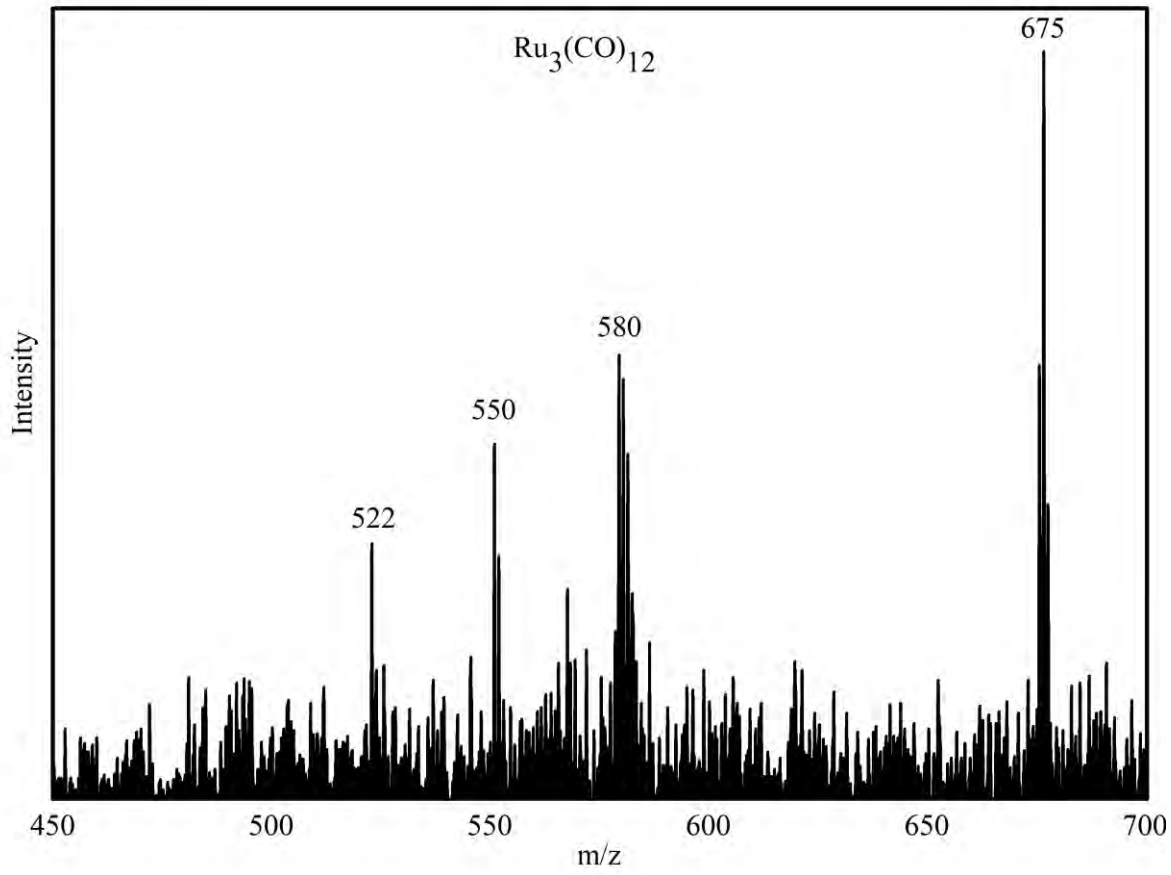

Figure 6. 8: *MALDI-TOF Mass spectrum of $Ru_3(CO)_{12}$*

The mass of orange and black versions of $Ru_3(CO)_{12}$ were determined using MALDI-TOF MS in the presence of dithranol matrix. The spectrum of orange $Ru_3(CO)_{12}$ shows the mass of 675 g/mol; with the theoretical mass being 639.33 g/mol. There is a 36 g/mol mass difference which could possibly result from the matrix. Since this technique applies a soft ionization, the complex does not undergo extensive fragmentation. The fragmentation pattern displays another peak at m/Z = 580 g/mol, possibly due to losing two CO groups from the complex; followed by 550 g/mol after losing one CO group from the last fragment then lastly 522 g/mol from losing a single CO group. A total of four CO groups were lost in this process.

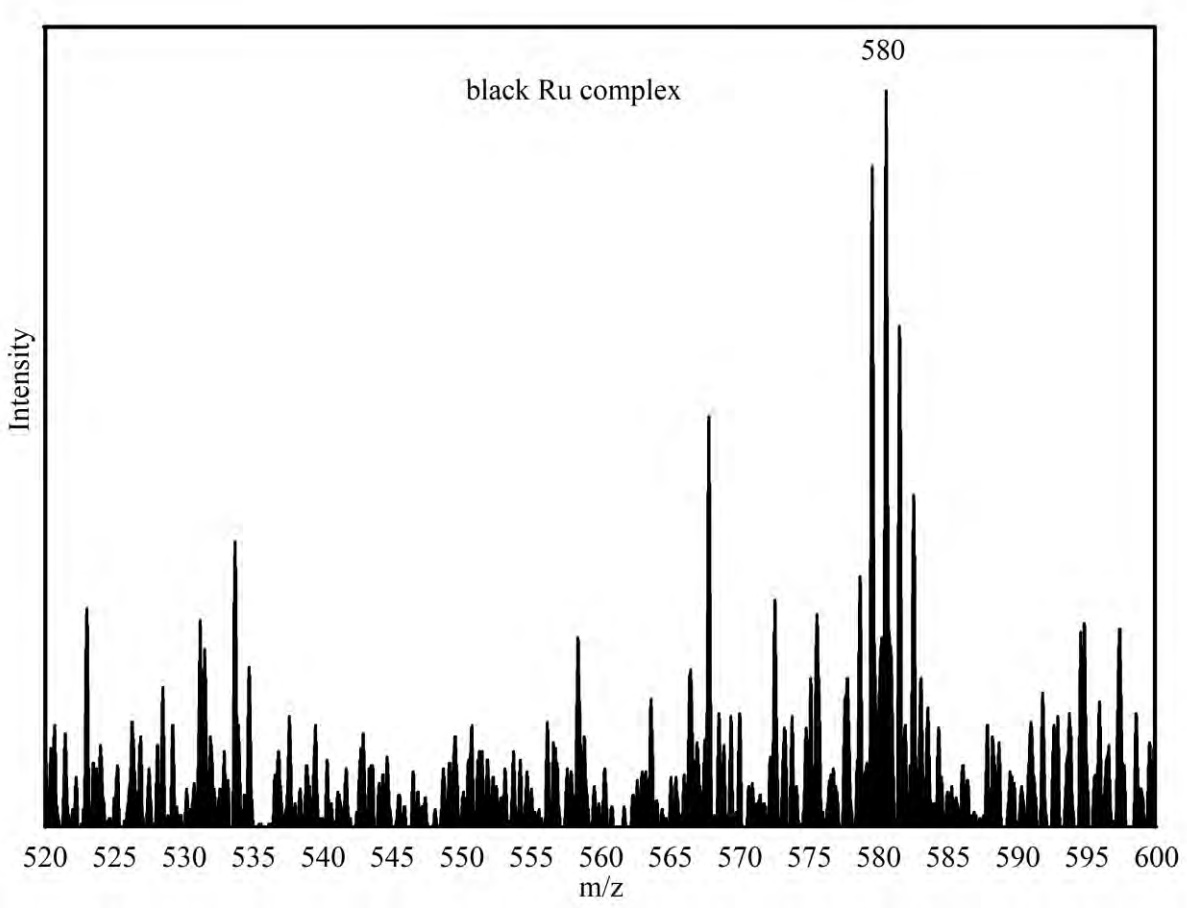

Figure 6.9: *MALDI-TOF Mass spectrum of black Ru complex*

The spectrum of black Ru complex on the other hand shows one peak with a mass of 580 g/mol indicating that two CO ligands were lost during the pyrolytic process in the oven. Therefore, the resulting complex in this case should be $Ru_3(CO)_{10}$. The lack of a fragmentation pattern in the mass spectrum of this resulting specie demonstrates, to a certain degree, the stability of this formed complex.

i. Analysis of the two variants of $Ru_3(CO)_{12}$ *via* Powder X-ray Diffraction

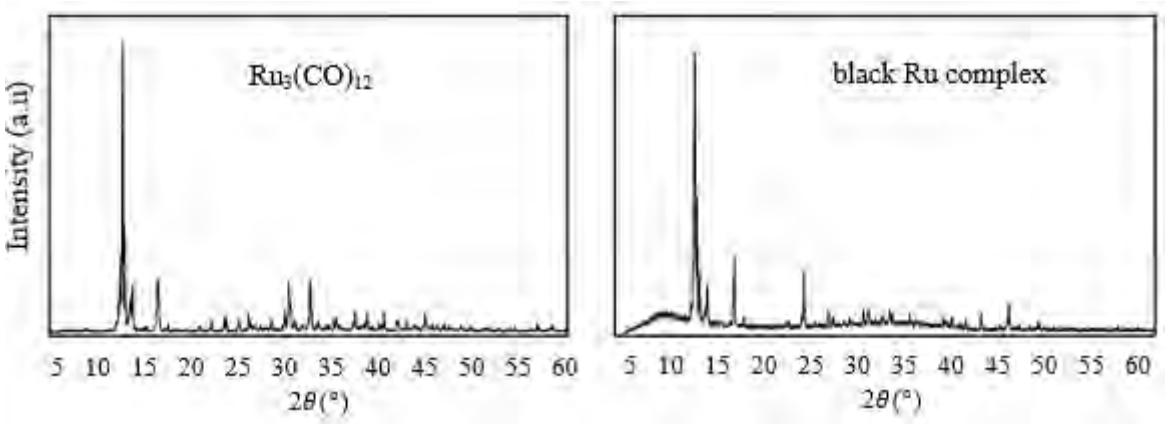

Figure 6.10: *PXRD diffractograms for orange and black variants of $Ru_3(CO)_{12}$*

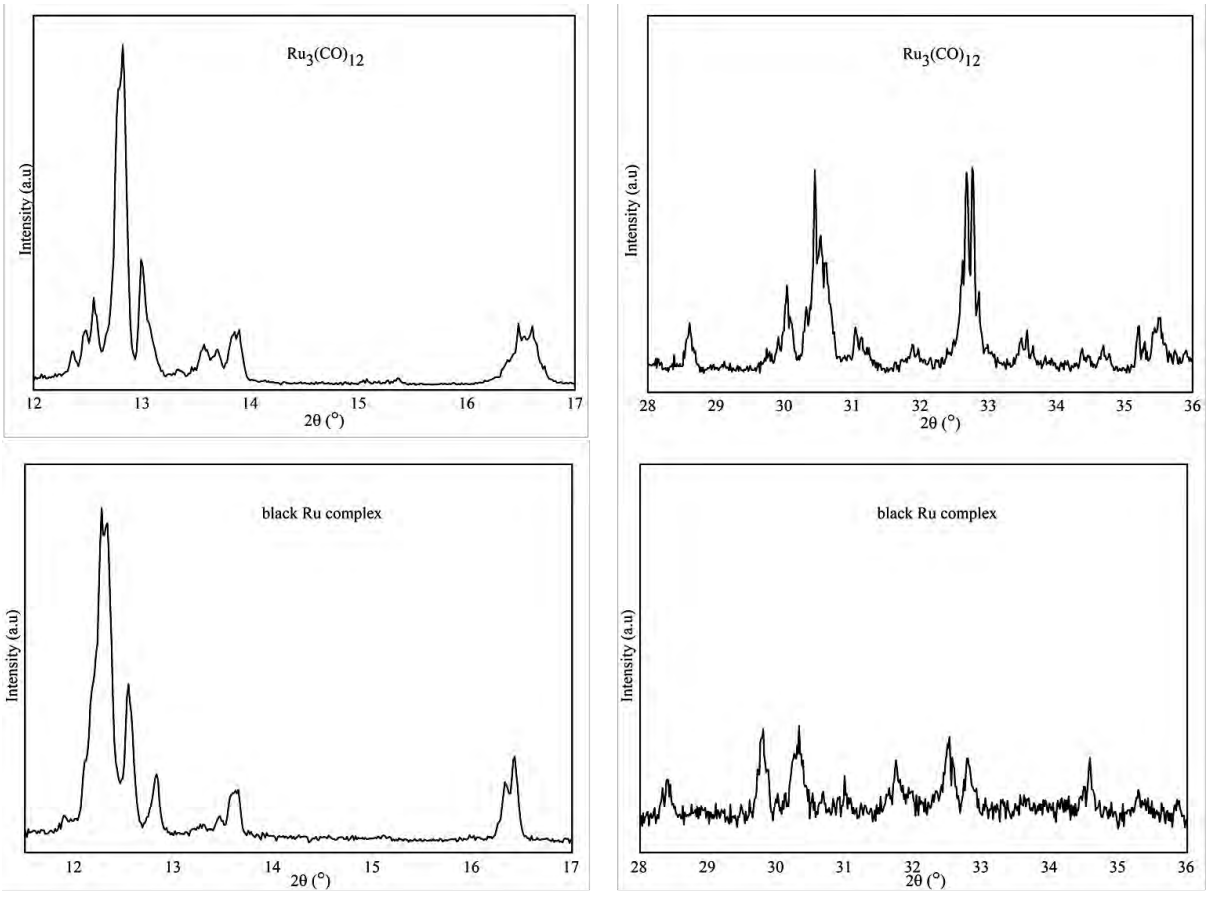

Figure 6.11: *Magnified XRD diffractograms of $Ru_3(CO)_{12}$ and black Ru complexes from 11 – 17 (2θ(°)) and 28 – 37 (2θ(°)) to highlight the observed differences*

The diffraction pattern (**Figure 6.10**) of the black Ru complex and orange $Ru_3(CO)_{12}$ look similar but upon magnification (**Figure 6.11**) the differences becomes evident. The orange variant has three overlapping peaks at 12^o which is absent from the black variant. There's a

new peak that appeared at 12.8° in the black complex which is absent on the orange variant. In the orange complex, the peak at 13.6° is split into two peaks at the top while in the black one of the peaks disappear. Moreover, the peak at 16.5° is broad with its top splitting into two peaks with equal intensities but this peak in the black has the two peaks with different intensities with the right peak being more intense that the left peak.

Another major difference is that the peak at 24.6° in the diffractogram of the orange $Ru_3(CO)_{12}$ has low intensity while the same peak in the diffractogram of the black Ru complex has a higher intensity. Lastly the peaks at 30.6° and 32.8° in the diffractogram of the orange $Ru_3(CO)_{12}$ are more intense that those in the diffractogram of the black Ru complex. These differences imply that the complexes have different crystal structures.

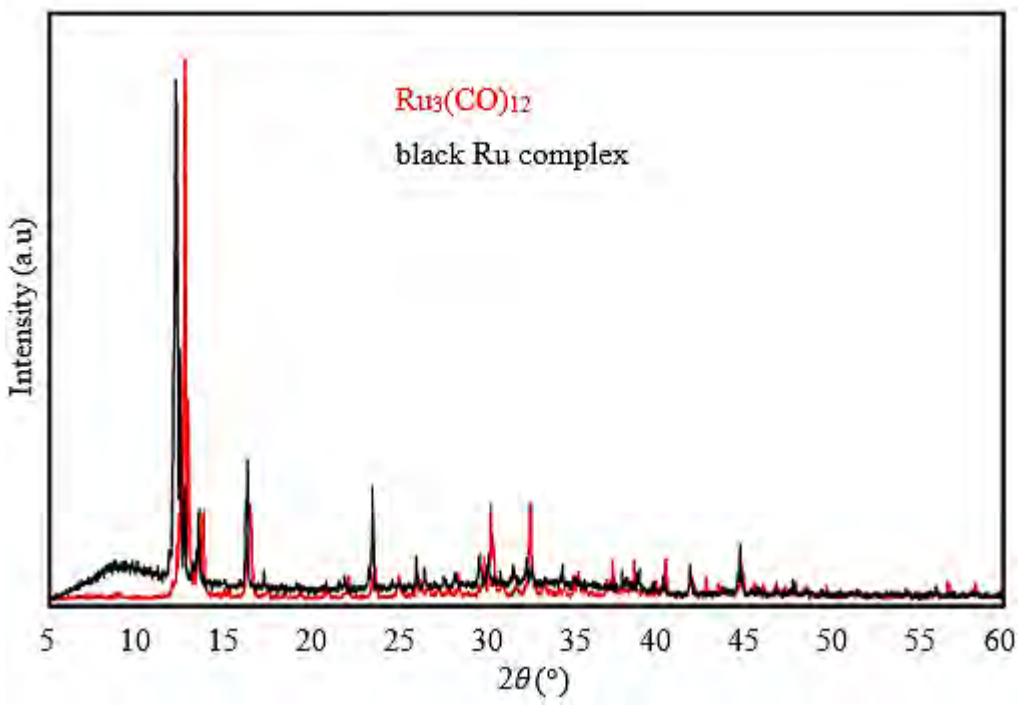

Figure 6. 12: *Merged PXRD diffractograms, illustrating the differences in the profiles between the orange and black variants of the $Ru_3(CO)_{12}$ complex*

The two complexes were further subjected to different thermal conditions and comparatively studied with different techniques; thermogravimetric analysis (TGA), differential scanning calorimetry (DSC), powder X-ray diffraction (PXRD) and Fourier transform infrared (FT-IR). The orange $Ru_3(CO)_{12}$ and black Ru complex were subjected to heat at different temperatures in the TGA isothermally and non-isothermally to study their decomposition profile.

Table 6. 2. *Possible species produced during thermal decomposition of $Ru_3(CO)_{12}$*

Species	Molecular mass (g/mol)	Ligands lost (%)
$Ru_3(CO)_{12}$	639.33	0
$Ru_3(CO)_{11}$	611.33	4
$Ru_3(CO)_{10}$	583.33	9
$Ru_3(CO)_9$	555.33	13
$Ru_3(CO)_8$	527.33	18
$Ru_3(CO)_7$	499.33	22
$Ru_3(CO)_6$	471.33	26
$Ru_3(CO)_5$	443.33	31
$Ru_3(CO)_4$	415.33	35
$Ru_3(CO)_3$	387.33	39
$Ru_3(CO)_2$	359.33	44
$Ru_3(CO)$	331.33	48
Ru_3	303.33	53

i. Isothermal analysis at 100 ℃

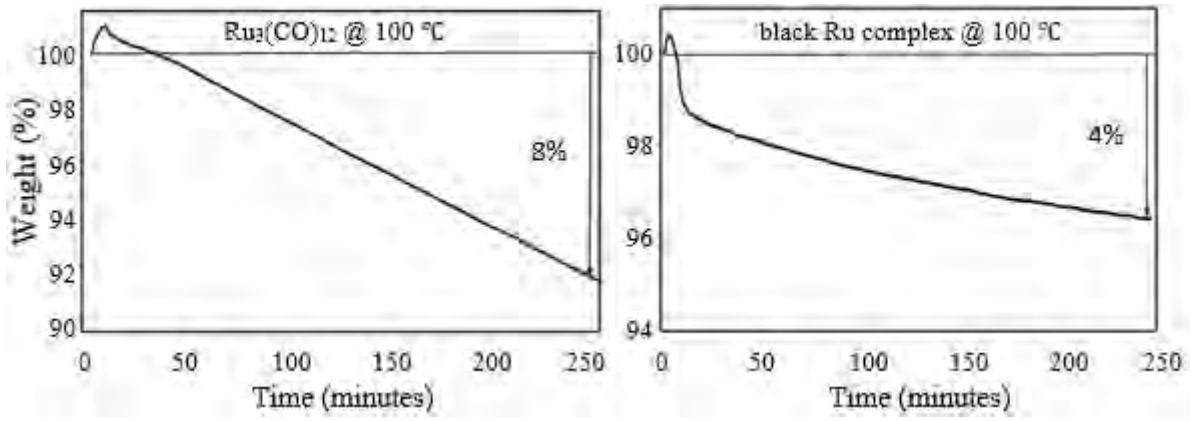

Figure 6.13: *TGA profiles of orange coloured $Ru_3(CO)_{12}$ complex (left) and the black variant obtained after thermal treatment at 100* ℃ *for 4 hours (right)*

The TGA profile of $Ru_3(CO)_{12}$ after 4 hours at 100 ° C shows 8 % mass loss corresponding to a loss of two CO groups, forming $Ru_3(CO)_{10}$. In contrast, the profile of black Ru complex after 4 hours shows 4 % mass loss corresponding to a loss of one CO ligand forming $Ru_3(CO)_9$, since the MS spectra already indicated the formation of the black variant is due to $Ru_3(CO)_{10}$.

ii. Isothermal analysis at 120 ℃

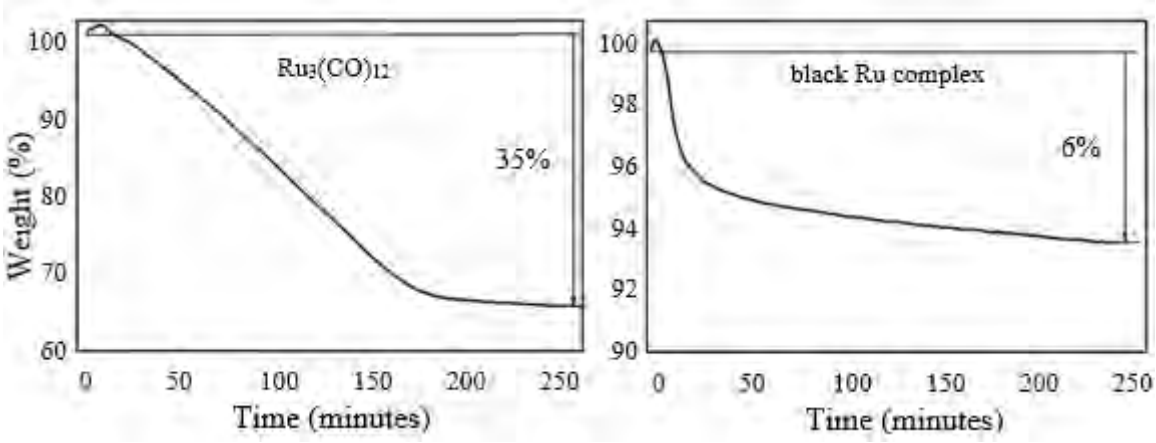

Figure 6.14: *TGA thermogram of $Ru_3(CO)_{12}$ and black Ru complex at 120℃ for 4 hours*

The TGA profile of orange $Ru_3(CO)_{12}$ after 4 hours at 120 ºC shows 35 % mass loss corresponding to a loss of eight CO ligands forming $Ru_3(CO)_4$. In contrast, the profile of black Ru complex after 4 hours shows 6 % mass loss which still corresponds to a loss of one CO ligand forming $Ru_3(CO)_9$ still in the process of losing the second CO ligand.

iii. Isothermal analysis at 150 ℃

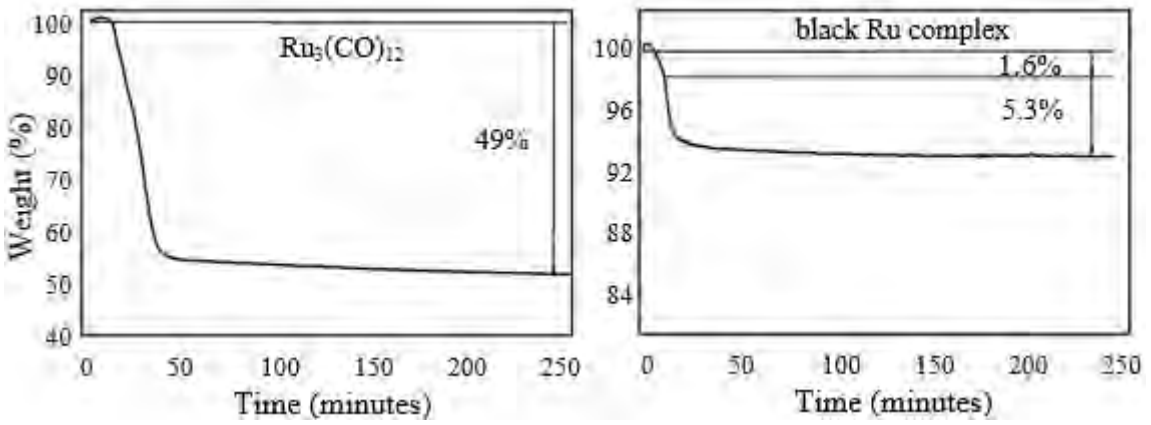

Figure 6.15: *TGA thermogram of $Ru_3(CO)_{12}$ and black Ru complex at 150 ℃ for 4 hours*

The TGA profile of orange $Ru_3(CO)_{12}$ after 4 hours at 150 ° C shows 49 % mass loss corresponding to a loss of eleven CO ligands forming $Ru_3(CO)$. In contrast, the profile of black Ru complex after 4 hours shows approximately 7 % mass loss which corresponds to a loss of about two CO ligands forming $Ru_3(CO)_8$.

The thermogram (**Figure 6.15**) shows that after 50 minutes the resulting complex becomes stable for 3 hours. These results from the mass spectroscopy of the black Ru complex obtained in the oven at 70 ° C after 3 weeks and TGA suggest that temperature ranging from 70 to 150 °C is required to form $Ru_3(CO)_8$ and is time dependent, had the orange $Ru_3(CO)_{12}$ been left longer in the oven it could have eventually formed the thermally stable $Ru_3(CO)_8$ species. Lower temperatures require more time and higher temperatures require less time, this is also suggested by the TGA thermograms at 100, 120 and 150 ° C.

iv. Non - isothermal analysis from 30 to 550 ℃

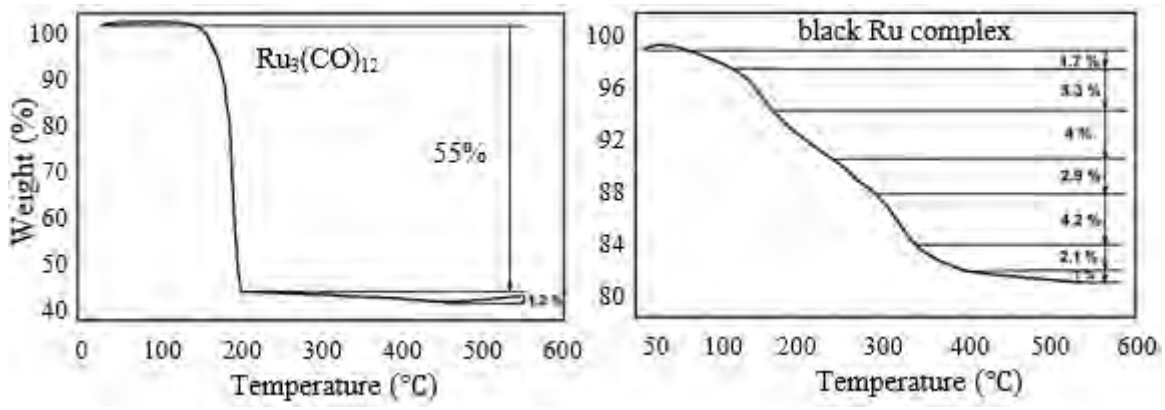

Figure 6.16: *TGA thermogram of "orange" and "black" $Ru_3(CO)_{12}$ from 30 to 550* ℃

The TGA profile of orange $Ru_3(CO)_{12}$ for the non-isothermal analysis from 30 to 550 ° C shows 55 % mass loss corresponding to a complete decomposition of the complex to Ru_3. There is also about 1 % mass gain which is not clear what could the cause of that be. The black Ru complex thermogram on the other hand shows a number of thermal events with a total mass loss of 19 % suggesting a formation of $Ru_3(CO)_6$.

There is a general trend from the TGA results which is that both the orange and black $Ru_3(CO)_{12}$ lose more CO ligands with higher temperature. Though the ligand loss happens for both, but it happens at a much lower rate for the black than the orange $Ru_3(CO)_{12}$. Interestingly,

the orange $Ru_3(CO)_{12}$ reaches complete decomposition (55 %) at 550 ^{o}C while the black $Ru_3(CO)_{12}$ only reaches 19 % mass loss. These results imply that after heating the pure $Ru_3(CO)_{12}$ at 70 ^{o}C, (most probably true for any pyrolytic temperature), and allowing it to cool down results in a more thermally stable complex but if heated constantly without allowing it to cool the process continues to happen until complete decomposition.

This stability could explain why we obtain a different compound in the second cycle of the catalyst in the reactions because after the reaction the catalyst and ionic liquid mixture is allowed to cool down to room temperature before it is reused instead of using it while it is still hot (which is challenging). Nonetheless, this may not be entirely true because dry pyrolytic conditions are different from the wet pyrolytic conditions.

Out of all the literature that we found, none except for one article reported their results beyond the first cycle of the catalyst. This literature reported that $Ru_3(CO)_{12}$ was used together with an ionic liquid to facilitate a hydroformylation reaction between CO_2, H_2 and 1-hexene. It is reported that this reaction successfully afforded the anticipated aldehyde but when the same catalyst system was recycled, an alcohol was selectively formed instead of the targeted aldehyde.[129]

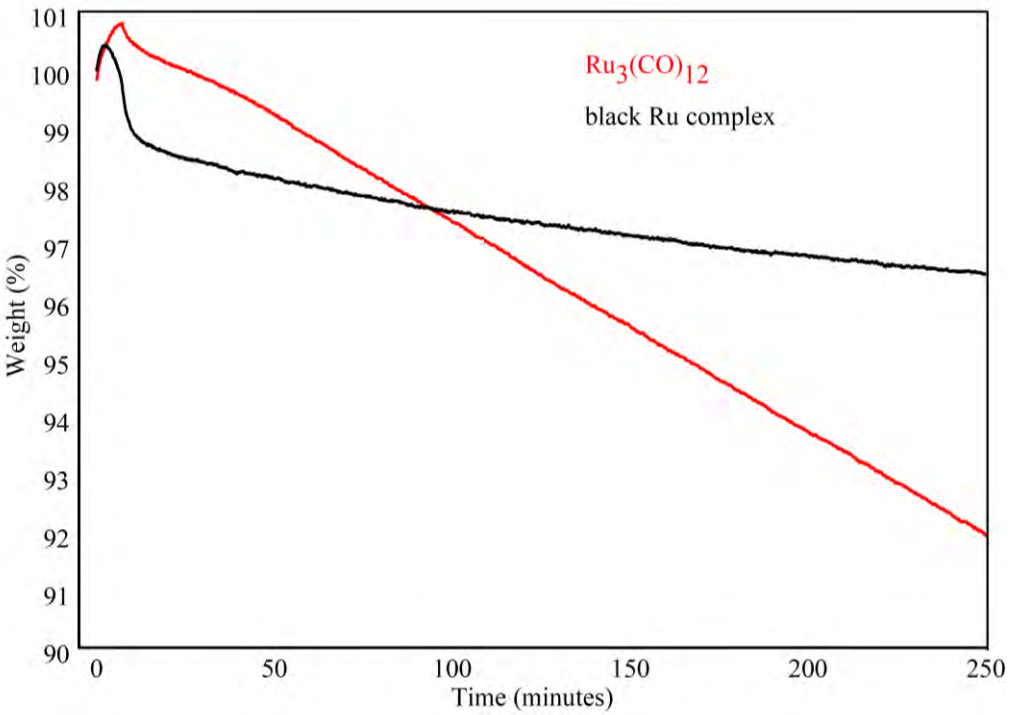

Figure 6.17: *Merged TGA thermograms of $Ru_3(CO)_{12}$ and black Ru complex at 100 ℃ for 4 hours*

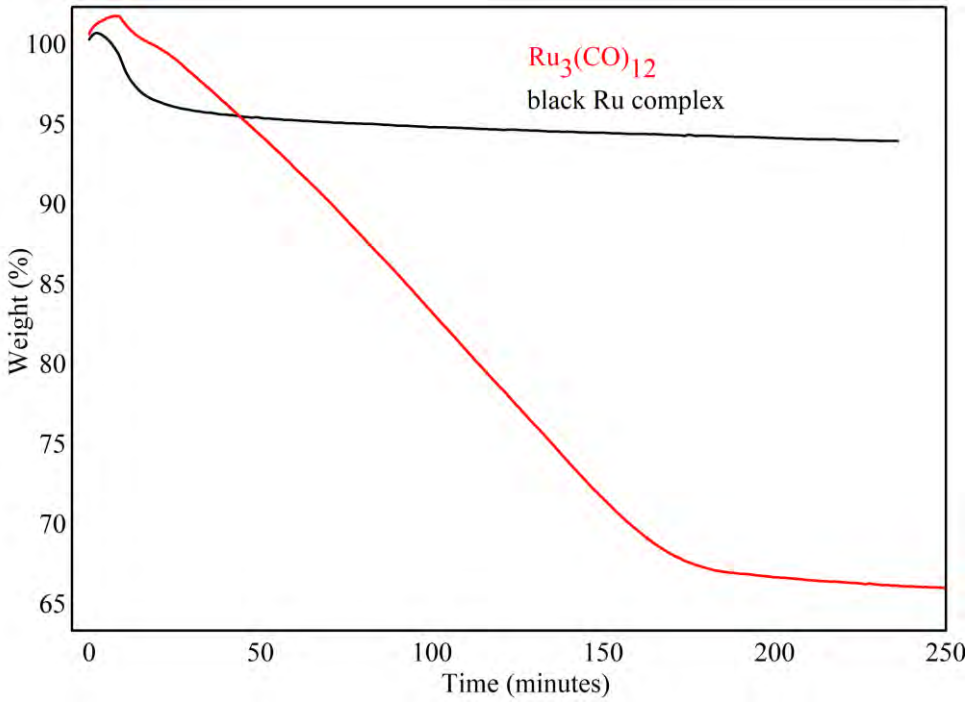

Figure 6.18: *Merged TGA thermograms of $Ru_3(CO)_{12}$ and black Ru complex formed after thermal treatment at 120 ℃ for 4 hours*

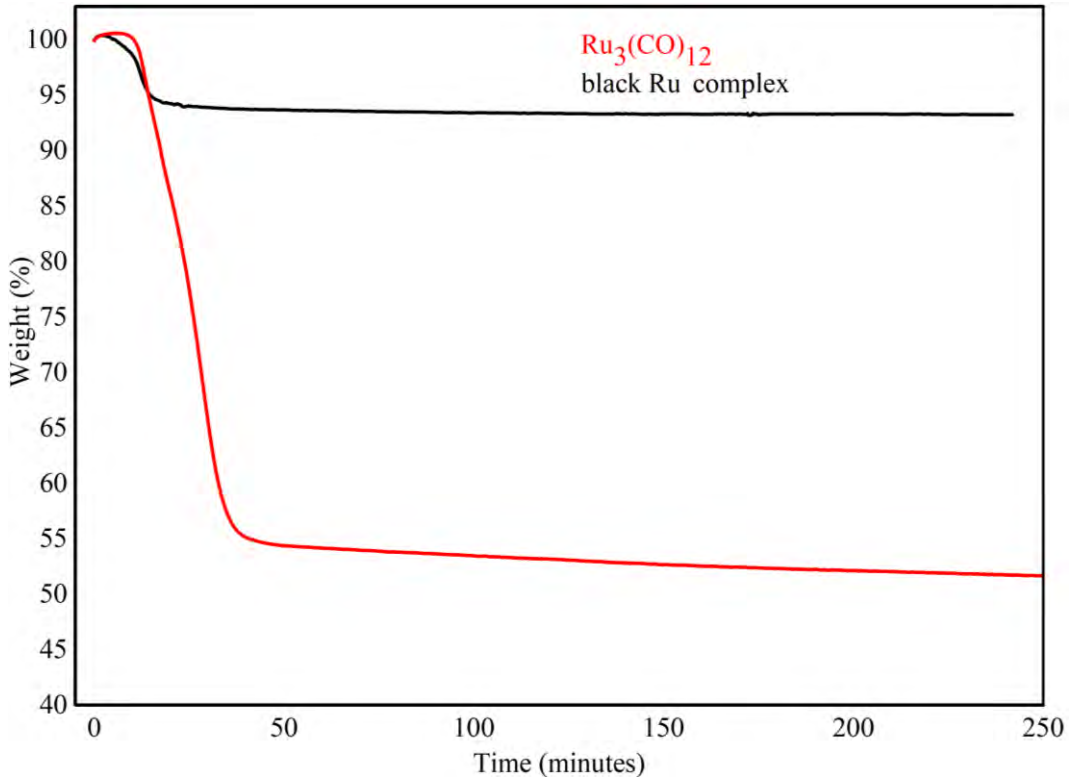

Figure 6.19: *Merged TGA thermograms of $Ru_3(CO)_{12}$ and black Ru complex at 150 ℃ for 4 hours*

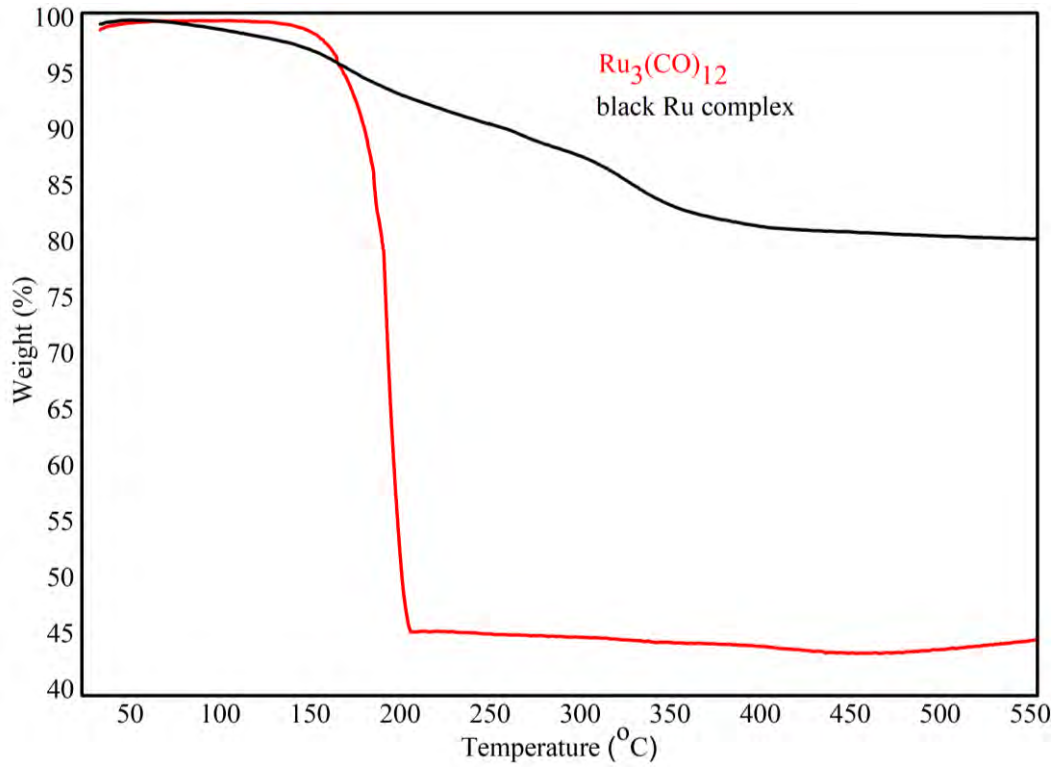

Figure 6.20: *Merged TGA thermograms of $Ru_3(CO)_{12}$ and black Ru complex from 30 to 550 ℃*

The overall trend displayed by the merged thermograms is that $Ru_3(CO)_{12}$ is less thermally stable than the black Ru complex. The slope of the decomposition profile of the $Ru_3(CO)_{12}$ is much steeper than that of black Ru complex meaning that the rate of decomposition of the orange is higher than that of the black. This is due to the difference in thermal stability of the two complexes.

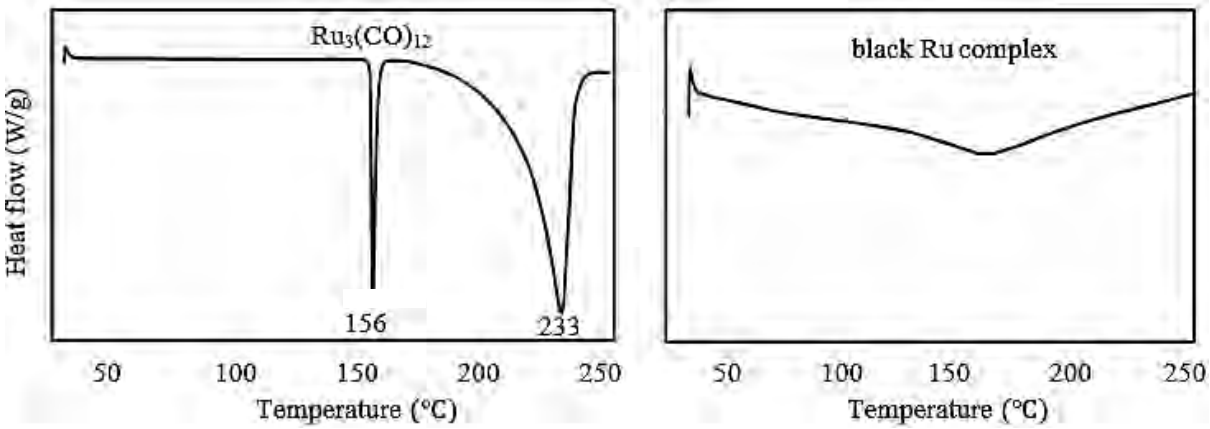

Figure 6.21: *DSC thermograms of $Ru_3(CO)_{12}$ and black Ru complex from 30 to 250 °C*

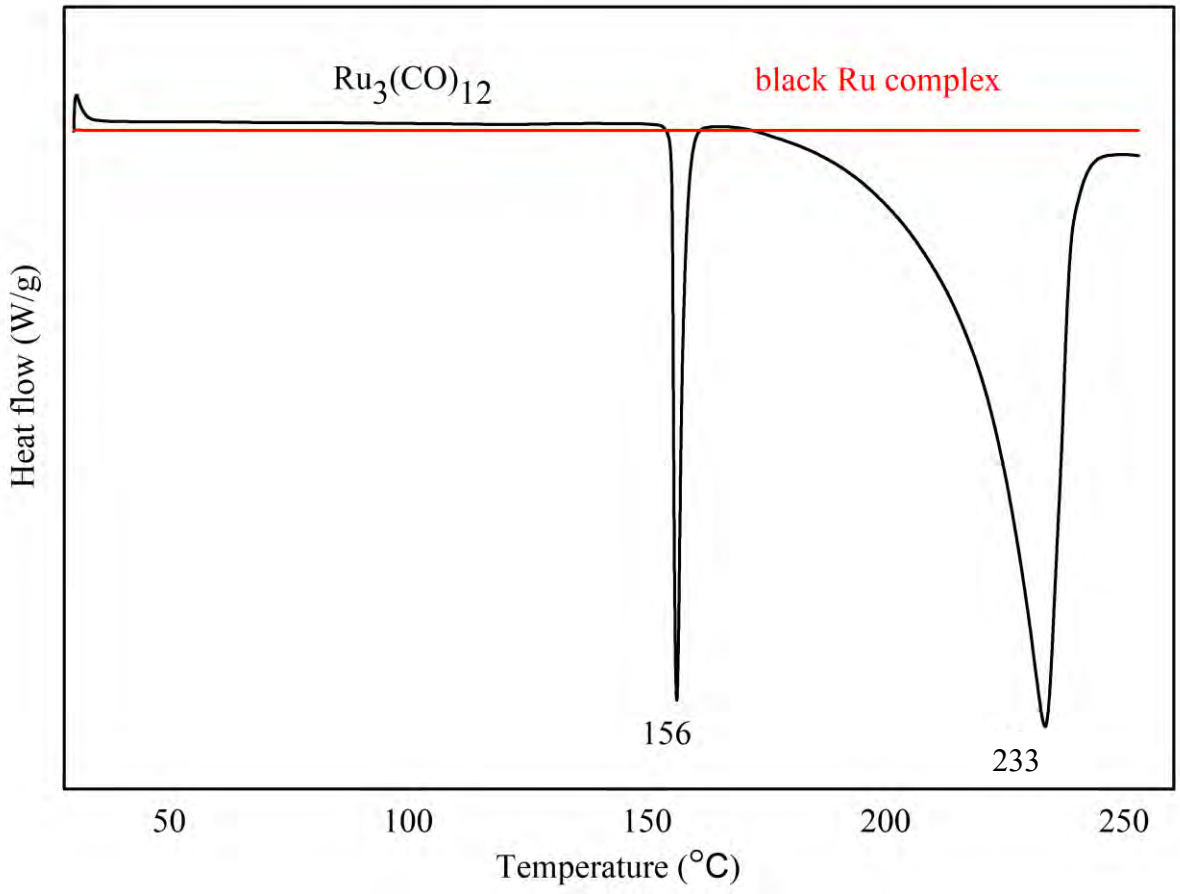

Figure 6.22: *Merged DSC thermogram of $Ru_3(CO)_{12}$ and black Ru complex from 30 to 250 °C*

The DSC thermograms (**Figure 6.21 and Figure 6.22**) highlight a clear distinction between the two forms of $Ru_3(CO)_{12}$ before and after thermal treatment. The thermogram of orange $Ru_3(CO)_{12}$ demonstrates two events occurring at 156 ℃ and 233 ℃. The first event at 156 ℃ is the melting point of the complex and the second event at 233 ℃ is the decomposition of the complex. The thermogram of the black Ru complex on the other hand does not show any thermal event within the temperature range investigated, indicating the thermal stability of this species.

The non-isothermal TGA and DSC thermogram of the orange $Ru_3(CO)_{12}$ were overlaid (**Figure 6.23**) to check if the thermal events in both thermograms correlate with each other and the conclusion is that they do correlate because the melting point on the DSC thermogram happens exactly at the start of the thermal event of the TGA thermogram followed by the decomposition of the complex.

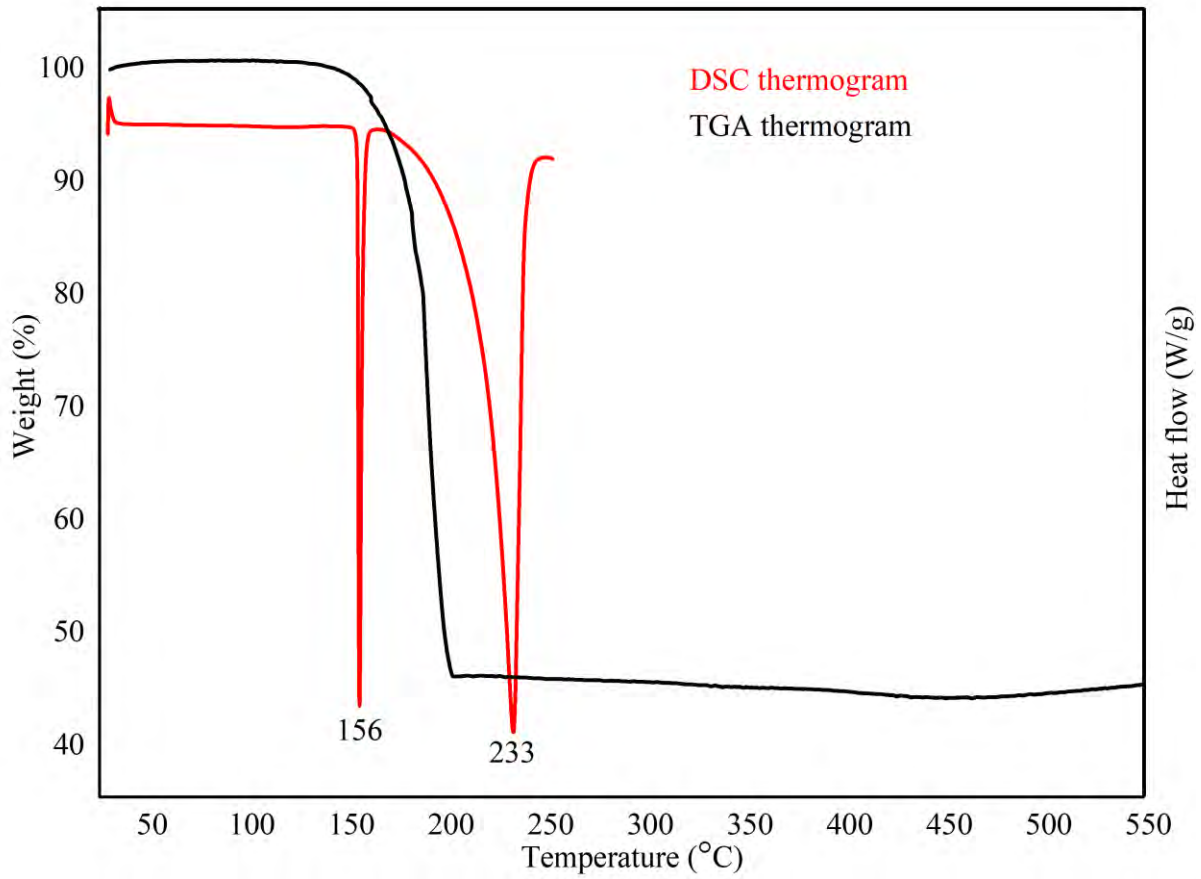

Figure 6.23: *Merged DSC (30 –250 ℃) and TGA (30 - 550 ℃) thermograms of* $Ru_3(CO)_{12}$

The orange $Ru_3(CO)_{12}$ was heated to 175 ℃ then cooled to 30 ℃ (**Figure 6.24**). This process was repeated four times, the fifth time the sample was heated all the way to 250 ℃. This analysis was performed to investigate the formation of the thermally stable species of ruthenium carbonyl obtained in the oven heated at 70 ℃ through heating and cooling which seemingly forms a stable complex having seen the TGA thermograms.

Unfortunately, the stable species did not occur because each cycle produced a melt. The reason for this could be due to the cooling cycle not being sufficient to allow the formation of a more thermally stable species. Furthermore, it was noted that the peak intensity decreases with each succeeding cycle, which could indicate that the sample becomes increasingly stable. This was deduced since it is known that the intensity of a peak represents the rate of transformation, therefore the more intense the peak the faster the transformation and less thermally stable the complex and *vice versa*. The recrystallisation temperature on the other hand kept decreasing with each cycle indicating formation of different species with each cycle.

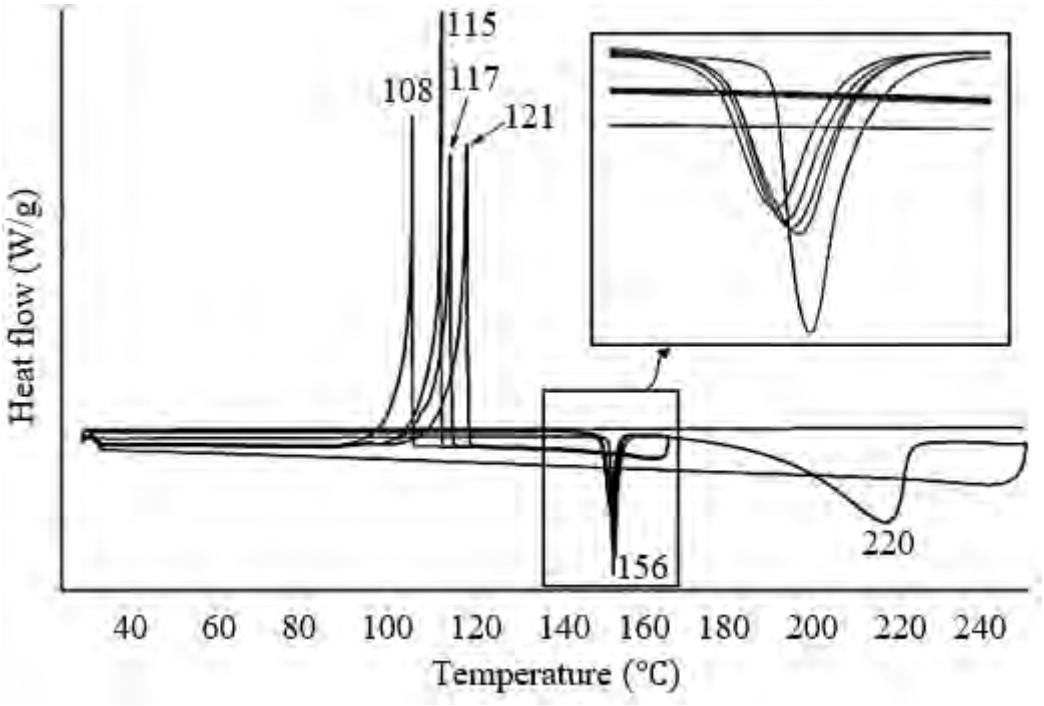

Figure 6.24: *DSC thermogram of $Ru_3(CO)_{12}$ from 30 to 250 °C after 5 cycles*

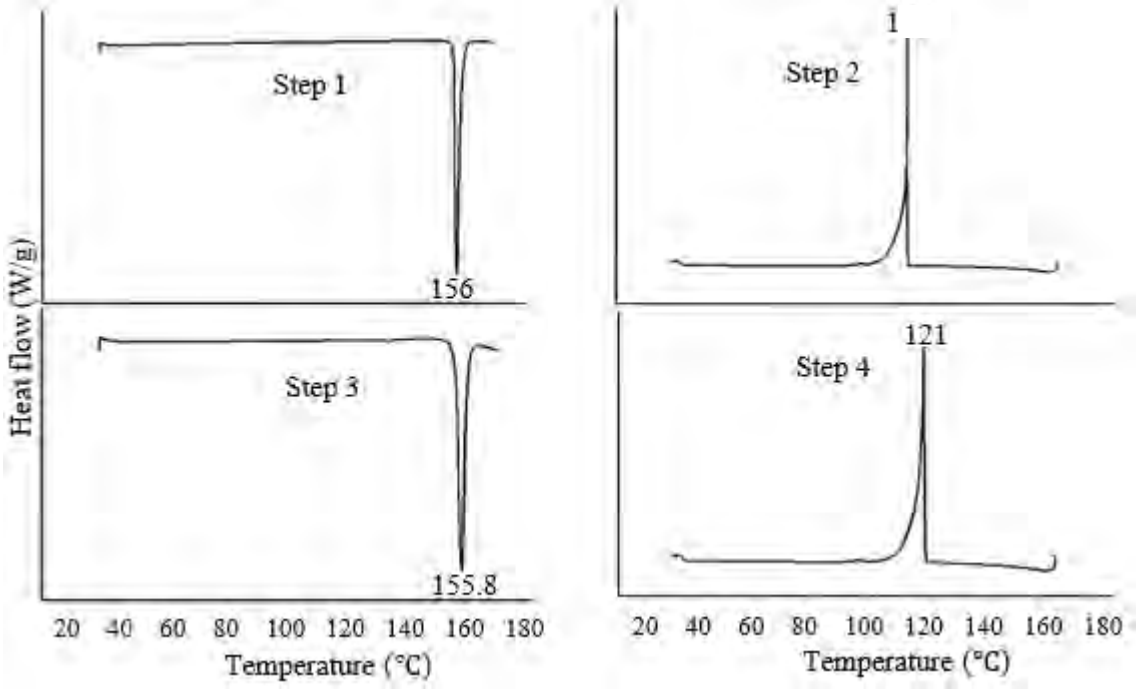

Figure 6.25: *DSC thermograms of $Ru_3(CO)_{12}$ showing each step for cycle 1 and 2*

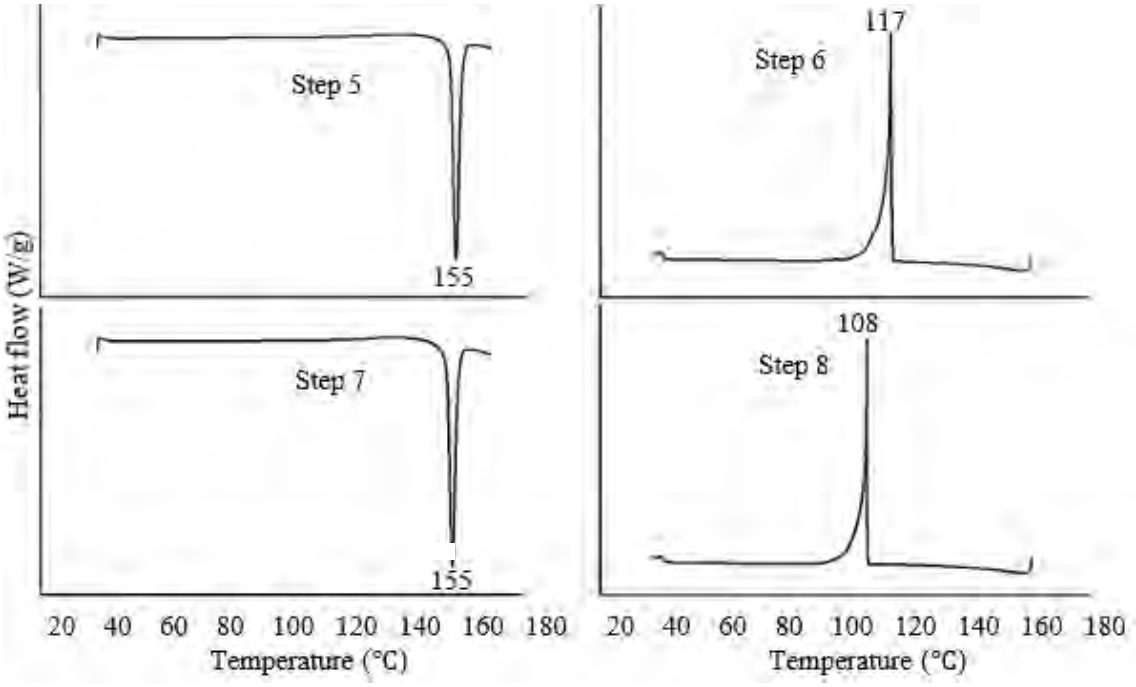

Figure 6.26: *DSC thermograms of $Ru_3(CO)_{12}$ showing each step for cycle 3 and 4*

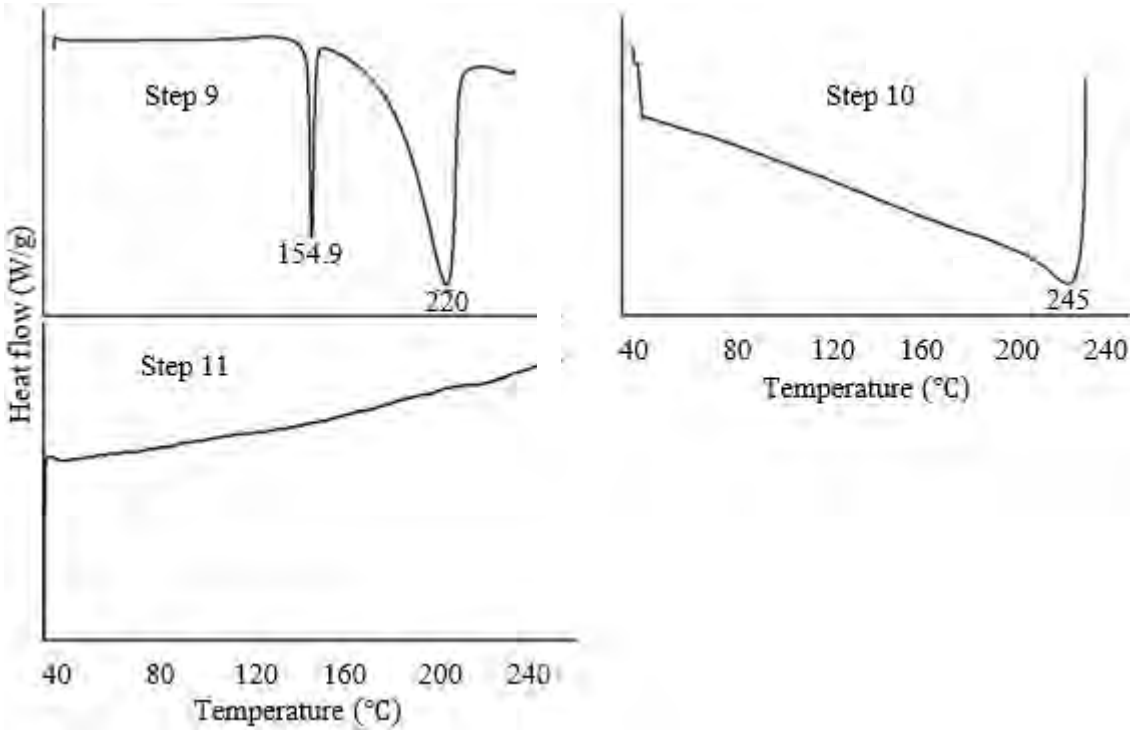

Figure 6.27: *DSC thermograms of $Ru_3(CO)_{12}$ showing each step for cycle 5*

All samples subjected to thermal analysis were analysed with ATR-FT-IR and PXRD. Surprisingly, the infra-red spectra of all samples that was heated above 100ºC was identical (**Figure 6.34**).

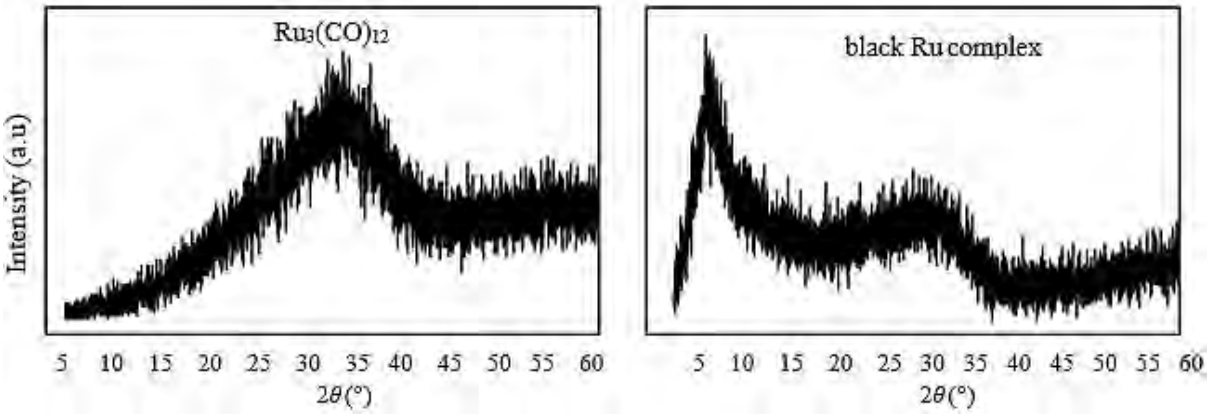

Figure 6.28: *XRD diffractograms for $Ru_3(CO)_{12}$ and black Ru complex after 100 ℃ thermal analysis*

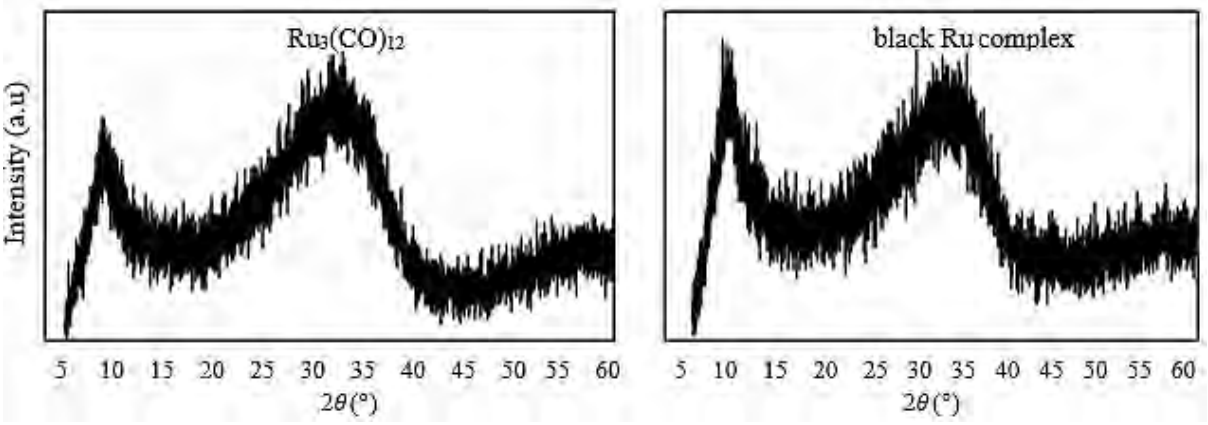

Figure 6.29: *XRD diffractograms for $Ru_3(CO)_{12}$ and black Ru complex after 120 ℃ thermal analysis*

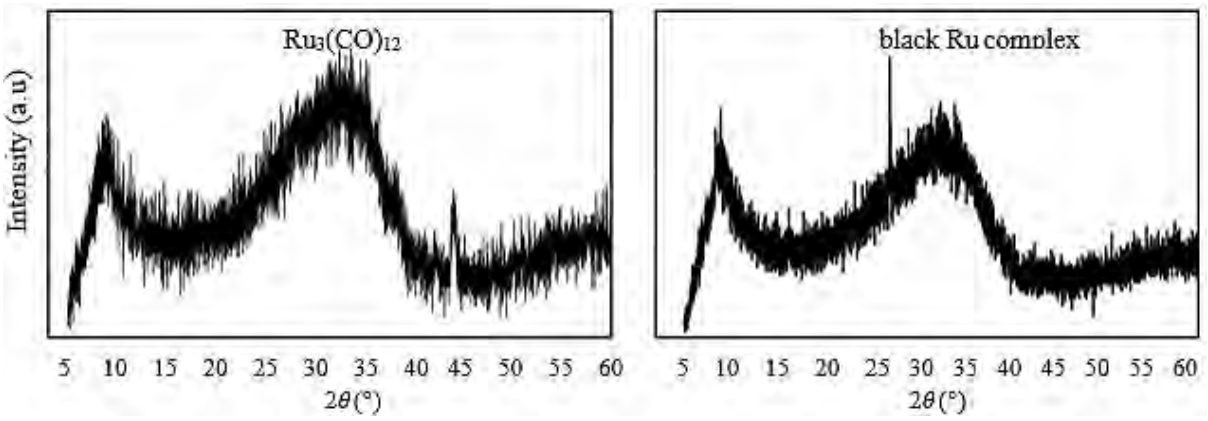

Figure 6.30: *XRD diffractograms for $Ru_3(CO)_{12}$ and black Ru complex after 150 ℃ thermal analysis*

The diffraction patterns of both orange $Ru_3(CO)_{12}$ and black Ru complex display an amorphous pattern after exposing them to temperatures of 100 ℃, 120 ℃ and 150 ℃. These results show that the two complexes undergo a similar phase change, losing its crystalline properties when heated above 100 ºC.

Thermal treatment at 150 ℃ for both samples shows an emergence of one peak on each of their diffractograms. For $Ru_3(CO)_{12}$ the peak appears at 44.3º while for the black Ru complex the peak appears at 27.2º. The peaks develop completely when both $Ru_3(CO)_{12}$ and black Ru complex are exposed to the temperature of 550 ℃. Their diffractograms (**Figure 6.31**) at this temperature are comparative to that of a metallic substance.

This results for the $Ru_3(CO)_{12}$ are in agreement with the results of the TGA thermogram at 550 ℃, where the $Ru_3(CO)_{12}$ loses all of its ligands through decomposition. The black Ru complex on the other hand did not display complete decomposition on its TGA thermogram at 550 ℃ but the diffraction pattern looks as though it is metallic and all the peaks that appear on its diffractogram also appear on the diffractogram of the $Ru_3(CO)_{12}$ which has extra peaks at 38.4º and 42º.

Interestingly, physically they both look different after being exposed to 550 ℃ (**Figure 6.33**), the sample obtained from the $Ru_3(CO)_{12}$ looks grey while that obtained from the black Ru complex is still completely black. All the other samples that were exposed to 100 ℃, 120 ℃ and 150 ℃ also look completely black like the sample exposed to 550 ℃.

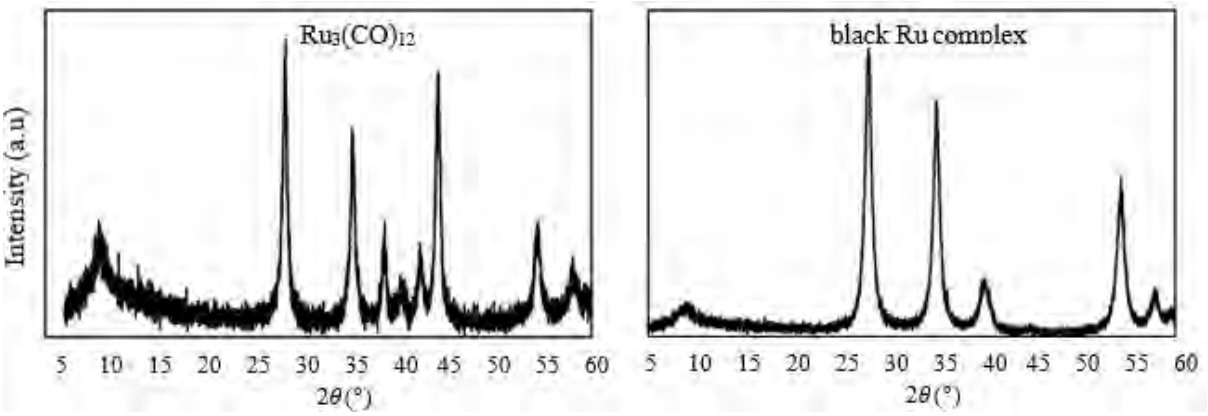

Figure 6.31: *XRD diffractograms for $Ru_3(CO)_{12}$ and black Ru complex after 550 ℃ thermal analysis*

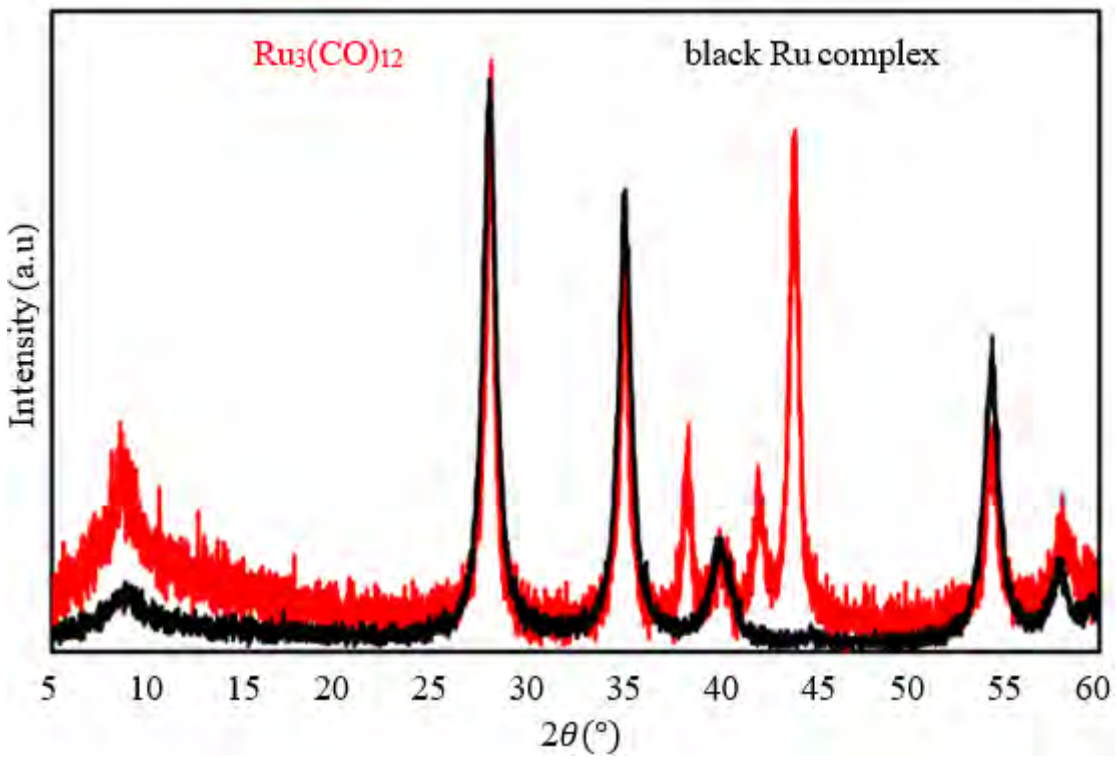

Figure 6.32: *Merged XRD diffractograms for $Ru_3(CO)_{12}$ and black Ru complex after 550 ℃ thermal analysis*

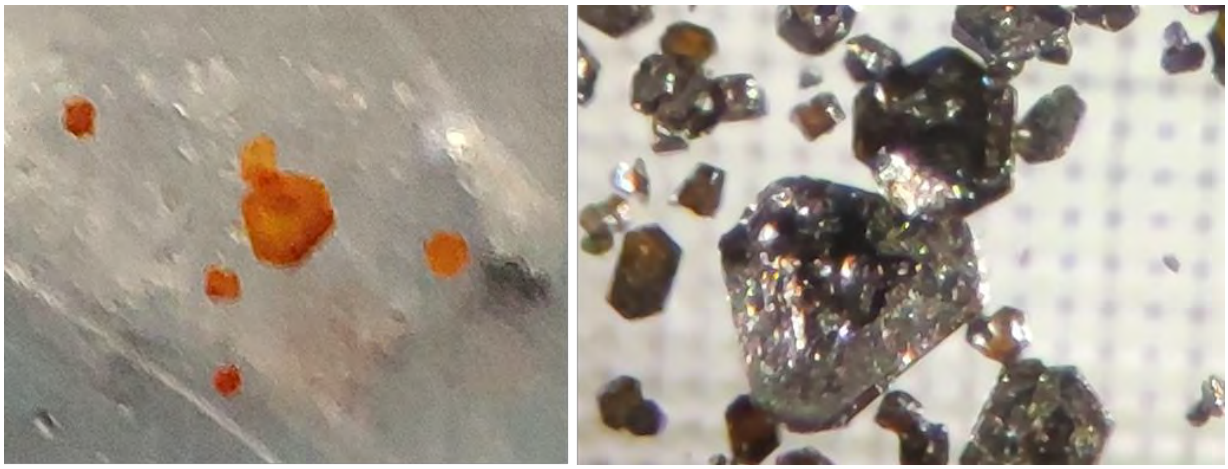

Figure 6.33: *Picture of procured $Ru_3(CO)_{12}$ (left) and (right) the black Ru complex obtained after being exposed to 550 ℃*

Since all FT-IR spectra of the $Ru_3(CO)_{12}$ samples were identical after being treated at 100 ℃ and above, only one example of the resultant spectra is shown (**Figure 6.34**). The IR spectra of all the samples after TGA analysis does not display carbonyl bands nor the metal-carbon bands that were observed prior to being exposed to the thermal conditions in the TGA analyses. The complete characterization of these samples is still ongoing, especially considering the strong

evidence that the $Ru_3(CO)_{12}$ complex might not actually be the (only) catalytic species present in most of the reactions documented in literature.

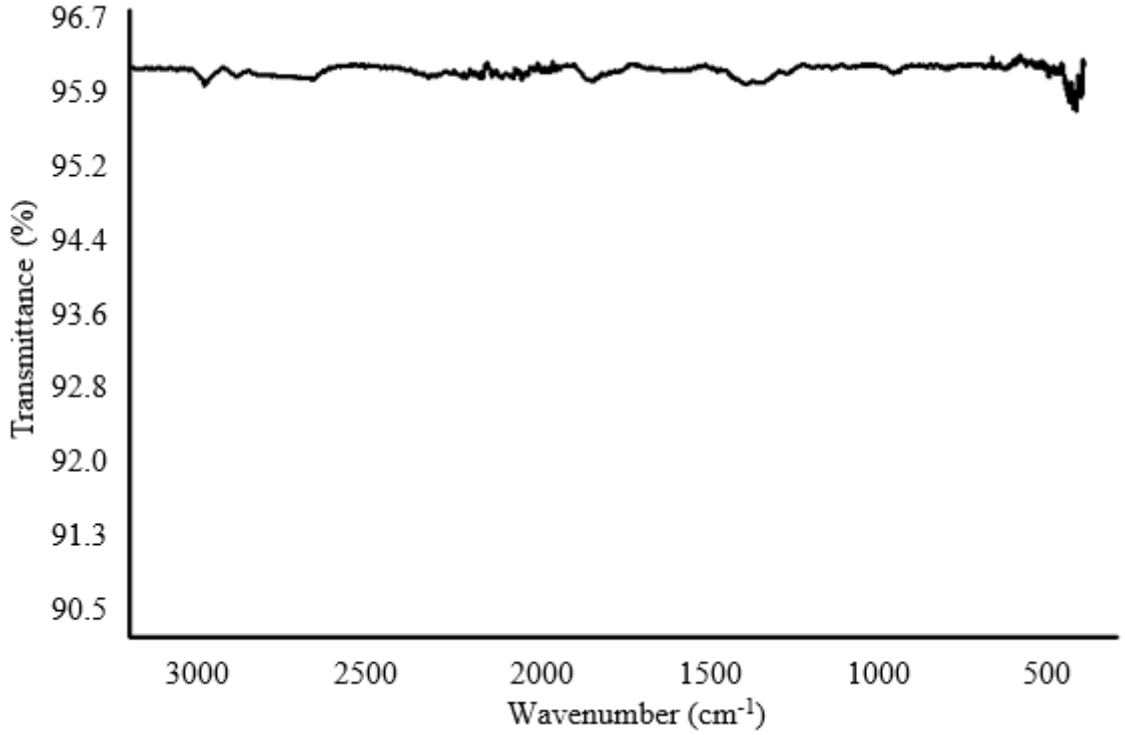

Figure 6.34: *IR spectrum of black Ru complexes after 100, 120, 150 to 550 ℃ thermal analysis*

6.3. Conclusion

A comprehensive literature review was conducted on $Ru_3(CO)_{12}$ about its use in catalytic reactions to understand its role in the reactions. Additionally, an investigation was undertaken on the kind of transformations that the catalyst undergoes when exposed to heat. This investigation was carried out with the hopes of finding the structures that could be resulting from $Ru_3(CO)_{12}$ during the reaction and their significance to it. The orange $Ru_3(CO)_{12}$ that was exposed to the oven temperature of 70 ℃ for 3 weeks, turned black, “black Ru complex”.

The orange and black Ru complexes were characterized utilizing DSC, TGA, ATR-FT-IR and PXRD. Results obtained from DSC and TGA suggest that the catalyst transforms to different species at different temperatures. They also demonstrated that black Ru complex become more thermally stable when allow to cool. Orange Ru complex undergoes a continuous transformation rapidly when not allowed to cool. ATR-FT-IR showed that $Ru_3(CO)_{12}$ loses its symmetry when heat is applied to it indicating a transformation. PXRD confirmed this observation by showing that $Ru_3(CO)_{12}$ becomes amorphous with heat exposure indicating the

transformation. Nonetheless, the results don’t indicate which specie/s are present during the reaction therefore results are inconclusive.

7. Concluding remarks

The study has presented a successful conversion of carbon dioxide (CO_2) through homogenous catalysis. This success gives an indication that the utilization of CO_2 in organic synthesis offers a promising role in the reduction of its emissions. In addition to other ways to mitigate the effects of this greenhouse gas on climate change, our results show that committed use of CO_2 in organic synthesis can help achieve net-zero emissions.

The central focus of the study revolved around exploring the viability of utilizing CO_2 as a C1 synthon in conjunction with cyclohexene, water, or methanol to synthesize the corresponding carboxylic acids and/or esters. The objective was to achieve this transformation with the assistance of transition metal catalysts, aimed at overcoming the inherent thermodynamic stability of CO_2. The study was bifurcated into two distinct sections of catalysis: heterogeneous and homogeneous catalysis.

In the heterogeneous catalysis section, various catalysts including Au/TiO_2, Fe/TiO_2, Ni/TiO_2, and Ru/TiO_2 were synthesized using the wet impregnation method. The resulting catalysts underwent comprehensive characterization utilizing solid-state UV-VIS, TEM, EDX, BET, and PXRD techniques. Subsequently, these catalysts were applied in a reaction alongside cyclohexene, water, and CO_2 at a temperature of 150 °C. However, the anticipated product, carboxylic acid, was not obtained. Instead, oxidation products, including cyclohexanone, cyclohexenone, and cyclohexane diol, were observed for Au/TiO_2, Fe/TiO_2, and Ni/TiO_2 catalysts, while Ru/TiO_2 catalysed a hydrogenation reaction yielding cyclohexane. Despite raising the temperature to 200 °C in an attempt to promote product formation, all catalysts were poisoned during the reaction, and the desired product remained elusive.

In the second approach, a reaction involving cyclohexene, methanol, and CO_2 (initially in gaseous form, followed by solid) was conducted in the presence of an ionic liquid, $[BMIM]^+Cl^-$, as an additive, and $Ru_3(CO)_{12}$ as a catalyst. The ionic liquid ($[BMIM]^+Cl^-$) was successfully synthesized and characterized *via* ^1H NMR and ATR-FT-IR techniques, while the catalyst was utilized as obtained from the supplier. The reaction yielded the expected ester, methyl cyclohexanoate, with a 27% yield when performing the reaction under a CO_2 atmosphere and an 87% yield when the reaction solution is saturated with solid CO_2. This outcome suggests that solid CO_2 readily absorbs into the reaction media, rendering the reaction more efficient compared to the gaseous counterpart.

To elucidate the mechanism of this reaction, the initial reaction mixture of the catalyst and non-volatile ionic liquid was reutilized in the same reaction with fresh reactants. However, the desired product was not obtained, potentially attributed to a colour change observed in the catalyst from orange to black during the reaction, indicating either a chemical or physical change. Further investigation and literature review were conducted on the catalyst alone to ascertain if it functions as a catalyst or participates in the reaction. Additionally, heat was applied to the catalyst to explore the transformations it undergoes in hopes of elucidating the resulting structures and their correlation with the reaction. Unfortunately, inconclusive results were obtained due to a lack of appropriate experimental setup and insufficient literature reporting on obvious colour changes or turnover numbers.

In terms of future prospects, while intriguing results were obtained in the second approach of the reaction, there remains a need to comprehensively understand the mechanism involved. Questions regarding the catalyst-induced colour change, its absence in literature, and the role of the ionic liquid warrant further investigation through meticulously designed experiments utilizing appropriate equipment and analytical techniques. These endeavours will pave the way for a deeper understanding of the reaction mechanism and potential applications in the future.

References

(1) Goel, S.; Agarwal, D. Carbon Dioxide. In *Encyclopedia of Toxicology (Third Edition)*; Wexler, P., Ed.; Academic Press: Oxford, **2014**; pp 675–677. https://doi.org/10.1016/B978-0-12-386454-3.00269-4.

(2) Carbon Dioxide | Atmospheric Science Education Tools. *UCAR Center for Science Education*.https://scied.ucar.edu/learning-zone/how-climate-works/carbon-dioxide (accessed 2021-07-07).

(3) Solomon, S. Climate Change: The Physical Science Basis, Contribution of Working Group I to the Fourth Assessment Report of the Intergovernmental Panel on Climate Change. *Intergovernmental Panel on Climate Change, Intergovernmental Panel on Climate Change, Eds*. Cambridge University Press: Cambridge ; New York, **2007**.

(4) Sabine, C. L.; Feely, R. A. Carbon dioxide. In *Encyclopedia of Atmospheric Sciences*; Holton, J. R., Ed.; Academic Press: Oxford, **2003**; pp 335–343. https://doi.org/10.1016/B0-12-227090-8/00095-6.

(5) Huang, K.; Sun, C.-L.; Shi, Z.-J. Transition-Metal-Catalyzed C–C Bond Formation through the Fixation of Carbon Dioxide. *Chem. Soc. Rev.* **2011**, *40* (5), 2435. https://doi.org/10.1039/c0cs00129e.

(6) Ritchie, H.; Roser, M. CO_2 and Greenhouse Gas Emissions. *Our World Data* **2020**.

(7) Porosoff, M. D.; Yan, B.; Chen, J. G. Catalytic Reduction of CO_2 by H_2 for Synthesis of CO, Methanol and Hydrocarbons: Challenges and Opportunities. *Energy Environ. Sci.* **2016**, *9* (1), 62–73. https://doi.org/10.1039/C5EE02657A.

(8) Otto, A.; Grube, T.; Schiebahn, S.; Stolten, D. Closing the Loop: Captured CO_2 as a Feedstock in the Chemical Industry. *Energy Environ. Sci.* **2015**, *8* (11), 3283–3297. https://doi.org/10.1039/C5EE02591E.

(9) Grignard, B.; Gennen, S.; Jérôme, C.; Kleij, A. W.; Detrembleur, C. Advances in the Use of CO_2 as a Renewable Feedstock for the Synthesis of Polymers. *Chem. Soc. Rev.* **2019**, *48* (16), 4466–4514. https://doi.org/10.1039/C9CS00047J.

(10) Seibicke, M.; Siebert, M.; Siegle, A. F.; Gutenthaler, S. M.; Trapp, O. Application of Hetero-Triphos Ligands in the Selective Ruthenium-Catalyzed Transformation of Carbon Dioxide to the Formaldehyde Oxidation State. *Organometallics* **2019**, *38* (8), 1809–1814. https://doi.org/10.1021/acs.organomet.9b00107.

(11) Liu, Q.; Wu, L.; Jackstell, R.; Beller, M. Using Carbon Dioxide as a Building Block in Organic Synthesis. *Nat. Commun.* **2015**, *6* (1), 5933. https://doi.org/10.1038/ncomms6933.

(12) Chen, Y.; Mu, T. Conversion of CO_2 to Value-Added Products Mediated by Ionic Liquids. *Green Chem.* **2019**, *21* (10), 2544–2574. https://doi.org/10.1039/C9GC00827F.

(13) SciencesRoundtable, N. R. C. (US) C. Carbon Dioxide as a Feedstock. *National Academies Press (US)*. **2001**.

(14) Arakawa, H.; Aresta, M.; Armor, J. N.; Barteau, M. A.; Beckman, E. J.; Bell, A. T.; Bercaw, J. E.; Creutz, C.; Dinjus, E.; Dixon, D. A.; Domen, K.; DuBois, D. L.; Eckert, J.; Fujita, E.; Gibson, D. H.; Goddard, W. A.; Goodman, D. W.; Keller, J.; Kubas, G. J.; Kung, H. H.; Lyons, J. E.; Manzer, L. E.; Marks, T. J.; Morokuma, K.; Nicholas, K. M.; Periana, R.; Que, L.; Rostrup-Nielson, J.; Sachtler, W. M. H.; Schmidt, L. D.; Sen, A.; Somorjai, G. A.; Stair, P. C.; Stults, B. R.; Tumas, W. Catalysis Research of Relevance to Carbon Management: Progress, Challenges, and Opportunities. *Chem. Rev.* **2001**, *101* (4), 953–996. https://doi.org/10.1021/cr000018s.

(15) Sáenz-Galindo, A.; López-López, L. I.; Cruz-Duran, F. N. de la; Castañeda-Facio, A. O.; Rámirez-Mendoza, L. A.; Córdova-Cisneros, K. C.; Loera-Carrera, D. de. Applications of Carboxylic Acids in Organic Synthesis, Nanotechnology and Polymers. *In Carboxylic Acid - Key Role in Life Sciences*; *Badea, G. I., Radu, G. L., Eds.; InTech*, **2018**. https://doi.org/10.5772/intechopen.74654.

(16) Badea, G. I.; Radu, G. L. Introductory Chapter: Carboxylic Acids - Key Role in Life Sciences. *In Carboxylic Acid - Key Role in Life Sciences; Badea, G. I., Radu, G. L., Eds.; InTech*, **2018**. https://doi.org/10.5772/intechopen.77021.

(17) Mittal, R.; Kumar, A.; Awasthi, S. K. Practical Scale up Synthesis of Carboxylic Acids and Their Bioisosteres 5-Substituted-1 *H* -Tetrazoles Catalyzed by a Graphene Oxide-Based Solid Acid Carbocatalyst. *RSC Adv.* **2021**, *11* (19), 11166–11176. https://doi.org/10.1039/D1RA01053K.

(18) Anuar Sharuddin, S. D.; Abnisa, F.; Wan Daud, W. M. A.; Aroua, M. K. A Review on Pyrolysis of Plastic Wastes. *Energy Convers. Manag.* **2016**, *115*, 308–326. https://doi.org/10.1016/j.enconman.2016.02.037.

(19) Davarnejad, R.; Azizi, J.; Bahari, S. A Look at the Industrial Production of Olefins Based on Naphtha Feed: A Process Study of a Petrochemical Unit. *In Alkenes - Recent Advances, New Perspectives and Applications*; *Davarnejad, R., Ed.; IntechOpen,* **2021**. https://doi.org/10.5772/intechopen.100017.

(20) Wu, X.-F.; Zheng, F. Synthesis of Carboxylic Acids and Esters from CO_2. *Top. Curr. Chem.* **2017**, *375* (1), 4. https://doi.org/10.1007/s41061-016-0091-6.

(21) Ostapowicz, T. G.; Schmitz, M.; Krystof, M.; Klankermayer, J.; Leitner, W. Carbon Dioxide as a C_1 Building Block for the Formation of Carboxylic Acids by Formal Catalytic Hydrocarboxylation. *Angew. Chem.* **2013**, *125* (46), 12341–12345. https://doi.org/10.1002/ange.201304529.

(22) Graham, D. C.; Mitchell, C.; Bruce, M. I.; Metha, G. F.; Bowie, J. H.; Buntine, M. A. Production of Acrylic Acid through Nickel-Mediated Coupling of Ethylene and Carbon Dioxide—A DFT Study. *Organometallics* **2007**, *26* (27), 6784–6792. https://doi.org/10.1021/om700592w.

(23) Chatterjee, R.; Bhaumik, A. Carboxylation of Alkenes and Alkynes Using CO_2 as a Reagent: An Overview. *COC* **2022**, *26* (1), 60–70. https://doi.org/10.2174/1385272825666211206090621.

(24) Ester | Description, Types, & Reactions | *Britannica*. https://www.britannica.com/science/ester-chemical-compound (accessed 2023-02-23).

(25) Liu, M.; Zhang, Z.; Liu, H.; Xie, Z.; Mei, Q.; Han, B. Transformation of Alcohols to Esters Promoted by Hydrogen Bonds Using Oxygen as the Oxidant under Metal-Free Conditions. *Sci. Adv.* **2018**, *4* (10), eaas9319. https://doi.org/10.1126/sciadv.aas9319.

(26) Wu, L.; Liu, Q.; Jackstell, R.; Beller, M. Carbonylations of Alkenes with CO Surrogates. *Angew. Chem. Int. Ed.* **2014**, *53* (25), 6310–6320. https://doi.org/10.1002/anie.201400793.

(27) Wu, L.; Liu, Q.; Fleischer, I.; Jackstell, R.; Beller, M. Ruthenium-Catalysed Alkoxycarbonylation of Alkenes with Carbon Dioxide. *Nat. Commun.* **2014**, *5* (1), 3091. https://doi.org/10.1038/ncomms4091.

(28) Alcantara, M. L.; Pacheco, K. A.; Bresciani, A. E.; Brito Alves, R. M. Thermodynamic Analysis of Carbon Dioxide Conversion Reactions. Case Studies: Formic Acid and Acetic Acid Synthesis. *Ind. Eng. Chem. Res.* **2021**, *60* (25), 9246–9258. https://doi.org/10.1021/acs.iecr.1c00989.

(29) Aresta, M. Carbon Dioxide as Chemical Feedstock. *Wiley-VCH: Weinheim*. **2010**.

(30) Wang, L.; Chen, W.; Zhang, D.; Du, Y.; Amal, R.; Qiao, S.; Wu, J.; Yin, Z. Surface Strategies for Catalytic CO $_2$ Reduction: From Two-Dimensional Materials to Nanoclusters to Single Atoms. *Chem. Soc. Rev.* **2019**, *48* (21), 5310–5349. https://doi.org/10.1039/C9CS00163H.

(31) Carbon Management: Implications for R & D in the Chemical Sciences and Technology (A Workshop Report to the Chemical Sciences Roundtable); *National Academies Press: Washington, D.C.* **2001**; p 10153. https://doi.org/10.17226/10153.

(32) Mohammed, S. A. S.; Yahya, W. Z. N.; Bustam, M. A.; Kibria, M. G. Elucidation of the Roles of Ionic Liquid in CO_2 Electrochemical Reduction to Value-Added Chemicals and Fuels. *Molecules* **2021**, *26* (22), 6962. https://doi.org/10.3390/molecules26226962.

(33) Seo, H.; Nguyen, L. V.; Jamison, T. F. Using Carbon Dioxide as a Building Block in Continuous Flow Synthesis. *Adv. Synth. Catal.* **2019**, *361* (2), 247–264. https://doi.org/10.1002/adsc.201801228.

(34) Juliá-Hernández F, Gaydou M, Serrano E, van Gemmeren M, Martin R. Ni- and Fe-catalyzed Carboxylation of Unsaturated Hydrocarbons with CO_2. *Top Curr Chem (Cham)*. **2016,** *374*(4), 45. doi:10.1007/s41061-016-0045-z.

(35) Li, Y.; Cui, X.; Dong, K.; Junge, K.; Beller, M. Utilization of CO_2 as a C1 Building Block for Catalytic Methylation Reactions. *ACS Catal.* **2017**, *7* (2), 1077–1086. https://doi.org/10.1021/acscatal.6b02715.

(36) Viswanathan, B. Reflections on the Electrochemical Reduction of Carbon Dioxide on Metallic Surfaces. *Indian Journal of Chemistry*. **2012**, 51

(37) Alvarez, Rafael; Carmona, Ernesto; Poveda, Manuel L.; Sanchez-Delgado, Roberto. Carbon Dioxide Chemistry. The Synthesis and Properties of Trans-Bis(Carbon Dioxide)Tetrakis(Trimethylphosphine)Molybdenum (Trans-[$Mo(CO_2)_2(PMe_3)_4$]) the First Stable Bis(Carbon Dioxide) Adduct of a Transition Metal. *Journal of the American Chemical Society*. **1984**, 106(9), 2731–2732. Doi10.1021ja00321a060.

(38) Bristow, G. S.; Hitchcock, P. B.; Lappert, M. F. A Novel Carbon Dioxide Complex: Synthesis and Crystal Structure of [$Nb(\eta\text{-}C_5H_4Me)_2(CH_2SiMe_3)(H_2\text{-}CO_2)$]. *J. Chem. Soc., Chem. Commun.* **1981**, 21, 1145–1146. https://doi.org/10.1039/C39810001145.

(39) Sakamoto, M.; Shimizu, I.; Yamamoto, A. Synthesis of the First Carbon Dioxide Coordinated Palladium(0) Complex, Pd(.Eta.$_2$-CO_2)($PMePh_2$)$_2$. *Organometallics* **1994,** *13* (2), 407-409. https://doi.org/10.1021/om00014a003.

(40) Gong, J. K.; Wright, C. A.; Thorn, M.; McCauley, K.; McGill, J. W.; Sutterer, A.; Hinze, S. M.; Prince, R. B. From Carbon Dioxide to C_2 Organic Molecules Mediated by Aresta's Nickel Carbon Dioxide Complex. In *Studies in Surface Science and Catalysis*; *Elsevier*, **1998**, 114, 491–494. https://doi.org/10.1016/S0167-2991(98)80803-3.

(41) Aresta, M.; Dibenedetto, A.; Quaranta, E. CO_2 Coordination to Metal Centres: Modes of Bonding and Reactivity. In *Reaction Mechanisms in Carbon Dioxide Conversion*; Springer Berlin Heidelberg: Berlin, Heidelberg, **2016**, 35–69. https://doi.org/10.1007/978-3-662-46831-9_2.

(42) Stagg-Williams, Susan, Fábio Bellot Noronha, Gene Fendley and Daniel E. Resasco. "CO2 Reforming of CH4 over Pt/ZrO2 Catalysts Promoted with La and Ce Oxides." *Journal of Catalysis* **2000**,194: 240-249.

(43) Dumesic, J. A.; Huber, G. W.; Boudart, M. Principles of Heterogeneous Catalysis. In *Handbook of Heterogeneous Catalysis*; John Wiley & Sons, Ltd, **2008**. https://doi.org/10.1002/9783527610044.hetcat0001.

(44) *Adsorption Theory of Heterogeneous Catalysis*. VEDANTU. https://www.vedantu.com/chemistry/adsorption-theory-heterogeneous-catalyst, https://www.vedantu.com/chemistry/adsorption-theory-heterogeneous-catalyst (accessed 2023-06-27).

(45) *Heterogeneous Catalysis in Organic Chemistry*. dokumen.tips. https://dokumen.tips/documents/heterogeneous-catalysis-in-organic-chemistry.html (accessed 2023-06-27).

(46) Gulumian, M.; Andraos, C.; Afantitis, A.; Puzyn, T.; Coville, N. J. Importance of Surface Topography in Both Biological Activity and Catalysis of Nanomaterials: Can Catalysis by Design Guide Safe by Design? *Int. J. Mol. Sci.* **2021**, *22* (15), 8347. https://doi.org/10.3390/ijms22158347.

(47) *Principles of Heterogeneous Catalysis - Dumesic - Major Reference Works - Wiley Online Library*. https://onlinelibrary.wiley.com/doi/full/10.1002/9783527610044.hetcat0001 (accessed 2023-06-27).

(48) Gerard V. Smith & Ferenc Notheisz. Heterogeneous Catalysis in Organic Chemistry. Academic Press; San Diego, CA. *J.Am. Chem. Soc.* **2000**, *122* (21), 5233-5234. https://doi.org/10.1021/ja995775q

(49) Hutchings, G. J.; Védrine, J. C. Heterogeneous Catalyst Preparation. In *Basic Principles in Applied Catalysis*; Baerns, M., Ed.; Castleman, A. W., Schäfer, F. P., Toennies, J. P., Zinth, W., Series Eds.; Springer Series in Chemical Physics; Springer Berlin Heidelberg: Berlin, Heidelberg, **2004**, 75, 215–258. https://doi.org/10.1007/978-3-662-05981-4_6.

(50) Schmal, M. Heterogeneous Catalysis and Its Industrial Applications. *Springer Science+Business Media:* New York, NY, **2016**. https://doi.org/10.1007/978-3-319-09250-8

(51) Xu, Hu & Zhang, Rui & Ng, Alan Man Ching & Djurišić, Aleksandra & Chan, Hung Tat & Chan, Wai Kin & Tong, S. Splitting Water on Metal Oxide Surfaces. *The Journal of Physical Chemistry C*. **2011**, 115. 19710–19715. 10.1021/jp2032884.

(52) Pinto, Felipe & Suzuki, Victor & Silva, R & La Porta, Felipe. Oxygen Defects and Surface Chemistry of Reducible Oxides. *Frontiers in Materials*. **2019**, 6, 260. 10.3389/fmats.2019.00260.

(53) Elahifard, Mohammadreza & Sadrian, Mohammad Reza & Mirzanejad, Amir & Behjatmanesh-Ardakani, Reza & Ahmadvand, Seyedsaeid. Dispersion of Defects in TiO_2 Semiconductor: Oxygen Vacancies in the Bulk and Surface of Rutile and Anatase. *Catalysts*. **2020**, 10, 397. 10.3390/catal10040397.

(54) Chizallet, C.; Digne, M.; Arrouvel, C.; Raybaud, P.; Delbecq, F.; Costentin, G.; Che, M.; Sautet, P.; Toulhoat, H. Insights into the Geometry, Stability and Vibrational Properties of OH Groups on c-Al_2O_3, TiO_2-Anatase and MgO from DFT Calculations. *Top Catal* **2009**, 12.

(55) Arrouvel, C.; Digne, M.; Breysse, M.; Toulhoat, H.; Raybaud, P. Effects of Morphology on Surface Hydroxyl Concentration: A DFT Comparison of Anatase–TiO_2 and γ - Alumina Catalytic Supports. *J. Catal.* **2004**, 15.

(56) Nadeem, I. M.; Harrison, G. T.; Wilson, A.; Pang, C. L.; Zegenhagen, J.; Thornton, G. Bridging Hydroxyls on Anatase TiO_2 (101) by Water Dissociation in Oxygen Vacancies. *J Phys Chem B* **2018**, 6.

(57) Groh, S.; Sabnick, H.; Ruiz, V. G.; Dzubiella, J. How the Hydroxylation State of the (110)-Rutile TiO_2 Surface Governs Its Electric Double Layer Properties. *Phys. Chem.* ***2021****, 23* (27), 14770-14782.https://doi.org/10.1039/D1CP02043A.

(58) Tsyganenko, A. A.; Filimonov, V. N., Inrared Spectra of Surface Hydroxyls Groups and Crystaline Structure of Oxides. *Journal of Molecular Structure*. **1973**, 19, 579-589.

(59) *Catalyst Preparation Methods | PDF | Catalysis | Sintering*. Scribd. https://www.scribd.com/doc/20654697/Catalyst-Preparation-Methods (accessed 2021-12-21).

(60) Liu, X.; Khinast, J. G.; Glasser, B. J. Drying of Supported Catalysts for Low Melting Point Precursors: Impact of Metal Loading and Drying Methods on the Metal Distribution. *Chem. Eng. Sci.* **2012**, *79*, 187–199. https://doi.org/10.1016/j.ces.2012.05.046.

(61) C. H. Bartholomew & R. J. Farrauto. Fundamentals of Industrial Catalytic Processes. *Wiley*, VCH. **2006**. 10.1002/9780471730071

(62) Lekhal, A.; Glasser, B. J.; Khinast, J. G. Impact of Drying on the Catalyst Profile in Supported Impregnation Catalysts. *Chem. Eng. Sci.* **2001**, 15.

(63) Perego, C.; Villa, P. Catalyst Preparation Methods. *Catal. Today* **1997**, *34* (3–4), 281–305. https://doi.org/10.1016/S0920-5861(96)00055-7.

(64) Liu, X.; Khinast, J. G.; Glasser, B. J. A Parametric Investigation of Impregnation and Drying of Supported Catalysts. *Chem. Eng. Sci.* **2008**, *63* (18), 4517–4530. https://doi.org/10.1016/j.ces.2008.06.013.

(65) Parikh, D. *Solids Drying: Basics and Applications*. Chemical Engineering. https://www.chemengonline.com/solids-drying-basics-and-applications/ (accessed 2022-01-04).

(66) Liu, X.; Khinast, J. G.; Glasser, B. J. Drying of Supported Catalysts: A Comparison of Model Predictions and Experimental Measurements of Metal Profiles. *Ind. Eng. Chem. Res.* **2010**, *49* (6), 2649–2657. https://doi.org/10.1021/ie9014606.

(67) Auvray, X.; Thuault, A. Effect of Microwave Drying, Calcination and Aging of Pt/Al_2O_3 on Platinum Dispersion. *Catalysts* **2018**, *8* (9), 348. https://doi.org/10.3390/catal8090348.

(68) Van Leeuwen, P. W. N. M. Homogeneous Metal Catalysis. In *Reference Module in Chemistry, Molecular Sciences and Chemical Engineering*; Elsevier, **2016**. https://doi.org/10.1016/B978-0-12-409547-2.11101-1.

(69) Farnetti, E.; Monte, R.; Kaspar, J. Homogeneous and Heterogeneous Catalysis. *Inorg. Chem.*

(70) Cornils, B.; Herrmann, W. A. Concepts in Homogeneous Catalysis: The Industrial View. *J. Catal.* **2003**, *216* (1–2), 23–31. https://doi.org/10.1016/S0021-9517(02)00128-8.

(71) Mukherjee, A.; Milstein, D. Homogeneous Catalysis by Cobalt and Manganese Pincer Complexes. *ACS Catal.* **2018**, *8* (12), 11435–11469. https://doi.org/10.1021/acscatal.8b02869.

(72) Luberoff, B. J. Homogeneous Catalysis: Industrial Applications and Implications Advances in Chemistry. *American Chemistry Society*; Washington, D.C. **1974**, 70. https://doi.org/10.1021/ba-1968-0070.

(73) Wu, L.; Liu, Q.; Jackstell, R.; Beller, M. Carbonylations of Alkenes with CO Surrogates. *Angew. Chem. Int. Ed.* **2014**, *53* (25), 6310–6320. https://doi.org/10.1002/anie.201400793.

(74) Fujita, S.; Okamura, S.; Akiyama, Y.; Arai, M. Hydroformylation of Cyclohexene with Carbon Dioxide and Hydrogen Using Ruthenium Carbonyl Catalyst: Influence of Pressures of Gaseous Components. *Int. J. Mol. Sci.* **2007**, *8* (8), 749–759. https://doi.org/10.3390/i8080749.

(75) Kalck, P.; Urrutigoïty, M. Tandem Hydroaminomethylation Reaction to Synthesize Amines from Alkenes. *Chem. Rev.* **2018**, *118* (7), 3833–3861. https://doi.org/10.1021/acs.chemrev.7b00667.

(76) Makuła, P.; Pacia, M.; Macyk, W. How To Correctly Determine the Band Gap Energy of Modified Semiconductor Photocatalysts Based on UV–Vis Spectra. *J. Phys. Chem. Lett.* **2018**, *9* (23), 6814–6817. https://doi.org/10.1021/acs.jpclett.8b02892.

(77) Mapukata, S.; Britton, J.; Osifeko, O. L.; Nyokong, T. The Improved Antibacterial Efficiency of a Zinc Phthalocyanine When Embedded on Silver Nanoparticle Modified Silica Nanofibers. *Photodiagnosis Photodyn. Ther.* **2021**, *33*, 102100. https://doi.org/10.1016/j.pdpdt.2020.102100.

(78) Thamaphat, Kheamrutai & Limsuwan, P. & Ngotawornchai, B. Phase characterization of TiO2 powder by XRD and TEM\n. *Nat. Sci*. **2008**, 42, 357-361.

(79) Kim, M. G.; Kang, J. M.; Lee, J. E.; Kim, K. S.; Kim, K. H.; Cho, M.; Lee, S. G. Effects of Calcination Temperature on the Phase Composition, Photocatalytic Degradation, and Virucidal Activities of TiO_2 Nanoparticles. *ACS Omega* **2021**, *6* (16), 10668–10678. https://doi.org/10.1021/acsomega.1c00043.

(80) Unwiset, P.; Chanapattharapol, K. C.; Kidkhunthod, P.; Poo-arporn, Y.; Ohtani, B. Catalytic Activities of Titania-Supported Nickel for Carbon-Dioxide Methanation. *Chem. Eng. Sci.* **2020**, *228*, 115955. https://doi.org/10.1016/j.ces.2020.115955.

(81) Hu, Z. Photocatalytic Degradation of Vehicle Exhaust Using Fe-Doped TiO_2 Loaded on Activated Carbon. *Appl. Surf. Sci.* **2017**, 10.

(82) Usui, H.; Domi, Y.; Nguyen, T. H.; Tanaka, Y.; Sakaguchi, H. Indium-Doped Rutile Titanium Oxide with Reduced Particle Length and Its Sodium Storage Properties. *ACS Omega* **2020**, 7.

(83) Ahmad, Shameem & Khan, Wasi & Raushan, Mohd. Synthesis and Characterization of Ni Doped TiO_2 Nanoparticles by Sol-Gel Method. **2015**.

(84) Berent, K.; Komarek, S.; Lach, R.; Pyda, W. The Effect of Calcination Temperature on the Structure and Performance of Nanocrystalline Mayenite Powders. *Materials,* **2019**, *12*.

(85) Kusuma, M.; Chandrappa, G.T. Effect of calcination temperature on characteristic properties of CaMoO4 nanoparticles. *Journal of Science: Advanced Materials and Devices*. **2019**. 10.1016/J.JSAMD.2019.02.003

(86) Gonnet, L.; André-Barrès, C.; Guidetti, B.; Chamayou, A.; Menendez, C.; Baron, M.; Calvet, R.; Baltas, M. Study of the Two Steps and One-Pot Two-Step Mechanochemical Synthesis of Annulated 1,2,4-Triazoles. *ACS Sustainable Chemistry & Engineering*. **2020**. 10.1021/acssuschemeng.9b05886

(87) Salami, S. A.; Smith, V. J.; Krause, R. W. M. Water-Assisted Passerini Reactions under Mechanochemical Activation: A Simple and Straightforward Access to Oxindole Derivatives. *ChemistrySelect* **2023**, *8* (4), e202204325. https://doi.org/10.1002/slct.202204325.

(88) Hosseini Lakeh, E.; Yeganeh Shariyati, A.; Safarpoor Nikoo Langarudi, M.; Tajik, H.; Shirini, F. Introduction of Two New Brønsted Acidic Ionic Liquids for the Formamide and Formamidine Derivatization of Amines. *ChemistrySelect.* **2020**, *5* (25), 7488–7491. https://doi.org/10.1002/slct.202001399.

(89) Satasia, S. P.; Kalaria, P. N.; Raval, D. K. Heteropolyanion-Based Sulfated Ionic Liquid Catalyzed Formamides Synthesis by Grindstone Chemistry. *J. Mol. Catal. Chem.* **2014**, *391*, 41–47. https://doi.org/10.1016/j.molcata.2014.04.005.

(90) Majumdar, S.; De, J.; Hossain, J.; Basak, A. Formylation of Amines Catalysed by Protic Ionic Liquids under Solvent-Free Condition. *Tetrahedron Lett.* **2013**, *54* (3), 262–266. https://doi.org/10.1016/j.tetlet.2012.11.017.

(91) Zhao, W.; Chi, X.; Li, H.; He, J.; Long, J.; Xu, Y.; Yang, S. Eco-Friendly Acetylcholine-Carboxylate Bio-Ionic Liquids for Controllable *N* -Methylation and *N* -Formylation Using Ambient CO_2 at Low Temperatures. *Green Chem.* **2019**, *21* (3), 567–577. https://doi.org/10.1039/C8GC03549K.

(92) Itoh, T.; Nagata, K.; Miyazaki, M.; Ishikawa, H.; Kurihara, A.; Ohsawa, A. A Selective Reductive Amination of Aldehydes by the Use of Hantzsch Dihydropyridines as Reductant. *Tetrahedron.* **2004**, *60* (31), 6649–6655. https://doi.org/10.1016/j.tet.2004.05.096.

(93) Akbari, J.; Hekmati, M.; Sheykhan, M.; Heydari, A. Guanidine Derived Ionic Liquids: Catalyst Free Medium for N-Formylation of Amines. *Arkivoc.* **2009**, (11), 123–129. https://doi.org/10.3998/ark.5550190.0010.b12.

(94) Li, R.; Zhao, Y.; Wang, H.; Li, D.; Wu, Y.; Zhang, H.; Tang, M.-H.; Liu, Z. Ionic Liquid-Promoted Formylation of N(Sp2)-Heteroarenes with CO_2/H_2 over Pd/C. *ACS Sustain. Chem. Eng.* **2021**, *9*, 2507–2514.

(95) Xia, S.-M.; Chen, K.-H.; Fu, H.-C.; He, L.-N. Ionic Liquids Catalysis for Carbon Dioxide Conversion With Nucleophiles. *Front. Chem.* **2018**, *6*, 462. https://doi.org/10.3389/fchem.2018.00462.

(96) Maciejewski, H. Ionic Liquids in Catalysis. *Catalysts* **2021**, *11* (3), 367. https://doi.org/10.3390/catal11030367.

(97) Fujita, S.; Okamura, S.; Akiyama, Y.; Arai, M. Hydroformylation of Cyclohexene with Carbon Dioxide and Hydrogen Using Ruthenium Carbonyl Catalyst: Influence of Pressures of Gaseous Components. *Int. J. Mol. Sci.* **2007**, *8* (8), 749–759. https://doi.org/10.3390/i8080749.

(98) Wu, L.; Liu, Q.; Fleischer, I.; Jackstell, R.; Beller, M. Ruthenium-Catalysed Alkoxycarbonylation of Alkenes with Carbon Dioxide. *Nat. Commun.* **2014**, *5* (1), 3091. https://doi.org/10.1038/ncomms4091.

(99) Koch, E.-C. Acid-Base Interactions in Energetic Materials: I. The Hard and Soft Acids and Bases (HSAB) Principle-Insights to Reactivity and Sensitivity of Energetic Materials. *Propellants Explos. Pyrotech.* **2005**, *30* (1), 5–16. https://doi.org/10.1002/prep.200400080.

(100) Haas, K. L.; Franz, K. J. Application of Metal Coordination Chemistry To Explore and Manipulate Cell Biology. *Chem. Rev.* **2009**, *109* (10), 4921–4960. https://doi.org/10.1021/cr900134a.

(101) Knifton, J. F. Syngas Reactions: Part XIII. The Ruthenium 'Melt'-Catalyzed Oxonation of Terminal Olefins. *J. Mol. Catal.* **1988**, *47* (1), 99–116. https://doi.org/10.1016/0304-5102(88)85077-6.

(102) Ambrosi, A.; Denmark, S. E. Harnessing the Power of the Water-Gas Shift Reaction for Organic Synthesis. *Angew. Chem. Int. Ed Engl.* **2016**, *55* (40), 12164–12189. https://doi.org/10.1002/anie.201601803.

(103) Patrow, J. G.; Cheng, Y.; Pyles, C. G.; Luo, B.; Tonks, I. A.; Massari, A. M. Spectroscopic Study of Sol–Gel Entrapped Triruthenium Dodecacarbonyl Catalyst Reveals Hydride Formation. *J. Phys. Chem. Lett.* **2020**, *11* (17), 7394–7399. https://doi.org/10.1021/acs.jpclett.0c02316.

(104) Ungermann, C.; Landis, V.; Moya, S. A.; Cohen, H.; Walker, H.; Pearson, R. G.; Rinker, R. G.; Ford, P. C. Homogeneous Catalysis of the Water Gas Shift Reaction by Ruthenium and Other Metal Carbonyls. Studies in Alkaline Solutions. *J. Am. Chem. Soc.* **1979**, *101* (20), 5922–5929. https://doi.org/10.1021/ja00514a011.

(105) Fujita, S.; Okamura, S.; Akiyama, Y.; Arai, M. Hydroformylation of Cyclohexene with Carbon Dioxide and Hydrogen Using Ruthenium Carbonyl Catalyst: Influence of Pressures of Gaseous Components. *Int. J. Mol. Sci.* **2007**, *8* (8), 749–759. https://doi.org/10.3390/i8080749.

(106) Dabral, S.; Schaub, T. The Use of Carbon Dioxide (CO_2) as a Building Block in Organic Synthesis from an Industrial Perspective. *Adv. Synth. Catal.* **2019**, *361* (2), 223–246. https://doi.org/10.1002/adsc.201801215.

(107) Shen, X.; Meng, Q.; Dong, M.; Xiang, J.; Li, S.; Liu, H.; Han, B. Low-Temperature Reverse Water–Gas Shift Process and Transformation of Renewable Carbon Resources to Value-Added Chemicals. *ChemSusChem.* **2019**, *12* (23), 5149–5156. https://doi.org/10.1002/cssc.201902404.

(108) Frenking, G.; Fernández, I.; Holzmann, N.; Pan, S.; Krossing, I.; Zhou, M. Metal–CO Bonding in Mononuclear Transition Metal Carbonyl Complexes. *JACS Au.* **2021**, *1* (5), 623–645. https://doi.org/10.1021/jacsau.1c00106.

(109) Miyajima, K.; Mafuné, F. Thermal Decomposition of Triruthenium Dodecacarbonyl Investigated by Variable-Temperature Mass Spectrometry in the Gas Phase. *Chem. Phys. Lett.* **2022**, *786*, 139191. https://doi.org/10.1016/j.cplett.2021.139191.

(110) *Triruthenium dodecacarbonyl*. American Chemical Society. https://www.acs.org/molecule-of-the-week/archive/t/triruthenium-dodecacarbonyl.html (accessed 2023-06-08).

(111) Mason, R.; Rae, A. I. M. The Crystal Structure of Ruthenium Carbonyl, $Ru_3(CO)_{12}$. *J. Chem. Soc. Inorg. Phys. Theor.* **1968**, 0, 778–779. https://doi.org/10.1039/J19680000778.

(112) Quicksall, C.O.; Spiro, T.G. Raman frequencies of metal cluster compounds: triosmium dodecacarbonyl and triruthenium dodecacarbonyl. *Inorganic Chemistry,* **1968**, *7*, 2365-2369. https://doi.org/10.1021/ic50069a037.

(113) Churchill, M. Rowen.; Hollander, F. J.; Hutchinson, J. P. An Accurate Redetermination of the Structure of Triruthenium Dodecacarbonyl, $Ru_3(CO)_{12}$. *Inorg. Chem.* **1977**, *16* (10), 2655–2659. https://doi.org/10.1021/ic50176a051.

(114) Chini, P. Some aspects of the chemistry of polynuclear metal carbonyl compounds. *Pure and Applied Chemistry.* **1970**, *23*, 489 - 503.

(115) Chini, P.; Martinengo, S. New Rhodium Carbonyl Cluster Compounds. *J. Chem. Soc. Chem. Commun.* **1969**, No. 19, 1092–1093. https://doi.org/10.1039/C29690001092.

(116) Fukui, K.; Yonezawa, T.; Shingu, H. A Molecular Orbital Theory of Reactivity in Aromatic Hydrocarbons. *J. Chem. Phys.* **1952**, *20* (4), 722–725. https://doi.org/10.1063/1.1700523.

(117) Hieber, W. Metal Carbonyls, Forty Years of Research. In *Advances in Organometallic Chemistry*; Stone, F. G. A., West, R., Eds.; Academic Press. **1970**, 8, 1–28. https://doi.org/10.1016/S0065-3055(08)60632-2.

(118) Johnson, B. F. G.; Johnston, R. D.; Lewis, J.; Williams, I. G.; Kilty, P. A. Relative Reactivity of Triruthenium and Triosmium Dodecacarbonyls. *Chem. Commun. Lond.* **1968**, 15, 861–862. https://doi.org/10.1039/C19680000861.

(119) Johnson, B. F. G.; Johnston, R. D.; Josty, P. L.; Lewis, J.; Williams, I. G. Some Reactions of Triruthenium Dodecacarbonyl. *Nature* **1967**, *213* (5079), 901–902. https://doi.org/10.1038/213901b0.

(120) Bianchi, M.; Menchi, G.; Matteoli, U.; Piacenti, F. Catalytic Activity of Cluster Ruthenium Complexes: Oligomerization of Ethylene. *J. Organomet. Chem.* **1993**.

(121) Patrow, J. G.; Cheng, Y.; Pyles, C. G.; Luo, B.; Tonks, I. A.; Massari, A. M. Spectroscopic Study of Sol–Gel Entrapped Triruthenium Dodecacarbonyl Catalyst Reveals Hydride Formation. *J. Phys. Chem. Lett.* **2020**, *11* (17), 7394–7399. https://doi.org/10.1021/acs.jpclett.0c02316.

(122) Fujita, S.; Okamura, S.; Akiyama, Y.; Arai, M. Hydroformylation of Cyclohexene with Carbon Dioxide and Hydrogen Using Ruthenium Carbonyl Catalyst: Influence of Pressures of Gaseous Components. *Int. J. Mol. Sci.* **2007**, *8* (8), 749–759. https://doi.org/10.3390/i8080749.

(123) Castellanos, R.; Arco, E.; Altamirano-Gutiérrez, A.; Ortega, R.; Meas, Y.; Jiménez-Sandoval, O. Electrocatalytic Properties of Novel Ruthenium-Based Compounds for the Oxygen Reduction Reaction in 0.5 M H_2SO_4 : Effects of the Synthesis Atmosphere and Temperature. *J. New Mater. Electrochem. Syst.* **2005**, *8*.

(124) Piacenti, F.; Bianchi, M.; Benedetti, E. A New Cluster Ruthenium Carbonyl. *Chem. Commun. Lond.* **1967**, 15, 775a–775a. https://doi.org/10.1039/C1967000775A.

(125) Sirigu, A.; Bianchi, M.; Benedetti, E. The Crystal Structure of $Ru_6C(CO)_{17}$. *J. Chem. Soc. Chem. Commun.* **1969**, 11, 596a–596a. https://doi.org/10.1039/C2969000596A.

(126) Venter, J. J.; Vannice, M. A. DRIFTS Investigation of the Decomposition of Ruthenium Clusters on Carbon and the Subsequent Ruthenium/Carbon Catalysts. *Inorg. Chem.* **1989**, *28* (9), 1634–1644. https://doi.org/10.1021/ic00308a008.

(127) Banditelli, P.; Cuccuru, A.; Sodi, F. Decomposition Studies of Triruthenium Dodecacarbonyl and Triosmium Dodecacarbonyl. *Thermochim. Acta* **1976**, *16* (1), 89–93. https://doi.org/10.1016/0040-6031(76)85046-0.

(128) Johnson, B. F. G.; Lewis, J.; Nicholls, J. N.; Puga, J.; Raithby, P. R.; Rosales, M. J.; McPartlin, M.; Clegg, W. The Synthesis of $[Ru_5C(CO)_{15}]$ by the Carbonylation of $[Ru_6C(CO)_{17}]$ and the Reactions of the Pentanuclear Cluster with a Variety of Small Molecules: The X-Ray Structure Analyses of $[Ru_5C(CO)_{15}]$, $[Ru_5C(CO)_{15}(MeCN)]$, $[Ru_5C(CO)_{14}(PPh_3)]$, $[Ru_5C(CO)_{13}(PPh_3)_2]$, and $[Ru_5(\mu\text{-}H)_2C(CO)_{12}\{Ph_2P(CH_2)_2PPh_2\}]$. *J. Chem. Soc. Dalton Trans.* **1983**, 2, 277–290. https://doi.org/10.1039/DT9830000277.

(129) Zhao, X.; Hrbek, J.; Rodriguez, J. A. The Decomposition and Chemistry of $Ru_3(CO)_{12}$ on TiO_2 (110) Studied with X-Ray Photoelectron Spectroscopy and Temperature Programmed Desorption. *Surf. Sci.* **2005**, *575* (1), 115–124. https://doi.org/10.1016/j.susc.2004.11.012.

(130) Fujita, S.; Okamura, S.; Akiyama, Y.; Arai, M. Hydroformylation of Cyclohexene with Carbon Dioxide and Hydrogen Using Ruthenium Carbonyl Catalyst: Influence of Pressures of Gaseous Components. *Int. J. Mol. Sci.* **2007**, *8* (8), 749–759. https://doi.org/10.3390/i8080749.

(131) Viezbicke, B. D.; Patel, S.; Davis, B. E.; Birnie, D. P. Evaluation of the Tauc Method for Optical Absorption Edge Determination: ZnO Thin Films as a Model System: Tauc Method for Optical Absorption Edge Determination. *Phys. Status Solidi B* **2015**, *252* (8), 1700–1710. https://doi.org/10.1002/pssb.201552007.

(132) Tauc, J.; Grigorovici, R.; Vancu, A. Optical Properties And Electronic Structure of Amorphous Germanium. *Phys. Status Solidi* B **1966**, 15, 627−637.

Appendix

Tauc's method of determining the band gap energy using the following equation:

$$(\alpha h\nu)^{1/n} = A(h\nu - E_g),$$

whereby α is absorption coefficient, h is Planck's constant, ν is photon's frequency, A is proportionality constant, E_g is band gap energy and n is the nature of the electron transition, if n = 0.5 then transition is direct allowed, if n = 2 then transition is indirect allowed.[76 130] The Tauc's equation can now be related to the straight line equation therefore a graph of $(\alpha h\nu)^{1/n}$ vs (hν) can be plotted.[130] The value of α can be obtained from the Beer lambert law:

Transmitted light, I, is equal to the exponentially decaying intensity of incident light, I_o, passing through an absorbing medium with a thickness, l. This is given by:

$$I = I_o e^{-\alpha \cdot l},$$

$$(I/I_o) = e^{-\alpha \cdot l},$$

$$\log (I/I_o) = e^{-\alpha . l},$$

$$\log (I/I_o) = -\alpha l \cdot \log(e),$$

$$\log (I/I_o) = -\alpha l \cdot (0.4343),$$

$$\log (I_o/I) = \alpha l \cdot (0.4343),$$

$$\log (I_o/I) \text{ is absorbance A},$$

$$\therefore A = \alpha l(0.4343),$$

whereby A is absorbance value from the UV-vis data, l is width of powdered samples of which in our case was 1mm. The incident energy $h\nu$ can be obtained from:

$$E = \frac{hc}{\lambda} = \frac{1240}{\lambda},$$

whereby E is energy in electron volts (eV), h is Planck's constant, c is speed of light and λ is wavelength from the UV-vis data in nanometers (nm).

When all the calculations are done and the values obtained, the graph of $(\alpha h\nu)^{1/n}$ vs (hν) can now be plotted to obtain the value of the band gap energy from the graph by extrapolating the linear region of the graph with a straight line to the x-axis which represents the energy.[75 131] Whether the value of n is 0.5 or 2 depends on which one gives a better linear fit and thus

identifies a correct transition.[130] In this study the value of n that gives the best fit is found to be 0.5.

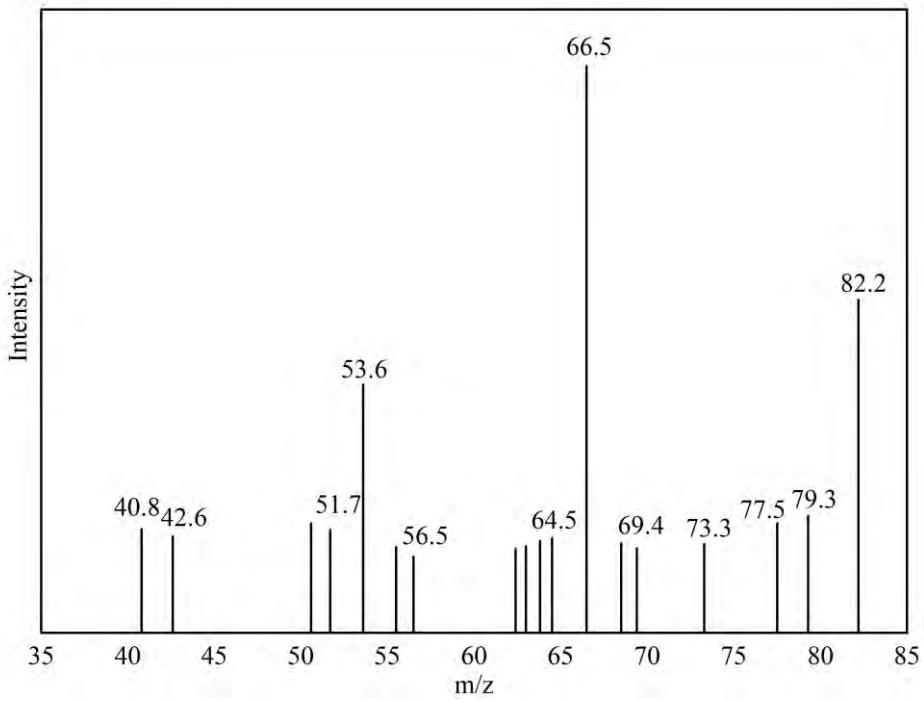

Figure A1: *Mass spectrum of the unreacted cyclohexene, 82.2 g/mol, during the reaction between cyclohexene (40 mmol), water (40 mmol) and CO_2 (11 atm) in the presence of the catalysts (25 mg) after 48 hours at 150 ^{O}C*

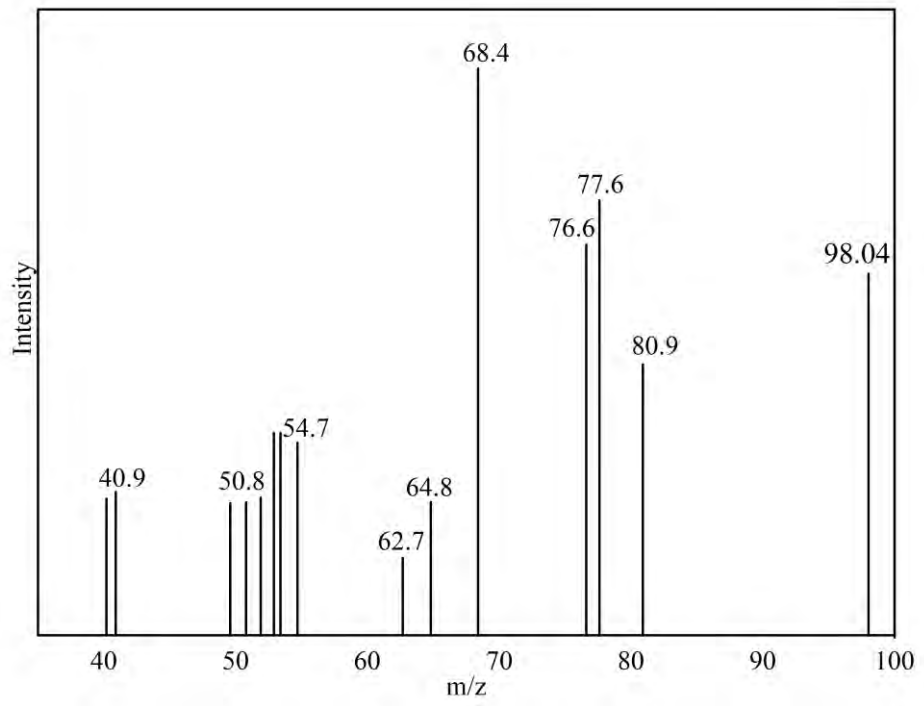

Figure A2: *Mass spectrum of cyclohexanone, 98.04 g/mol, obtained after the reaction between cyclohexene (40 mmol), water (40 mmol) and CO_2 (11 atm) in the presence of the catalysts (25 mg) after 48 hours at 150* ℃

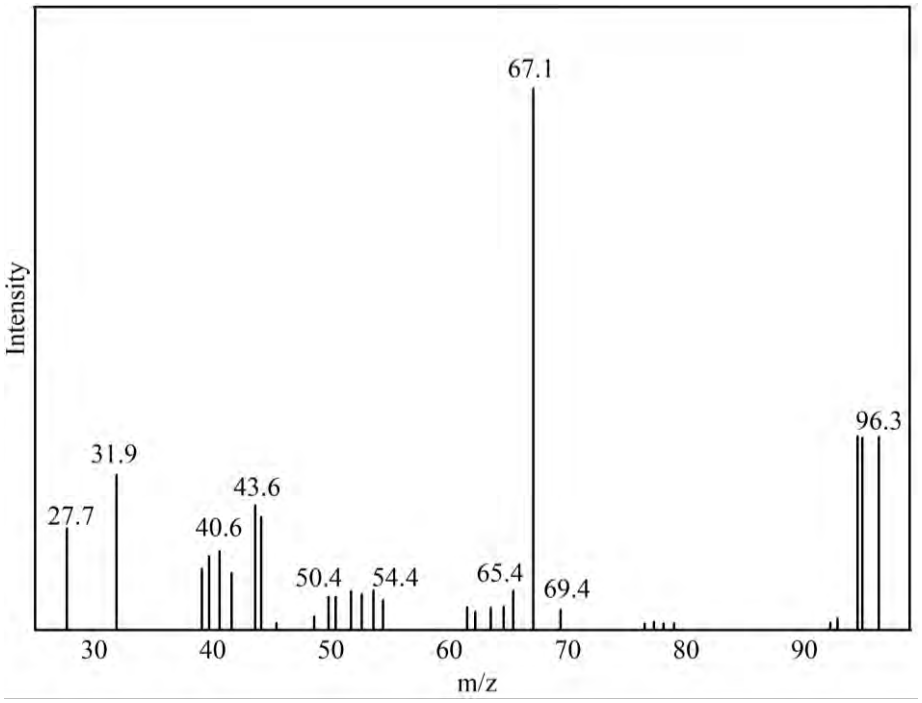

Figure A3: *Mass spectrum of cyclohexenone, 96.3 g/mol, obtained after the reaction between cyclohexene (40 mmol), water (40 mmol) and CO_2 (11 atm) in the presence of the catalysts (25 mg) after 48 hours at 150 ℃*

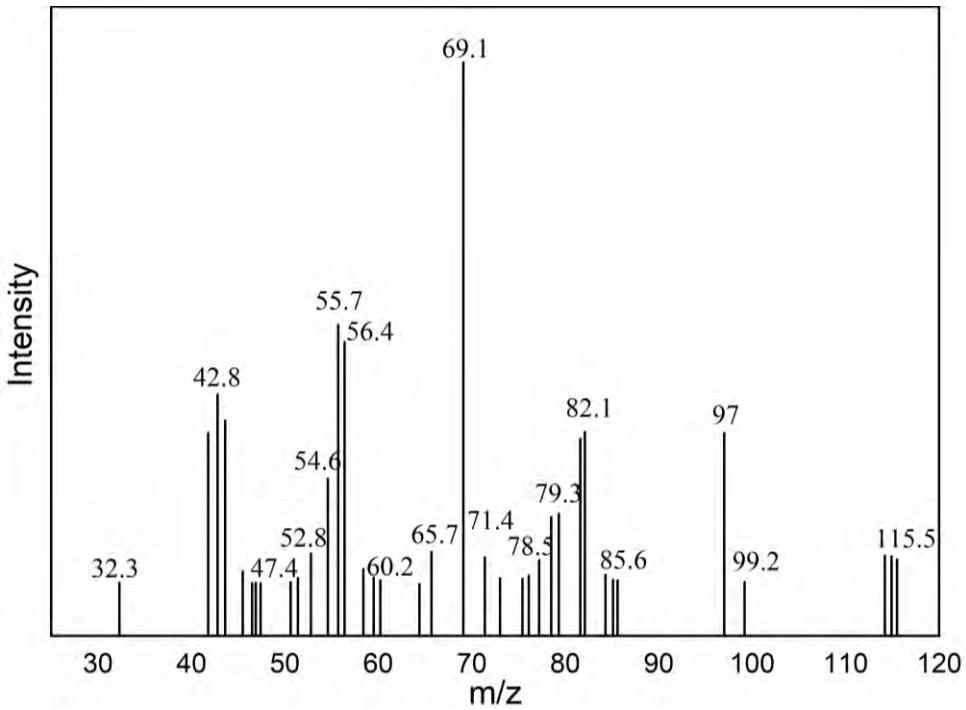

Figure A4: *Mass spectrum of cyclohexane-diol, 115.5 g/mol, obtained after the reaction between cyclohexene (40 mmol), water (40 mmol) and CO_2 (11 atm) in the presence of the catalysts (25 mg) after 48 hours at 150 ℃*

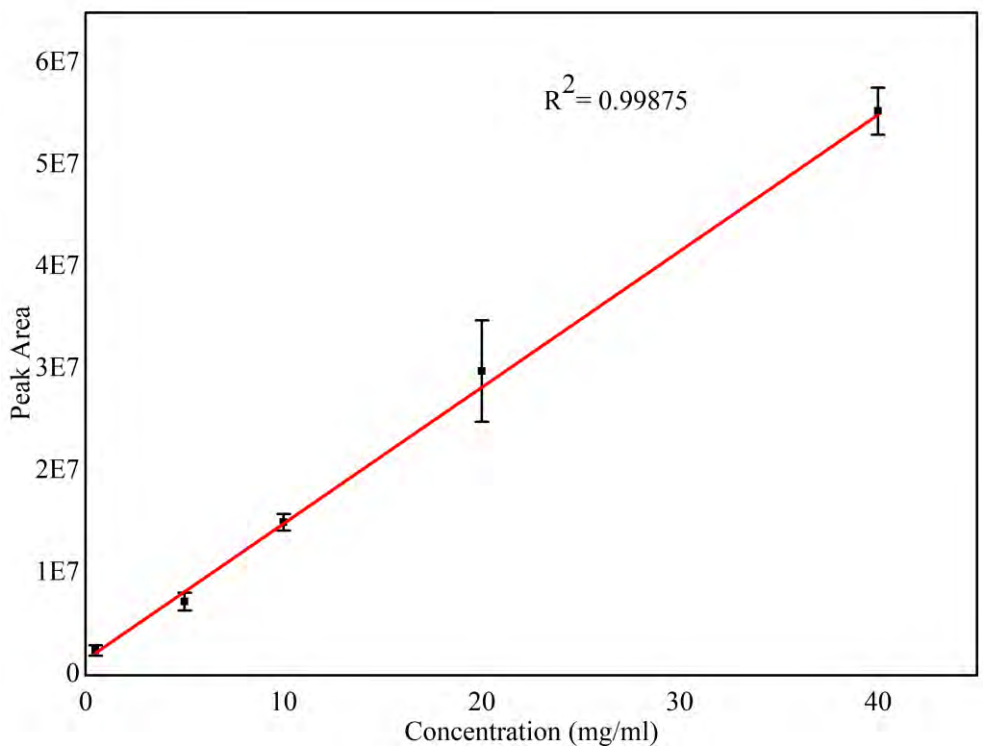

Figure A5: *Calibration curve of cyclohexene used to calculate concentration of product in reactions with gaseous CO_2*

Table A1: *Points used to draw calibration curve in (**Figure A5**)*

Concentration(mg/ml)	Area 1 x10^7	Area 2 x10^7	Area 3 x10^7	Mean area x10^7	Initial concentration
40	5,37	5,37	5,85	5,53	38,6 (mg/ml)
20	2,53	2,74	3,67	2,98	
10	1,50	1,40	1,60	1,50	
5	0,60	0,82	0,74	0,72	
0,5	0,17	0,25	0,30	0,24	

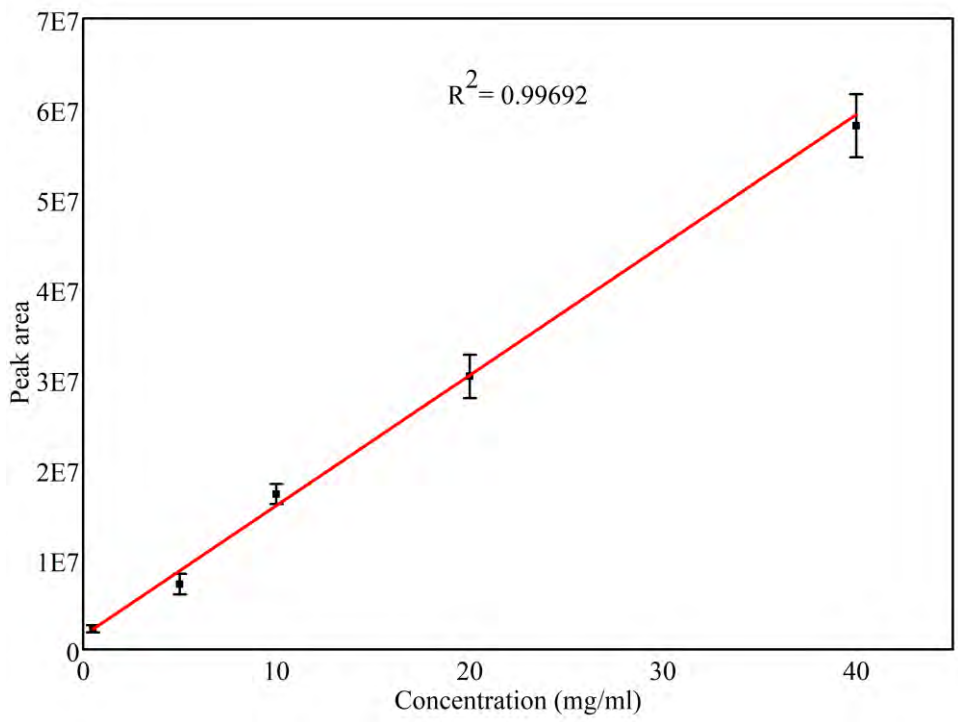

Figure A6: *Calibration curve of cyclohexene used to calculate concentration of product in reactions with solid CO_2*

Table A2: *Points used to draw calibration curve in (**Figure A6**)*

Concentration (mg/ml)	Area 1 x10^7	Area 2 x10^7	Area 3 x10^7	Mean area x10^7	Initial concentration
40	5,43	5,72	6,27	5,81	38.6 (mg/ml)
20	2,70	3,28	3,09	3,03	
10	1,75	1,84	1,57	1,72	
5	0,57	0,74	0,85	0,72	
0,5	0,17	0,25	0,26	0,22	